

Field and experimental constraints on the deformation and breakup of injected magma

by

Kirsten FitzGerald Hodge,

B.Sc., (Honors), Vanderbilt University, 2006

A THESIS SUBMITTED IN PARTIAL FULFILLMENT OF
THE REQUIREMENTS FOR THE DEGREE OF

DOCTOR OF PHILOSOPHY

in

The Faculty of Graduate Studies

(Geophysics)

THE UNIVERSITY OF BRITISH COLUMBIA

(Vancouver)

July 2012

© Kirsten FitzGerald Hodge, 2012

Abstract

Understanding the growth and differentiation of silicic magma chambers is a central issue in volcanology. Specifically, the injection, deformation and breakup of new pulses of magma can influence how the chamber evolves thermally and chemically, as well as the potential for eruption. Magmatic structures (e.g. enclaves, ladder dikes, and schlieren) preserved in plutonic and volcanic rocks record information about the physical processes that occur within the chamber prior to solidification. A key outstanding issue is how to use magmatic structures to extract information about magma rheology and host chamber dynamics within the chamber and during magma ascent—processes that are inherently inaccessible to direct observation. This thesis is an attempt to elucidate the fundamental physics that governs the breakup of an injected magma into a preexisting chamber. One major obstacle for the popular model that mafic inputs trigger big eruptions [Pallister et al., 1992; Murphy et al., 1998] and govern the long-term growth of silicic chambers is the way the new magma is injected. In particular, the scale length at which thermal and compositional heterogeneity is introduced controls how efficiently heat is transferred and the extent to which chamber convection causes mixing. This thesis provides a new understanding of how injections breakup to such small sizes, which can lead to a greater efficiency for mixing and remobilization of an otherwise immobile magma.

I use field and experimental studies to investigate specific magmatic features preserved in plutonic and volcanic rocks that can be used to constrain the magma rheology within the chamber at the time of deformation. First, I use experiments and scaling theory to investigate the mechanical and rheological conditions leading to the deformation and breakup of analog crystal-rich dikes. Second, I use field observations of “ladder dikes” from

Abstract

the Tuolumne Intrusive Suite, together with experiments and scaling theory to demonstrate that prior to solidification, these features are deformed and broken by shearing motions in the magma chamber. And third, using experimental results along with thermodynamic and modeling constraints on key physical properties of the injected and host magmas, I use size distributions of enclaves preserved in lava flows to characterize the flow regime governing enclave formation.

Preface

This thesis includes three complementary manuscripts, presented in Chapters 2, 3, and 4, that were prepared for publication in peer-reviewed scientific journals.

A version of **Chapter 2**¹ is published in *Earth and Planetary Science Letters* [Hodge et al., 2012a]. The co-authors are Kirsten Hodge (first author), Guillaume Carazzo, and Mark Jellinek. I am responsible for the setup, implementation, and analysis of all experiments presented in Chapter 2 and the majority of the writing in this manuscript. Guillaume Carazzo and Mark Jellinek helped during several of the experimental runs and provided extensive feedback for experimental setup and scaling analysis. They also contributed to numerous versions of the manuscript, providing editorial comments, feedback on the overall structure, and invaluable comments on all drafts prior to publication.

K. F. Hodge, G. Carazzo, and A. M. Jellinek. (2012), Experimental constraints on the deformation and breakup of injected magma. *Earth and Planetary Science Letters*, 325-326: 52-62.

A version of **Chapter 3**² is published in *Contributions to Mineralogy and Petrology* [Hodge et al., 2012b]. The co-authors are Kirsten Hodge (first author), Guillaume Carazzo, Xena Montague, and Mark Jellinek. I am responsible for the majority of the field work, image preparation and analysis

¹Reprinted from *Earth and Planetary Science Letters*, ©2012, with permission from Elsevier.

²Reprinted from *Contributions to Mineralogy and Petrology*, ©2012, with permission from Springer.

presented in Chapter 3 and the majority of the writing in this manuscript. Guillaume Carazzo provided help in the field, including the preparation of a detailed map of all ladder dikes presented in this Chapter. Xena Montague helped with petrologic descriptions of all outcrops studied in the Tuolumne Intrusive Suite. Mark Jellinek and Guillaume Carazzo contributed feedback on the data analysis and provided editorial comments, general comments, and scientific feedback on all drafts prior to publication.

K. F. Hodge, G. Carazzo, X. Montague, and A. M. Jellinek. (2012), Magmatic structures in the Tuolumne Intrusive Suite, California: A new model for the formation and deformation of ladder dikes. *Contributions to Mineralogy and Petrology*, 1-14.

A version of **Chapter 4** is in press to be published in *The Journal of Geophysical Research–Solid Earth*. The co-authors are Kirsten Hodge (first author) and Mark Jellinek. I am responsible for data collection, analysis, and the majority of the writing in this manuscript. Mark Jellinek provided editorial comments, general comments and scientific feedback on all drafts prior to submission.

Table of Contents

Abstract	ii
Preface	iv
Table of Contents	vi
List of Tables	x
List of Figures	xi
Acknowledgements	xiv
Dedication	xviii
1 Introduction	1
1.1 Motivation	1
1.2 Background	6
1.2.1 Magma rheology	6
1.2.2 Magmatic structures	6
1.3 Thesis structure	11
2 Experimental constraints on the deformation and breakup of injected magma	14
2.1 Introduction	14
2.2 Experiments	17
2.2.1 Experimental setup, materials and methods	17
2.2.2 Dimensionless parameters and scaling considerations	21
2.3 Qualitative observations	27

Table of Contents

2.4	Quantitative results	30
2.4.1	Regime diagram	30
2.4.2	Length scales of breakup	32
2.5	Discussion	33
2.5.1	Aspects of the dynamics of breakup and ponding	33
2.6	Implications for magmas	37
2.6.1	Enclave sizes and a regime diagram for magma chambers	37
2.6.2	Breakup vs. ponding in batholiths: Role of compositional contrasts	41
2.6.3	Some comments related to magma mixing and degassing	44
2.7	Conclusions and future work	46
3	Magmatic structures in the Tuolumne Intrusive Suite, California	48
3.1	Introduction	48
3.2	Ladder dikes in the Tuolumne Intrusive Suite	51
3.2.1	Geologic setting	51
3.2.2	What are ladder dikes?	51
3.2.3	A new quantitative model for the formation and deformation of ladder dikes: Experiments and scaling analysis	55
3.3	Ladder dike classification	59
3.3.1	Dike orientation and geometry	59
3.3.2	Classification scheme	59
3.3.3	Group 1: <i>broken</i> dikes	60
3.3.4	Group 2: <i>unbroken</i> dikes	60
3.3.5	K-feldspar-rich dikes	62
3.3.6	Mafic-felsic banding	64
3.4	Comparison with analogue experiments	64
3.4.1	Experimental results: Constraints on the deformation of ladder dikes	66

Table of Contents

3.4.2	Quantitative implications for broken ladder dikes . . .	71
3.4.3	The broken/unbroken transition: Why do some dikes break?	72
3.5	The origin of ladder structures	73
3.6	Conclusion	76
4	Linking enclave formation to magma rheology	78
4.1	Introduction	78
4.2	Enclaves in 6 Cascade lava flows	81
4.2.1	Crater Lake	81
4.2.2	Medicine Lake Volcano	81
4.2.3	Lassen Volcano	83
4.3	Methods	83
4.3.1	Field methods	85
4.3.2	Image analysis	85
4.3.3	Fractal analysis	85
4.3.4	Physical properties of host and enclave magmas from compositional data	86
4.4	A model for linking magma rheology to enclave sizes	90
4.5	Results and Discussion	93
4.5.1	A Y-S regime for enclaves in lava flows	93
4.5.2	The character of enclave fragmentation	97
4.6	Conclusions	100
5	Conclusion	101
5.1	Summary	101
5.2	Future work	102
	Bibliography	105
 Appendices		
A	Appendix	126
A.1	General concept of rheology	126

Table of Contents

A.1.1	Mathematical description	126
A.1.2	Rheology models	127
A.2	Suspension rheology	132
A.2.1	Flow around rigid particles	132
A.2.2	Particle shape and rheology	135
A.2.3	Particle behavior in a shear flow	137
A.2.4	Hydrodynamic particle diffusion in semi-dilute and concentrated suspensions	142
A.3	What controls a magma's effective viscosity	150
A.3.1	Melt viscosity	150
A.3.2	Bubbles	153
A.3.3	Crystals	153
A.4	Linking a magma's microstructure to a macroscopic descrip- tion of its rheology	155
A.4.1	Experimental set-up	158
A.4.2	Methods for calibration	160
A.4.3	Experimental conditions	160
A.4.4	Techniques for characterizing kinematics of particle- fluid motions	161
A.4.5	Measuring a macroscopic rheology: What did not work 164	
A.4.6	Future work	165

List of Tables

2.1	Experimental conditions and results	19
2.2	Symbols and parameters	22
2.3	Examples of composite plutons with and without mafic layers	43
4.1	Physical properties of six lava flows	89
4.2	Calculated properties of six lava flows	96

List of Figures

1.1	Mt. St. Helens eruption photos	1
1.2	Photos of mafic sheets and mafic enclaves preserved in silicic intrusions	4
1.3	Photos of interface between dense mafic intrusion (dark) and resident crystal-rich silicic magma (light)	7
1.4	Photos of ladder dikes in the Cathedral Peak granodiorite, near Glen Aulin, Tuolumne Meadows, Yosemite National Park.	10
2.1	Photos of mafic sheets and mafic enclaves	16
2.2	Cartoon of experimental set-up	18
2.3	Dimensionless time evolution of the three regimes	28
2.4	Evolution of breakup in the Tension regime	29
2.5	Image sequence in R-T regime experiment	30
2.6	Diagram showing injected material behavior	31
2.7	Observed vs. predicted blob size	34
2.8	Characteristic timescales for yielding and Rayleigh-Taylor instability	36
2.9	Published enclave size data	38
3.1	Photos highlighting specific features of ladder dikes that we measure in the field	49
3.2	General geologic map of Tuolumne Intrusive Suite	52
3.3	Diagram showing injected material behavior from experiments	54
3.4	Field map from Glen Aulin outcrop	58
3.5	Photomosaic showing several meters of one continuous ladder dike	61

List of Figures

3.6	Photos of large-scale meander pattern of ladder dikes	63
3.7	Rose diagram of ladder dike orientation data	64
3.8	Ladder dike classification scheme	65
3.9	Histogram showing λ values for ~ 70 meandering ladder dikes	66
3.10	Plot of the range in widths of mafic and felsic bands	67
3.11	Main results from Hodge et al. [2012a]	68
3.12	Plot of Observed d_s/d values for ladder dikes at Glen Aulin vs. Predicted d_s/d values	69
3.13	Y – S regime plot for magma chambers	70
3.14	Evolution of ladder dike deformation	75
4.1	Examples of magmatic inclusions from different lava flows . . .	79
4.2	Map of southern Cascade volcanos from this study	82
4.3	Enclave size distribution plots from our field locations	84
4.4	Main results from Hodge et al. [2012a]	91
4.5	Y-S regime diagram for enclaves in lava flows	92
4.6	Plots used to determine the fractal dimension	94
4.7	Plot of median enclave size and fractal dimension vs. the S parameter for each lava flow	99
A.1	Spring and dashpot models for the deformation of materials .	128
A.2	Stress-strain rate curves for various rheology models.	129
A.3	Stress-strain curves show hysteresis of loading and unloading of viscoelastic material	131
A.4	Flow-lines in a laminar flow of particle-free fluid far from a stationary boundary	133
A.5	A particle’s instantaneous contribution to the viscosity of a dilute suspension	137
A.6	Orientation angles, ϕ and θ of a particle undergoing motion in a simple shear flow	138
A.7	The probability density function in the ϕ -direction for parti- cles with aspect ratios between 1 and 10	140

List of Figures

A.8 Orientation distribution as a function of strain during pure and simple shear	141
A.9 Distribution of C_b ($C_b = C/(1 + C)$), where C is the orbit constant from equation A.23	144
A.10 Plot and caption from Huang et al. [2005]	149
A.11 Schematic diagram of Si-O bonds	150
A.12 Silicate melt viscosity as a function of temperature and water content	152
A.13 Monodisperse and polydisperse rigid spheres.	154
A.14 Rheological regimes as a function of crystal concentration . .	155
A.15 Photo of dense rhyolite that settled into a less dense silicic mush	157
A.16 General design of concentric cylinder rheometer	158
A.17 Example regime diagrams	161
A.18 Regime diagram showing the initial conditions of the experiments	162
A.19 Histogram plots of feldspar orientation distribution	163
A.20 PIV Image analysis process	165

Acknowledgements

Being paid to think about magma chambers and play with corn syrup all day might be one of the coolest jobs in the world. I can't say that being a graduate student did not have its rough spots, because as any Ph.D. student would quickly tell you: it's probably one of the the craziest 5 year periods of your life, but given the opportunity to work on some of the biggest problems in Earth Science, all the rough spots seem to get smoothed out in the end and we all look back and say: "wow, that was fun!" (or to be more precise, "wow, that was *type 2* fun!")

With any huge body of work that spans 5 years of your life, there are inevitably a bunch of people to thank:

1. My research supervisor: Mark Jellinek. For the past six years Mark has not only been a powerful mentor and academic support, but he has also become a wonderful friend. I could probably write a whole Ph.D. thesis entitled "Being a graduate student under Mark Jellinek: Intense, but fun." Instead, I will use this space to simply thank him for his time, energy, words of support, and his friendship. Mark is one of the most motivated, stable, and generous people I have encountered in my academic career. I feel lucky to have learned from him—not only his work ethic—but also his strong commitment to life outside of work. I remember my first days as a student at UBC, when Mark would recite: "I like to work hard to play hard." This is the truth. Who has a Ph.D. supervisor who encourages you to go skiing on a Wednesday morning to clear your head? Or a supervisor who demands that you spend time outside on a sunny day? I did. And I cannot thank him enough for being the toughest, but the best, science teacher and mentor

Acknowledgements

I've ever had. (Mark: please read that last sentence twice.)

2. My lab-mates: old and new. Heather Wilson and Amelia Bain: Thank you for the constant support, the endless distractions and laughs, and the invaluable coffee shop maneuvers. I will never forget our infamous trip to the bookstore to get a bunch of nylon jackets for Abain's experiments. Kathi Unglert and Eric Deal: Thank you for the intense, but fun times in the lab. You both filled the last years of my Ph.D. with so many (Tuesday-Thursday only) laughs, too many distractions, and a bunch of fun memories. Kathi: one day we will complete our screen play and it will be brilliant. It might not be a screen play, per se, but it sure was fun to take a step back and write it!

3. Our French Post-Doc: Guillaume Carazzo. Your guidance and support through my Ph.D. were absolutely invaluable. Working with you in the lab not only taught me how to setup and run elegant experiments, but also how to think simply and cleanly like a scientist. Your eye for perfection and your enduring patience are something that I strive for.

4. My Vancouver family: Nathalie Vigouroux, Geneviève Robert, Mandy Catron, Jen Bell, and Sandy Musclow. You all probably know more about magma rheology than you'd like to. (Expect for you Geeves—I'm sure that we could talk non-Newtonian fluids all day!) Thanks for balancing my life as a nerdy graduate student. From long climbing sessions at Cliff's, to living at the "Man's house," to Michael Jackson Wii dance parties, to many many IPA's and glasses of red wine and the finest pizza east (or west) of Main St., you gals are simply the best of the best (obviously).

5. My UBC family: Catherine Johnson, Reka Winslow, J-F Guertin, Betsy Friedlander, Lucy Porritt, Wren Bruce, Megan Wolfe, Ben Kennedy, John Hernlund, and Xena Montague. You all are the ones who kept me sane and entertained between all the science stuff. I cannot thank you enough for really making Vancouver and UBC feel like home. It has been a pleasure to

Acknowledgements

talk science and life stuff with you all. Thanks for the hallway chats and all the good advice and support that came with our friendships. Xena: thanks for your help in Tuolumne. I don't think I've ever laughed as hard as I do around you—especially when you become Kristin Wiig or Marcel the Shell. These impressions will forever make me smile.

6. My family! Mom, Menna, Drew, Liam, Lily, Grandma, Grandpa, Kim, Gabi, Josi, Elvis, Dad, Hi-Jin, Grandma, David, Kim, Ruby, and Star. I love you all. Mom and Menna: you are my gems. Your support, even from miles (or kilometres, I should say) away was always constant and strong. You have no idea how much your love and enduring confidence kept me moving through even the hardest parts of graduate school.

7. My Partner: Mark Halverson. Our weird and wonderful relationship has been one of the best outcomes from my time as a graduate student at UBC. I never thought that I would find someone who not only inspires me as a person, a musician, and a scientist, but also compliments all of my quirks. A true gem! You are, in fact, one of a kind and I am grateful that you've been by my side through this part and will be there for the rest of the journey.

8. The others: Solly, Roscoe, and Summer. Thank you for consistently being overjoyed by my presence—I always took this as the highest compliment. Except for Solly, who is only ever about 58% overjoyed by anyone's presence.

The projects presented in this thesis were generously funded by a University of British Columbia University Graduate Fellowship and a Four-Year Ph.D. Fellowship, the Natural Sciences and Engineering Research Council of Canada, a Mineralogical Society of American student research grant, the Canadian Institute for Advanced Research, and the National Science Foundation. I thank these funding sources for paying for me to hike around in the Sierras and the Cascades for three summers and to play in the lab for five years with all sorts of interesting fluids!

Acknowledgements

Queue the fiddle music!

Dedication

To my mom, my sister Menna, and my Grandparents—Penny and Bob—who used to always ask me: “When will you become a Rock Doctor?”

Chapter 1

Introduction

1.1 Motivation



Figure 1.1: Ash pours out of the crater at Mount St. Helens during the May 18th, 1980, eruption (photo credit: USGS/Robert Krimmel).

The most catastrophic volcanic events include enormous caldera-forming eruptions capable of releasing volumes on the order of $1,000 \text{ km}^3$ ($> 10^3$ times greater than the 1980 eruption of Mt. St. Helens, Figure 1.1) over the course of several days to weeks. An eruption of this magnitude could blanket the entire province of British Columbia in ~ 1 meter of volcanic ash. Well-studied examples include eruptions from the Yellowstone caldera, WY [see Christiansen, 1984; Hildreth et al., 1991; Bindeman and Valley, 2000], the Long Valley caldera, CA [see Halliday et al., 1989; Baliey, 2004; Hildreth, 2004], and from the Taupo volcanic zone, New Zealand [see Wilson et al., 1995; Jurado-Chichay and Walker, 2001]. These cataclysmic events remain one of the most poorly understood types of eruptions. The processes that control the strength and magnitude of volcanic eruptions occur in magma chambers which are zones located $10 - 15$ km below the Earth's surface that host the long-lived ($10^5 - 10^6$ years [Jellinek and DePaolo, 2003]) accumulation of large volumes (order $1,000 \text{ km}^3$) of eruptible magma. From a societal standpoint, it is important to understand the processes active inside these subsurface magma chambers in order to fully realize how and why an eruption of this magnitude can occur. Central to the issue of how and why these eruption occur is the eruption timescale: How does all that magma get out so quickly? Broadly speaking, the eruption rate is controlled by the mobilization of magma from inside the chamber through the volcanic conduit. A magma's rheological behavior, specifically how it moves and deforms, is ultimately what governs the timescale for mobilization. I use the term *magma* here to describe a particle suspension (see Appendices A.2 and A.4) that is a mixture of melt, crystals, and bubbles. When the crystal fraction is below ~ 50 vol.% a magma will flow. Above this threshold ($\sim 50 - 60$ vol.%) [Marsh, 1981] there exists a touching crystal framework, which results in strong frictional interactions between neighboring crystals. The fundamental mechanical problem of erupting such a rheologically-complex material puts specific demands on the underlying magma chamber processes.

1.1. Motivation

Several studies have hypothesized that volcanic eruptions can be triggered by the injection of a relatively more mafic (and therefore hotter) magma into a shallow silicic magma chamber [Pallister et al., 1992; Murphy et al., 1998]. This idea has motivated numerous studies on the mixing of compositionally distinct magmas [Snyder and Tait, 1996b; Jellinek and Kerr, 1999; Perugini et al., 2002; Kennedy et al., 2008; Ruprecht et al., 2008; Ruprecht and Bachmann, 2010]. Specifically, there exists numerous well-studied volcanos (e.g. Mount Pinatubo, Montserrat) whose eruptive products preserve evidence for mixing of mafic and silicic magmas prior to eruption. The preservation of evidence for magma mixing in both plutonic and volcanic rocks provides a tool for geologists to understand the details of how two compositionally distinct magmas interact. One key outstanding problem for the favored model that new mafic inputs of magma trigger big eruptions and control the growth and differentiation of silicic chambers is the way in which the new magma behaves upon injection. The scale length of thermal and compositional heterogeneity introduced by the disaggregation of new inputs of hot mafic magma will control how a magma chamber evolves both thermally and compositionally and possibly how and when it will erupt. For example, if a new intrusion of hot mafic magma breaks up into small blobs, heat will be transferred more efficiently to the host magma. This will lead to more efficient remobilization of a large batch of crystal-rich magma.

Field evidence for mechanical mixing comes in a variety of forms and emphasizes the potential complexity of the interactions between the input and resident magmas (Figure 1.2). Observationally, these interactions fall into two limiting regimes:

1. An intrusion of new magma breaks up upon entering a magma chamber and forms blobs of magma called *magmatic enclaves*, which are common in both plutonic [Barbarin, 2005; Paterson et al., 2004; Tobisch et al., 1997; Wiebe and Adams, 1997; Wiebe et al., 1997; Wiebe and Collins, 1998; Didier and Barbarin, 1991; Vernon, 1984] and volcanic rocks [Eichelberger, 1975; Vernon, 1984; Bacon and Metz, 1984;

1.1. Motivation

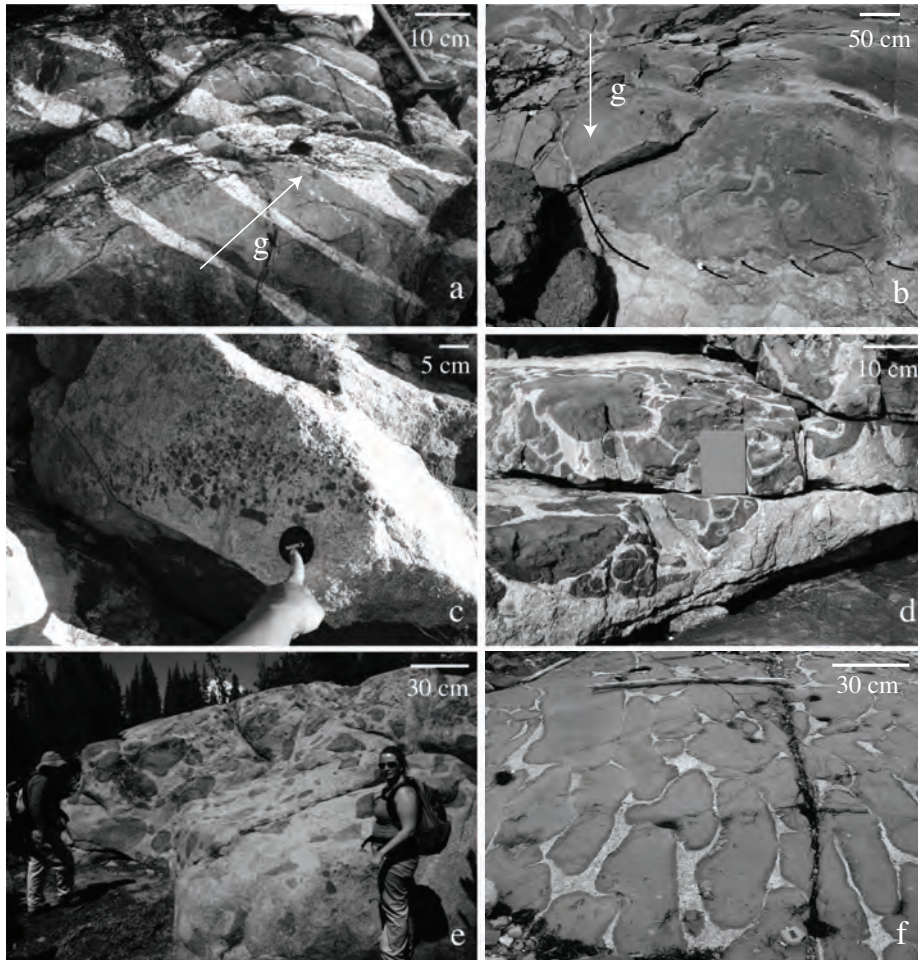


Figure 1.2: Photos of mafic sheets and mafic enclaves preserved in silicic intrusions. Photos *a* and *b* show layered mafic-silicic material from the Gouldsboro granite, Coastal Maine, and the Aztec Wash pluton, Nevada. Photos *c* and *d* show small (1 – 50 cm) mafic enclaves. Photo *c* is from the Pleasant Bay intrusion and photo *d* is from the Vinalhaven intrusive complex (Coastal Maine). Photos *e* and *f* show large (0.5 – 1 m) mafic enclaves in the Tuolumne intrusive suite (*e*) and the Vinalhaven intrusive complex (*f*). Photo *a* by R. A. Wiebe. Photo *b* by C. F. Miller. Photos *c* and *e* by K. Hodge. Photo *d* and *f* by M. Jellinek.

1.1. Motivation

Bacon, 1986; Didier and Barbarin, 1991; Wiebe et al., 1997; Clyne, 1999].

2. An injection of relatively mafic magma enters a chamber and spreads over the floor as a gravity current forming continuous layers or sheets [Wiebe, 1988; Irvine, 1982; Wiebe, 1993, 1996; Cawthorn and Walraven, 1998; Turnbull et al., 2010].

A key outstanding question crucial for understanding how silicic magma chamber grow, differentiate, and ultimately erupt is: What controls the extent to which a new injection of magma will disaggregate and form enclaves or remain intact and form continuous layers? In this regard, the broad goal of this thesis is to develop a method to utilize certain classes of magmatic structures observed in volcanic and plutonic rocks (e.g. mafic enclaves and ladder dikes) to constrain aspects of the styles of flow, stirring, and mixing within the magma chamber, as well as the rheological contrast between the two mixing magmas. In doing so, my work provides a novel technique to constrain magma chamber dynamics from basic field observations of magmatic structures, which are ultimately the remnants of dead processes. The recovery of information about the dynamics of these flows is quite remarkable and comes as a consequence of the rheology of magma—its resistance to deformation (Section 1.2.1). To achieve this goal, I use analogue experiments and theoretical scaling analyses to identify and understand the basic fluid mechanics that govern how an injected crystallizing magma interacts with a convecting chamber. In particular, I map an appropriate dynamical parameter space that governs whether and how injections break up or form layers. The key controls of this parameter space are the evolving rheology of a crystallizing injection and the flow regime of the chamber. To test the results of the analogue experiments and scaling theories, I conduct two detailed field-based studies to look at certain classes of magmatic structures: ladder dikes and enclaves. In doing so, I use the analogue experiments and scaling analysis to understand why these features exist and where in the dynamical parameter space they occur. A major result of this study is the development of a methodology that uses the geometry and size of magmatic

structures as a way to infer key aspects of the magma rheology and chamber flow regime.

1.2 Background

1.2.1 Magma rheology

Rheology describes how a material responds to an applied stress (see Appendix A.1 for a general discussion of rheology). Specifically for magmas, rheology controls flow within a chamber and influences the potential for its eruption at the surface. A magma's temperature, melt composition, and amount of suspended crystals and bubbles control its effective viscosity (Appendix A.3), which can vary over 15 orders of magnitude (from about 10 to 10^{15} Pa s, where 10 Pa s is for fluid, crystal-free melt and 10^{15} Pa s is for a rigid, crystal-rich magma [Murase and McBirney, 1973]). Consequently, this wide range in magma viscosity leads to a broad range in flow behavior, which ultimately makes magma rheology a crucial parameter not only for eruption models, but also for understanding how magma chambers accumulate and preserve strain. In particular, magmatic structures (e.g. magmatic enclaves and ladder dikes) preserved in plutonic rocks record quantitative information about the coupled crystal-melt dynamics that ultimately govern the rheological response of a magma. The crucial link between the origin of magmatic structures and chamber flow dynamics is understanding how magma rheology governs the production of magmatic textures preserved in the field.

1.2.2 Magmatic structures

Magmatic structures preserved in plutonic and volcanic rocks record information about the physical processes—e.g., mechanically driven flow during magma ascent and emplacement [Abbott, 1989; Tobisch and Cruden, 1995] or internal convection and stirring [Barrière, 1981]—that occur within the chamber prior to solidification. Numerous studies emphasize the importance of these structures (e.g. aligned minerals (Figure 1.3a & b), schlieren

1.2. Background

(Figure 1.3c), and enclaves (Figure 1.2c-f)) in documenting flow within a magma chamber [Balk, 1937; Barrière, 1981; Abbott, 1989; Tobisch and Cruden, 1995; Pitcher, 1997].



Figure 1.3: (a & b) Photos of interface between dense mafic intrusion (dark) and resident crystal-rich silicic magma (light). White lines show alignment of feldspars in the silicic magma. (c) Photo of dense rhyolite that settled into a less dense silicic mush. Parallel white lines indicate aligned biotite crystals (i.e. schlieren) and textural gradients that indicate the accumulation of simple shear strains along the side boundaries of the falling block. The white arrow indicates the direction of paleo-vertical.

This thesis focuses on two classes of magmatic structures: *mafic enclaves*, which are ubiquitous in silicic plutons and volcanic products; and *ladder dikes*, which are less common, but appear locally in a few well-studied plutons. Both enclaves and ladder dikes remain topics of ongoing study as there is no clear consensus regarding their formation.

Enclaves

There are three commonly accepted mechanisms for enclave formation: (i) injection of a relatively more mafic magma into a silicic host magma chamber, whereby the mafic injection breaks up to form enclaves as a result of stirring [Frost and Mahood, 1987; Wiebe et al., 1997; Smith, 2000; Paterson et al., 2004]; (ii) fragments of the wall rock or previously-solidified cumulate host material that break off and become entrained in the host granite [Didier and Barbarin, 1991]; and (iii) convective entrainment from ponded layers of intermediate or mafic material at the base of a silicic chamber [Vernon, 1984; Wiebe, 1993, 1996; Wiebe and Adams, 1997; Wiebe et al., 1997].

1.2. Background

Most studies cite the rheological effects of rapid cooling and solidification of a hotter mafic material upon injection into a cooler silicic chamber as a key part of the breakup process [Frost and Mahood, 1987; Snyder and Tait, 1995], though the explicit effects of heat transfer have yet to be investigated.

Neglecting the effects of heat transfer and solidification, laboratory experiments show that rounded, basaltic enclaves of various sizes may be produced in a number of ways [Campbell and Turner, 1986; Snyder and Tait, 1995; Wiebe et al., 1997; Hodge et al., 2012a]. Depending on the rate of injection, a new intrusion of basalt can enter a silicic magma chamber as a dense turbulent fountain (e.g., Campbell and Turner [1986]) or as a laminar gravity current that spreads along the chamber floor [Snyder and Tait, 1995]. Campbell and Turner [1986] show that if the Reynolds number of the injection is $> 10^2$ and the viscosity ratio is not larger than 400, the deformation and entrainment of granitic magma will lead to mechanical mixing. By inference, this process will lead to the production of enclaves where the maximum size, as well as the size and shape distribution, will depend on the structure and scale of the turbulent eddies in the fountain that can impinge, deform and entrain more viscous silicic magma. Snyder and Tait [1995] and Wiebe et al. [1997] interpret enclaves as being related to flow front instabilities forming at the nose of a basaltic intrusion spreading as a gravity current at the chamber floor. Building on this picture, Snyder and Tait [1996b] argue that subsequent thermal convection driven by heat transfer from this newly-injected layer will lead to the intermittent entrainment and stirring of basaltic “blobs” with a size that depends on the strength of the convection and the viscosity variations between the two magmas. In addition to processes occurring during magma chamber replenishment, enclaves may form as a result of magma chamber stirring during large eruptions. Thomas et al. [1993] suggest that mechanical mixing can occur following the exsolution of a gas phase from the vesiculation of mafic magma whereby low density bubble-rich basalt rises as foamy plumes, driving vigorous convection. Kennedy et al. [2008] show that the structure and mixing properties of the flow with the chamber and overlying ring dike during a caldera-forming eruption will generally be complex in both time and

space. This suggests a strong likelihood for erupted magmas that are compositionally and texturally heterogeneous over a large range of scale lengths. The length scales of texturally heterogeneity will probably depend strongly on the time-dependence of the flow and the magnitude of any viscosity variations [Koyaguchi, 1985; Blake and Campbell, 1986; Jellinek and Kerr, 1999; Jellinek et al., 1999].

Ladder dikes

Ladder dikes are a unique class of magmatic structures that exist sporadically in the Taveras pluton, Brazil [Weinberg et al., 2001] and in the Late Cretaceous intrusions that make up the Sierra Nevada batholith (Reid et al. [1993]; Paterson [2009]; Figure 1.4). In outcrop view, ladder dikes appear as long (up to 25 m), often tortuous, features that consist of alternating mafic and felsic bands. Mafic schlieren define the dike margins, and K-feldspar megacrysts that vary in size distribution and concentration appear within the mafic/felsic bands and also as large clusters within the dike margins.

The link between ladder dikes and magma chamber dynamics is poorly understood [Reid et al., 1993; Weinberg et al., 2001; Paterson, 2009]. A number of conceptual models have described how ladder dikes might form, but there is no general consensus between studies. According to Reid et al. [1993], ladder dikes occur as “crescent-shaped dark and light layers that appear dike-like in outcrop. Individual curved layers of these ‘ladder dikes’ are nested and are younger in the concave direction.” The light and dark layers contain the same petrologic phases (but in different proportions) as the surrounding host granodiorite. The dark layers and edges contain magnetite, sphene, hornblende, and biotite, and are lacking plagioclase, alkali feldspar, and quartz. The light layers contain plagioclase with lesser amounts of quartz, k-feldspar, biotite, and minor hornblende [Reid et al., 1993]. Fine-grained mafic layers grade into coarser-grained light layers. Weinberg et al. [2001] propose an interpretation based on the idea that ladder dikes are preserved plumes of silicic magma that flow relative to the surrounding material. According to their conceptual model, relative motion between fluid

1.2. Background



Figure 1.4: Photos of ladder dikes in the Cathedral Peak granodiorite, near Glen Aulin, Tuolumne Meadows, Yosemite National Park.

layers produces aligned minerals, or schlieren along the plume boundaries [Wilshire, 1969; Barrière, 1981; Abbott, 1989; Weinberg et al., 2001; Wiebe et al., 2007; Paterson, 2009]. Paterson [2009] uses the term “tube” to describe the ladder dikes. This study defines magma tubes as “cylindrical or tube-shaped structures in three dimensions that in sections perpendicular to tube axes display numerous, enclosed (if not removed by subsequent magmatic erosion), elliptical schlieren bounded by layers.” Paterson [2009] subdivides the tube structures into two types: stationary and migrating. The “stationary tubes” appear as roughly symmetric concentric schlieren rings and the “migrating tubes” appear as if a stationary tube migrated, in some cases, tens of meters. The tube structures are present throughout the Tuolumne Intrusive Suite (initial estimates by Paterson [2009] ~ 1000) and appear to be spatially clustered ($0 - 100$ tubes per km^2).

1.3 Thesis structure

This thesis combines three complementary studies aimed at understanding the deformation and breakup of injected magma into a silicic magma chamber.

In *Chapter 2*, I use laboratory experiments and scaling theory to investigate the mechanical and rheological conditions leading to the deformation and breakup of analog crystal-rich dikes injected as discrete plumes that descend into an underlying imposed shear flow. To scale the experiments and map the results across a wide range of natural conditions, I define the ratio S of the timescale for the growth of a gravitational Rayleigh-Taylor (R-T) instability of the sheared, injected material to the timescale for settling through the fluid layer and the ratio Y of the timescales for shearing and lateral disaggregation of the particle-fluid mixture (yielding). At low S (< 3) and high Y (> 40), descending plumes are stretched and tilted before undergoing R-T instability, forming drips with a wavelength that is comparable to the initial diameter of the injection. At low Y (< 40) and S values that increase from ~ 3 as $Y \rightarrow 0$, an injection yields in tension before a R-T instability can grow, forming discrete particle-fluid blobs that are much smaller than the initial injection diameter and are separated by thin filaments of the original mixture. At high S (> 3) and high Y (> 40), injections remain intact as they settle through the layer and pond at the floor. Applied to magma chambers, my results do not support the production of a continuum of enclave sizes. Indeed, from scaling analyses I expect the two breakup regimes to form distinct size populations: whereas enclaves formed in the R-T regime will be comparable to the injection size, those formed in the tension regime will be much smaller. I show that enclave size distributions observed in the field can potentially be used to infer the $Y - S$ conditions for the magma chamber at the time of injection. In addition, these observations can constrain aspects of the styles of flow, stirring, and mixing within the magma chamber, as well as the rheological contrast between the injected and host magma at the time of enclave formation. This work shows that the contrast in composition between the injected and host

magmas will have a strong effect on the mingling structures that are likely to be generated.

In *Chapter 3*, I use field observations of meter-scale “ladder dikes” from the Tuolumne Intrusive Suite (TIS), California, USA, together with analogue experiments and scaling theory (Chapter 2) to demonstrate that prior to solidification, these features are deformed and broken by shearing motions in the magma chamber. Field observations indicate that the majority of the ladder dikes are: (1) exposed perpendicular to gravity in a nearly horizontal slice through a solidified magma chamber, (2) located near a contact (specifically where they occur in large clusters) with either host rock or another intrusive unit in the TIS, and (3) oriented roughly perpendicular to that contact. The ladder dikes show evidence of breakup at the meter-scale as well as at the centimeter-scale (mafic-felsic banding). I hypothesize that the ladder dikes are buoyant plumes in a stirred magma chamber. In particular, their orientation and deformation are related to their rise (or descent) velocity, the stirring velocity within the chamber, and the rheological contrast between the plume and ambient material. The comparison between field data and laboratory experiments suggests that most of the ladder dikes deformed in a regime dominated by breakup from yielding under tension.

In *Chapter 4*, I discuss a comprehensive field study conducted to measure enclave size distributions in six Cascade lava flows. Using results from analogue experiments (Chapter 2) along with thermodynamic and modeling constraints on key physical properties of the injected and host magmas (i.e., temperature, density and effective viscosity), I use the size distributions of enclaves to characterize the flow regime governing enclave formation. Scaling arguments suggest that the viscous stresses related to magma chamber flow acting against the yield strength of a crystallizing injected magma control the breakup of 1 m-wide mafic dikes into mm-cm-scale enclaves. My data analysis identifies a corresponding characteristic breakup scale that constrains the yield strength of the injected magmas more reliably than existing empirical models for yield strength based on crystal content. In all six lava flows, I show that the progressive fragmentation of the injected magma is self-similar and characterized by a fractal dimension $D_f \sim 2$, which is

1.3. Thesis structure

similar to previous studies on enclaves. I also find a small but statistically significant dependence of D_f on the effective viscosity ratio between host and enclave magmas, such that large variations in effective viscosity enhance breakup. This work demonstrates that field observations of enclave size distributions can reliably constrain the rheological and flow conditions in which enclaves formed.

Chapter 2

Experimental constraints on the deformation and breakup of injected magma¹

2.1 Introduction

It is widely recognized that the injection of mafic or intermediate magmas into relatively silicic magma chambers through dikes can govern how these bodies grow and differentiate [Reid et al., 1983; Dodge and Kistler, 1990; Pin et al., 1990; Nardi et al., 2008; Alves et al., 2009] and also affect their tendency to feed eruptions [Pallister et al., 1992; Leonard et al., 2002]. However, a crucial issue determining the impact of such an injection on the subsequent evolution of the magma chamber is the extent to which it is stirred or mixed by ambient convection [Jellinek and Kerr, 1999]. Field evidence of such injections can take many forms and highlights the potential complexity of the interactions between the input and resident magmas (Fig. 2.1). Observationally, these interactions might be classified into two limiting regimes. In one endmember situation the intrusion breaks up on entering the magma chamber and this process is expressed in the field by the presence of magmatic enclaves [Vernon, 1984; Frost and Mahood, 1987; Didier, 1987; Pin et al., 1990; Didier and Barbarin, 1991; Blundy and Sparks, 1992; Wiebe, 1993; Elburg, 1996; Tobisch et al., 1997; Wiebe and Adams, 1997; Wiebe et al., 1997; Wiebe and Collins, 1998; Silva et al., 2000; Kim et al., 2002;

¹Reprinted from *Earth and Planetary Science Letters*, ©2012, with permission from Elsevier.

2.1. Introduction

Paterson et al., 2004; Donaire et al., 2005; Barbarin, 2005; Sahin, 2008; Barbey et al., 2008; Kumar, 2010; Smith, 2000], which are common in almost all granites [Didier and Barbarin, 1991; Vernon, 1984]. Enclave sizes are a few millimeters to several meters in diameter and their shapes, although often axisymmetric, can be complex [Kumar, 2010; Alves et al., 2009; Nardi et al., 2008; Barbey et al., 2008; Wiebe et al., 2007; Donaire et al., 2005; Barbarin, 2005; Kim et al., 2002; Silva et al., 2000; Akal and Helvaci, 1999; Wiebe and Adams, 1997; Wiebe et al., 1997; Pin et al., 1990]. Alternatively, an injection of relatively mafic magma enters a chamber, ponds and spreads over the floor as a gravity current to form continuous layers or sheets [Wiebe, 1988; Irvine, 1982; Wiebe, 1993, 1996; Cawthorn and Walraven, 1998; Turnbull et al., 2010]. Indeed, one of the enigmatic features of large silicic plutons is that whereas some are structurally layered, others are not.

Field observations of enclaves in intrusive rocks [Vernon, 1984; Didier, 1987; Didier and Barbarin, 1991; Blundy and Sparks, 1992; Wiebe, 1993; Elburg, 1996; Wiebe et al., 1997; Wiebe and Collins, 1998; Paterson et al., 2004; Barbarin, 2005; Kumar, 2010] suggest that whether injections form layers or enclaves is related to differences in density, viscosity and the yield strength of the two magmas. Three mechanisms for enclave formation have been proposed: (*i*) Deformation and stirring of a mafic magma into a more felsic host [Frost and Mahood, 1987; Wiebe et al., 1997; Smith, 2000; Paterson et al., 2004]; (*ii*) fragments of the wall-rock or previously solidified cumulate host material that break off and become entrained in the host granite [Didier and Barbarin, 1991]; and (*iii*) convective entrainment from ponded layers of intermediate or mafic material at the base of a silicic chamber [Vernon, 1984; Wiebe, 1993, 1996; Wiebe and Adams, 1997; Wiebe et al., 1997]. Although many studies identify that the rheological effects of rapid cooling and solidification of a hotter mafic material as it is injected into a cooler silicic chamber are probably a key part of the breakup process [Frost and Mahood, 1987; Snyder and Tait, 1995], these dynamics have been neglected most magma mixing studies (e.g., Koyaguchi [1985]; Campbell and Turner [1986]; Blake and Campbell [1986]; Thomas et al. [1993]; Snyder and Tait [1995, 1996b]; Thomas et al. [1993]; Jellinek and Kerr [1999]; Jellinek

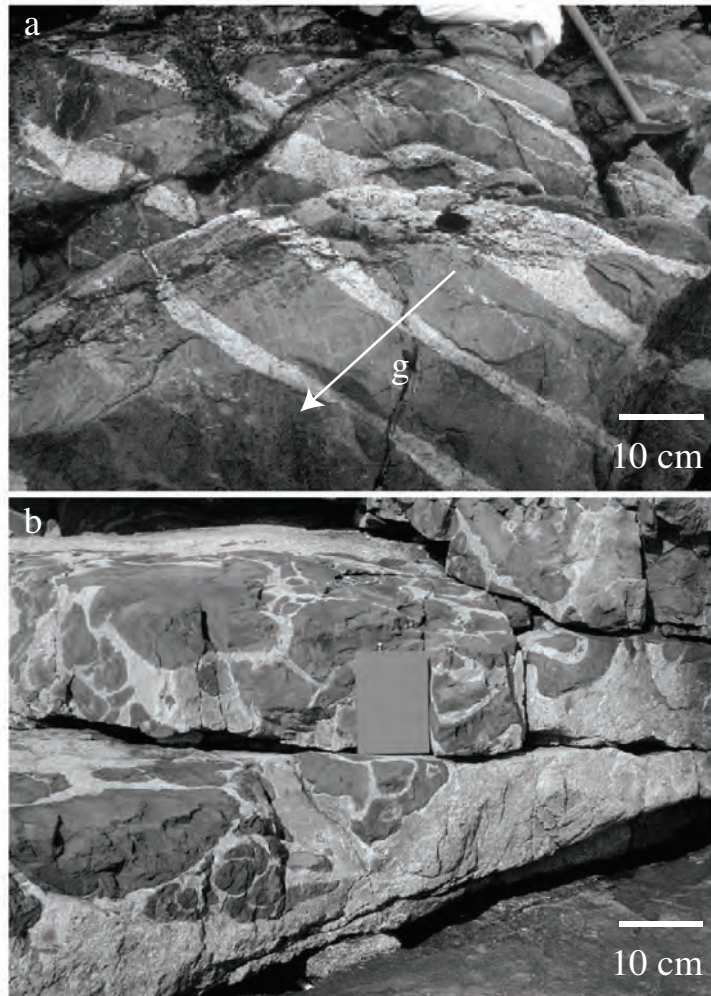


Figure 2.1: Photos of mafic sheets and mafic enclaves preserved in silicic intrusions. Photo *a* shows layered mafic-silicic material from the Gouldsboro granite, Coastal Maine. Photo *b* shows small (1–50 cm) mafic enclaves, from the Vinalhaven intrusive complex (Coastal Maine). Photo *a* by R. A. Wiebe. Photo *b* by A. M. Jellinek. Figure reprinted from *Earth and Planetary Science Letters*, ©2012, with permission from Elsevier

2.2. Experiments

et al. [1999]; Kennedy et al. [2008].

The evolution of the rheology of the injected relatively more mafic magma on cooling and solidification [Sparks and Marshall, 1986; Scaillet et al., 2000] is a key aspect of the breakup problem. In particular, whereas cooling alone will lead to an exponential increase in the mafic melt viscosity, the addition of suspended crystals can strongly augment this effect and potentially introduce non-Newtonian behavior [Lejeune and Richet, 1995; Caricchi et al., 2007]. Depending on the extent of crystallization, the injected magma may exhibit yielding behavior during replenishment. To make progress on this issue, we use analog experiments to examine the impact of enhanced viscosity and complex rheology of viscous, crystal-rich injections on the formation of layers versus enclaves in a convecting magma chamber. To capture the combined effects of cooling and solidification on the rheology of dense, mafic intrusions in a straightforward way that can be scaled to the natural magmatic case, we introduce buoyant, particle-laden plumes with different physical properties into a lower viscosity fluid undergoing simple shear flow. By carefully varying the buoyancy, effective viscosity, and yield strength of the injected material, as well as the strength of the imposed shear in the ambient fluid layer we characterize the deformation of the injections over a wide range of conditions expected to occur in natural systems. Our objectives are to understand why injected magma breaks up or ponds and to identify the main processes that set the shapes and size distributions of the broken-up material. Applying our results to magmas, we demonstrate that field observations of the shape and size distributions of enclaves can be used to constrain various chamber dynamics prior to solidification.

2.2 Experiments

2.2.1 Experimental setup, materials and methods

Our experiments are conducted in a cylindrical Plexiglas tank (8 cm high by 60 cm in diameter) filled with a 6 cm high layer of corn syrup, which has a viscosity of 251 Pa s at room temperature and a density of 1430 kg

2.2. Experiments

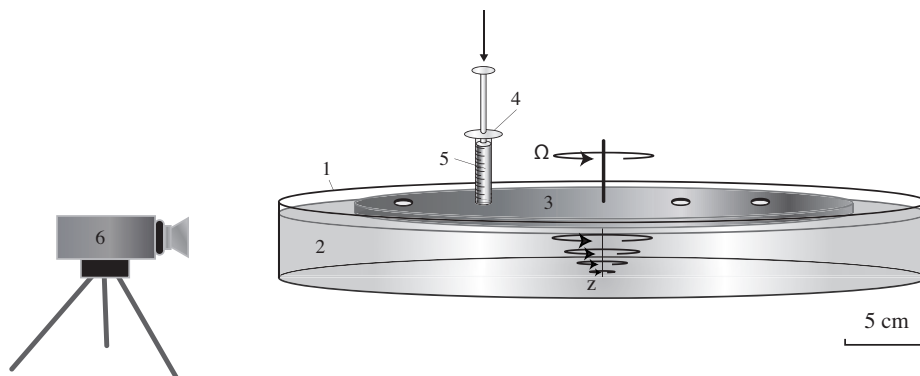


Figure 2.2: Cartoon of experimental set-up. (1) Tank, (2) corn syrup, (3) upper rotating plate, (4) syringe, (5) particle-corn syrup mixture, (6) high-speed camera.

m^{-3} (Fig. 2.2). At the top of the layer, immersed approximately 0.5 cm into the corn syrup, is a 30 cm diameter rotating cylinder with four 1 cm diameter holes at set distances measured from the center of the cylinder ($r = 5, 8, 10, 13$ cm). The rotating cylinder is attached to an external Brushless DC motor controlled by a BK Precision 1786B Programmable Power Supply and is used to generate a steady simple shear flow in the tank. There is a no-slip boundary condition along the base of the rotating cylinder and along the base and side-walls of the tank. Prior the start of each experiment, we load 3 mL of a particle-fluid mixture into plastic syringes. The cylinder is then set into motion and a steady simple shear flow with a linear vertical velocity gradient is rapidly established (the flow is at very low Reynolds number). Next, a constant volume dense plume of the particle-fluid mixture is introduced through one of the four holes by depressing a syringe. To test whether the timing or style of injection influenced the results we ran experiments at different injection rates and with the injections both before and after the start of cylinder rotation and found no dependence on these initial conditions.

The injected material is a suspension of polydisperse rigid spheres in corn syrup. The corn syrup is the same material used as the ambient fluid. The particles are zirconium silicate spheres with a density of 3600 kg m^{-3} and an

2.2. Experiments

average diameter of 0.4 mm and glass powder ($\rho = 2600 \text{ kg m}^{-3}$, $d = 1\mu\text{m}$). The volume fraction x_V of particles listed in Table 2.1 refers to the total volume fraction of both zirconium silicate spheres and glass powder. The density difference between the individual particles and the viscous syrup in the injection mixture is sufficiently small that buoyancy effects related to the relative motion of the particles and fluid within the suspension can be neglected over the short duration of the experiments. We note that because the layer depth and the diameter of the cylinder are significantly less than the diameter of the tank, additional variations in the imposed velocity field with radius related to drag on the sidewalls are minimized, an expectation that we verify prior to all experiments. The response of the dense particle-rich plume to the imposed shear flow is recorded through the side of the tank using a high-resolution video camera.

Our set-up allows us to vary several conditions externally: *(i)* particle volume concentration, *(ii)* rotation rate of the cylinder, and *(iii)* volume injected. For all experiments, the total volume injected is constant. The polydisperse particle volume fraction varies between 36% and 83% and the rotation rate varies between 0.08 and 16 rpm. A typical experiment lasts between 1 and 10 minutes (Table 2.1).

Table 2.1: Experimental conditions and results. Experiments marked with an asterisk (*) denote experiments that fell within the transition between two regimes.

experiment	$\Omega(\text{rpm})$	S	Y	x_V	regime
1	0.08	0.65	606	0.36	Rayleigh-Taylor
2	0.08	0.65	380	0.36	Rayleigh-Taylor
22	0.08	0.65	380	0.36	Rayleigh-Taylor
23	0.31	0.65	80	0.36	Rayleigh-Taylor
101	0.08	0.65	606	0.36	Rayleigh-Taylor
102	0.08	0.65	380	0.36	Rayleigh-Taylor

continued on next page

2.2. Experiments

continued from previous page

experiment	Ω (rpm)	S	Y	x_V	regime
103	0.34	0.65	57	0.36	Rayleigh-Taylor
104	0.08	1.26	920	0.47	Rayleigh-Taylor
105	0.08	1.26	575	0.47	Rayleigh-Taylor
106	0.50	1.26	58	0.47	Rayleigh-Taylor
109	0.59	2.29	66	0.57	Rayleigh-Taylor
29	0.08	2.29	1230	0.57	Rayleigh-Taylor
30	0.08	2.29	770	0.57	Rayleigh-Taylor
13	0.08	1.8	1150	0.53	Rayleigh-Taylor
14	0.08	1.8	720	0.53	Rayleigh-Taylor
107	0.08	2.29	1230	0.57	Rayleigh-Taylor
15*	0.47	1.8	78	0.53	Rayleigh-Taylor-tension
108*	0.11	2.29	555	0.57	Rayleigh-Taylor-ponding
V1001	11.86	1.8	8	0.53	tension
V1002	12.18	7.17	11	0.76	tension
V1003	8.98	0.65	3	0.36	tension
V1004*	11.22	4.18	5	0.67	tension
n6	1.62	0.65	15	0.36	tension
n7	1.62	4.18	33	0.67	tension
n3*	1.62	4.13	46	0.67	tension-ponding
28*	0.82	4.18	65	0.67	tension-ponding
R3	0.79	7.17	104	0.76	ponding
R6	0.82	4.18	5390	0.67	ponding
9	0.56	4.13	101	0.67	ponding
110	0.08	4.18	1690	0.67	ponding
4	0.08	4.18	1690	0.67	ponding
5	0.11	4.18	760	0.67	ponding
6	0.56	4.18	95	0.67	ponding
25	0.08	4.18	1690	0.67	ponding

continued on next page

2.2. Experiments

continued from previous page

experiment	Ω (rpm)	S	Y	x_V	regime
26	0.08	4.18	1060	0.67	ponding
16	0.08	7.17	2590	0.76	ponding
17	0.11	7.17	1160	0.76	ponding
18	0.79	7.17	104	0.76	ponding
7	0.08	4.13	1807	0.67	ponding
8	0.08	4.13	1130	0.67	ponding
10	0.08	10.72	5390	0.83	ponding
11	0.15	10.72	1890	0.83	ponding
12	0.82	10.72	208	0.83	ponding
<i>n1</i>	0.08	10.72	5386	0.83	ponding
<i>n2</i>	0.08	10.72	3370	0.83	ponding
<i>n4</i>	16.02	10.72	11	0.83	ponding
<i>n5</i>	6.42	10.72	26	0.83	ponding
<i>R1</i>	0.08	7.17	2590	0.76	ponding
<i>R2</i>	0.11	7.17	1160	0.76	ponding
<i>R4</i>	0.08	4.18	1690	0.67	ponding
<i>R5</i>	0.08	4.18	1060	0.67	ponding
<i>R7</i>	0.08	10.72	5390	0.83	ponding
<i>R8</i>	0.15	10.72	1890	0.83	ponding
<i>R9</i>	0.82	10.72	208	0.83	ponding

2.2.2 Dimensionless parameters and scaling considerations

To characterize the mechanics governing the behavior of negatively buoyant multiphase plumes descending into an imposed shear flow it is useful to perform dimensional analysis bearing in mind the timescales for the key dynamics at work (Table 2.2). First, the timescale for the injection to settle through the syrup layer to the tank base is:

$$t_s = \frac{\mu_a h}{\Delta \rho g^* R_i^2}, \quad (2.1)$$

2.2. Experiments

where μ_a is the viscosity of the ambient fluid, h is the fluid depth in the tank, $\Delta\rho = (\rho_i - \rho_a)$ is the density difference between the ambient fluid and the injected mixture, R_i is the injection radius, and g^* is the effective gravity which takes into account the orientation of the injection, which can be written as

$$g^* = g \sin \theta, \quad (2.2)$$

where θ is the angle of the injection from horizontal ($\theta = \arctan 1/V^*$). V^* is the ratio of the imposed cylinder velocity, $V_c = r\Omega/2\pi$, to the Stokes velocity of the injected material, V_s , and has the form

$$V^* = \frac{V_c}{V_s} = \frac{r\mu_a\Omega}{2\pi C_1 \Delta\rho g R_i^2}. \quad (2.3)$$

Here, r is the radial position of the injection point on the upper plate and Ω is the rotation rate and $C_1 \approx 0.22$ is for our cylindrical plumes.

Table 2.2: Symbols and parameters

Symbol	Value/units	Parameter
r	m	radius of upper plate at the injection point
R_i	0.0045 m	injection radius
d	0.009 m	injection diameter
h	0.06 m	fluid depth in tank
x_V		volume fraction of spheres in fluid-particle mixture
μ_i	Pa s	dynamic viscosity of the injected material ¹
μ_a	251 Pa s	dynamic viscosity of the ambient fluid at 20 °C ²
ν_i	m ² s ⁻¹	kinematic viscosity of injected mixture
ρ_i	kg m ⁻³	density of injected material
ρ_a	1430 kg m ⁻³	density of ambient fluid
$\Delta\rho$	kg m ⁻³	density difference between injected material and ambient fluid

continued on next page

2.2. Experiments

continued from previous page

Symbol	Value/unites	Parameter
λ	m	wavelength of fastest growing instability
d_b	m	measured blob size in Tension regime experiments
d_s	m	scaling for the blob size by balancing of the imposed viscous stress with the retarding yield stress of the mixture
L^*		measured wavelength and blob size normalized by radius of the injection
Ω	rad s ⁻¹	rotation rate of upper plate
V_c	m s ⁻¹	rotation velocity of upper plate
V_s	m s ⁻¹	Stokes settling velocity of injection
V^*		ratio of imposed velocity of upper plate to Stokes settling velocity
τ_y	Pa	yield stress
ϕ_m	0.85	maximum packing fraction for polydisperse spheres [Yu et al., 1993]
ϕ_c	0.25	critical packing fraction for spheres [Hoover et al., 2001]
A	5.3	constant that accounts for the total interparticle cohesion [Hoover et al., 2001]
p	1	constant that reflects the suspension's response to shearing [Hoover et al., 2001]
g^*	m s ⁻²	effective gravity which takes into account the orientation of the injection
t_{rev}	s	time for one revolution of the upper plate
t^*		$t/t_{rev} = t\Omega/2\pi$
t_s	$\mu_a h / \Delta\rho g^* R_i^2$	timescale for the injection to settle through the syrup layer
t_{rt}	$\mu_i / \Delta\rho g^* R_i$	timescale for the growth of a Rayleigh-Taylor instability:
t_f	$2\pi R_i / r\Omega$	timescale for lateral stretching over the scale of a plume diameter
t_y	$R_i \sqrt{\rho_i / \tau_y}$	timescale for lateral disaggregation or yielding of the deformed plumes

continued on next page

2.2. Experiments

continued from previous page

Symbol	Value/unites	Parameter
S	$\mu_i R_i / \mu_a h$	ratio of t_{rt} to t_s
Y	$2\pi \sqrt{\tau_y} / r\Omega \sqrt{\rho_i}$	ratio of t_f to t_y

2.2. Experiments

A second timescale is that for lateral disaggregation or yielding of the deformed plumes, which on dimensional grounds has the form:

$$t_y = R_i \sqrt{\frac{\rho_i}{\tau_y}}, \quad (2.4)$$

where τ_y is the yield strength and ρ_i is the density of the injected fluid-particle mixture. We take the yield strength of the mixture as [Wildemuth and Williams, 1984; Hoover et al., 2001],

$$\tau_y = A \left(\frac{x_V/\phi_c - 1}{1 - x_V/\phi_m} \right)^{1/p}, \quad (2.5)$$

where ϕ_c is the critical packing fraction at which the suspension can support an external stress with no deformation, ϕ_m is the volume fraction of solids in closest-packing at which the yield strength approaches infinity, A is a constant that accounts for the total interparticle cohesion, and p depends on the response of the mixture to shearing. From Hoover et al. [2001] we set $\phi_c = 0.25$, $p = 1$, and $A = 5.3$, since $x_V > \phi_c$ for all experiments. In addition, we set $\phi_m = 0.85$ to account for the polydispersivity of the spheres [Yu et al., 1993]. Replacing x_V with experimental values gives yield stresses between 4 and 450 Pa.

Because the injected plumes are negatively buoyant they can undergo a gravitational Rayleigh-Taylor-type instability if they are tilted away from vertical by the imposed shear [e.g. Skilbeck and Whitehead, 1978; Whitehead, 1988]. Consequently a third timescale is that for the growth of such an instability:

$$t_{rt} = \frac{\mu_i}{\Delta\rho g^* R_i}, \quad (2.6)$$

where μ_i is the effective viscosity of the injected material, which for high particle concentrations has the form [Scott and Kohlstedt, 2006]

$$\mu_i = \mu_a \exp(Bx_V), \quad (2.7)$$

where $B = 6$ for our working fluids.

Finally, ignoring the effects of shear at the sidewalls for reasons discussed

2.2. Experiments

above, there are three timescales for deformations by vertically-varying viscous stresses related to the imposed motion of the cylinder with a velocity V_c : (i) the timescale for a full rotation or large-scale lateral stretching $2\pi r/V_c$, (ii) the timescale for vertical shearing over the depth of the layer h/V_c , and (iii) the timescale for lateral stretching over the scale of a plume radius R_i/V_c . However, because $R_i/V_c < h/V_c \ll 2\pi r/V_c$, viscous stresses acting to stretch plumes over the full rotation time can be neglected. In addition, although viscous stresses acting over the layer depth are important for understanding the steady-state shape of a sheared plume over the full layer depth [e.g. Richards and Griffiths, 1988] lateral deformations on the scale of R_i including breakup of the injection occur almost an order of magnitude faster in our experiments. Moreover, as we are focusing on whether ponding or small-scale (compared to the layer depth) behavior such as break-up occurs we choose to simplify the problem and take a single timescale for flow to be:

$$t_f = \frac{R_i}{V_c}. \quad (2.8)$$

We use these four timescales to define two dimensionless parameters. The Stokes ratio S of the time for the growth of the first Rayleigh-Taylor instability to the time for the injection to fall through the syrup is:

$$S = \frac{t_{rt}}{t_s} = \frac{\mu_i R_i}{\mu_a h}. \quad (2.9)$$

Because R_i and h are fixed in our experiments this parameter is essentially a modified viscosity ratio, which only depends on the particle volume fraction. Next, we define a Yield ratio Y of the timescale for lateral stretching over the scale of a plume radius R_i to the timescale for yielding by lateral stretching as:

$$Y = \frac{t_f}{t_y} = \frac{2\pi}{r\Omega} \left(\frac{\tau_y}{\rho_i} \right)^{1/2}. \quad (2.10)$$

This parameter quantifies the yielding of the injected material depending on the shearing intensity. Whereas low Y conditions favor disaggregation of the mixture, the large yield strength under high Y conditions inhibits breakup from lateral stretching.

2.3 Qualitative observations

We identify three main Y – S regimes (Fig. 2.3a-c). At relatively low particle concentrations and high cylinder rotation velocities V_c ($Y \sim \mathcal{O}(10)$ and $S \sim \mathcal{O}(1)$), the strongly sheared mixture undergoes rapid extensional deformation and is pulled apart. In this “Tension regime” the injected mixture breaks up into a series of discrete particle-fluid blobs or clumps of a characteristic size that we analyze below (Fig. 2.3a). Immediately after break-up, these blobs are connected by a thin filament of interstitial fluid and entrained, widely-spaced particles. As the imposed deformation progresses the blobs roll under continued shearing to become more spherical, while entraining and stretching filament material. Concurrently, the rotation of individual particles entrained within the fluid filaments has a similar effect but at the much smaller length scale of individual particles. The combination of both effects eventually causes the larger blobs and individual particles to become disconnected from one another. Fig. 2.3a shows the time evolution of an experiment in the Tension regime. In particular, at $\sim 120t_y$ a consequence of the initial stretching is the emergence of a varicose instability with a wavelength that is small in comparison to the injection diameter. With increasing deformation ($140 - 160t_y$) small blobs form as yielding of the mixture evolves. At $180t_y$ the injection breaks and by $300t_y$ discrete blobs are apparent (highlighted in the final image in Fig. 2.3a at $t = 380t_y$). The images show that deformation begins with lateral stretching that leads, in turn, to pinch and swell or varicose behavior before ultimately yielding (see Fig. 2.4 for more detailed observations).

By contrast, at relatively low particle concentrations and more moderate V_c ($Y > \mathcal{O}(100)$ and $S \sim \mathcal{O}(1)$), comparatively modest shearing and disaggregation of the sinking multiphase plumes is followed by the growth of a gravitational Rayleigh-Taylor-type instability that takes the form of drips akin to behavior observed in studies of sheared low viscosity plumes [Skilbeck and Whitehead, 1978; Whitehead, 1988]. Fig. 2.3b shows the formation of a gravitational instability while the injection is being stretched by lateral shearing. In this “Rayleigh-Taylor (R-T)” regime, the injection

2.3. Qualitative observations

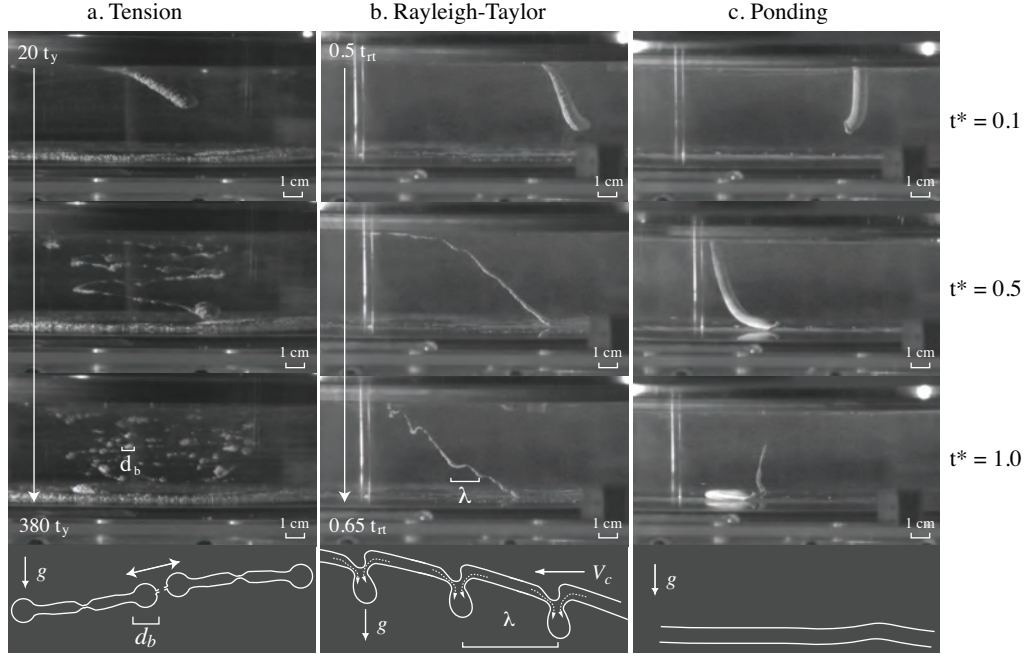


Figure 2.3: Photographs showing the dimensionless time evolution ($t^* = t\Omega/2\pi$) of the three regimes, during experiments (a) V1001 ($S = 1.8$ and $Y = 8$), (b) 13 ($S = 1.8$ and $Y = 1150$), and (c) 10 ($S = 10.72$ and $Y = 5390$) (see Table 2.1 for a list of experimental conditions). Time is reported in terms of the yield timescale t_y for the Tension regime and the Rayleigh-Taylor timescale t_{rt} for the Rayleigh-Taylor regime. The measured wavelength λ is shown for the Rayleigh-Taylor regime at $t^* = 1.0$ as well as the measured blob diameter d_b in the Tension regime (see Figs. 2.4 and 2.5 for more detail).

2.3. Qualitative observations

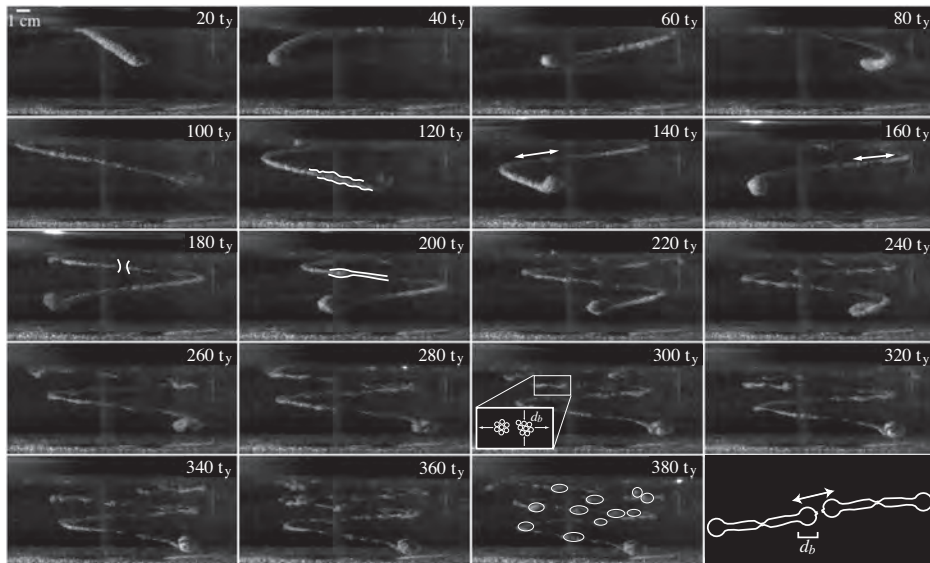


Figure 2.4: Image sequence showing evolution of injection breakup in the Tension regime experiment (V1001). Time is reported in terms of the yield timescale t_y . Image $120t_y$ shows variations in the diameter that are small in comparison to the radius R_i as lateral stretching pulls the injection apart. In images $140 - 160t_y$ small blobs form as yielding becomes the dominant deformation mechanism. The image at $t = 180t_y$ shows the first break in the injection. As the deformation progresses, small blobs of injected material form connected by thin filaments of interstitial corn syrup. The image at $t = 300t_y$ shows discrete blobs forming. Individual blobs are highlighted in the image at $t = 380t_y$.

initially sinks to the bottom of the tank ($t = 0.20t_{rt}$) and a thin tail forms behind a fat head which spreads laterally along the bottom of the tank. On a particle-scale the stretching in the tail induces movement of individual particles away from each other such that particle clumps form in regions of high cohesion which causes a local decrease in particle concentration elsewhere. As the deformation progresses, particle clumps form the troughs of drips, which grow by drawing surrounding fluid to a well-defined instability at $t = 0.40t_{rt}$ (Fig. 2.5).

Finally, for very concentrated mixtures ($S > \mathcal{O}(10)$ and for all Y) the injection remains intact as it sinks. Ultimately, the mixture breaks off at

2.4. Quantitative results

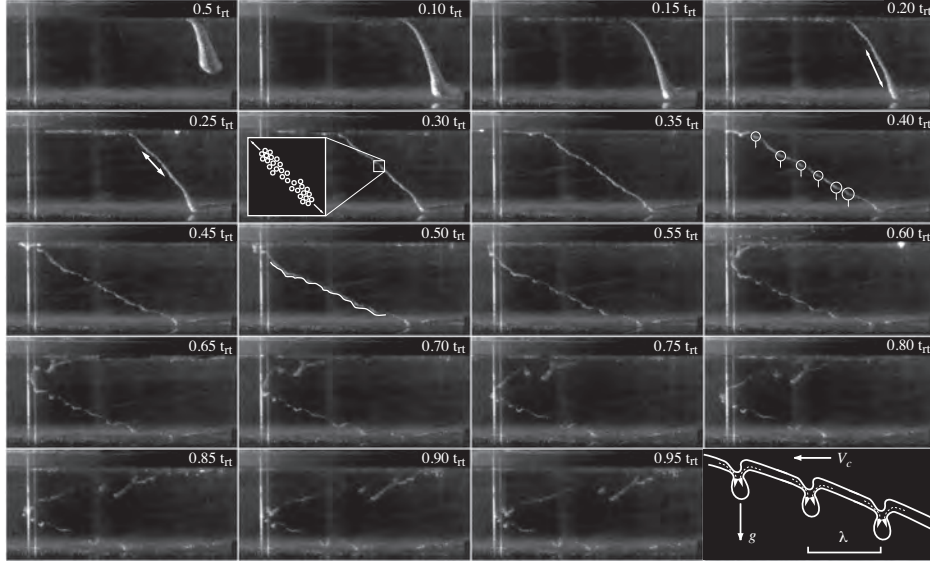


Figure 2.5: Image sequence during R-T regime for experiment 1. Time is reported in terms of the time for the injection to fall through itself, t_{rt} . The images show the formation of a gravitational instability accompanied by lateral stretching. Stretching in the thin tail of the injection is shown by the cartoon zoom in the image at $t = 0.30t_{rt}$. The instability begins at $t = 0.25t_{rt}$ and progresses as material is pulled laterally along the injection into the drips.

the injection point and ponds at the bottom of the tank (Fig. 2.3c). In this “Ponding regime” no deformation or yielding related to the imposed shear is observed.

2.4 Quantitative results

2.4.1 Regime diagram

Our experiments show that under certain conditions, a buoyant particle-rich plume descending into a shear flow can break up either as a result of the growth of a R-T instability or by tensile failure of an otherwise cohesive mixture. Which regime dominates the geometric evolution of the injection depends on the relative timescales over which these two processes act. The

2.4. Quantitative results

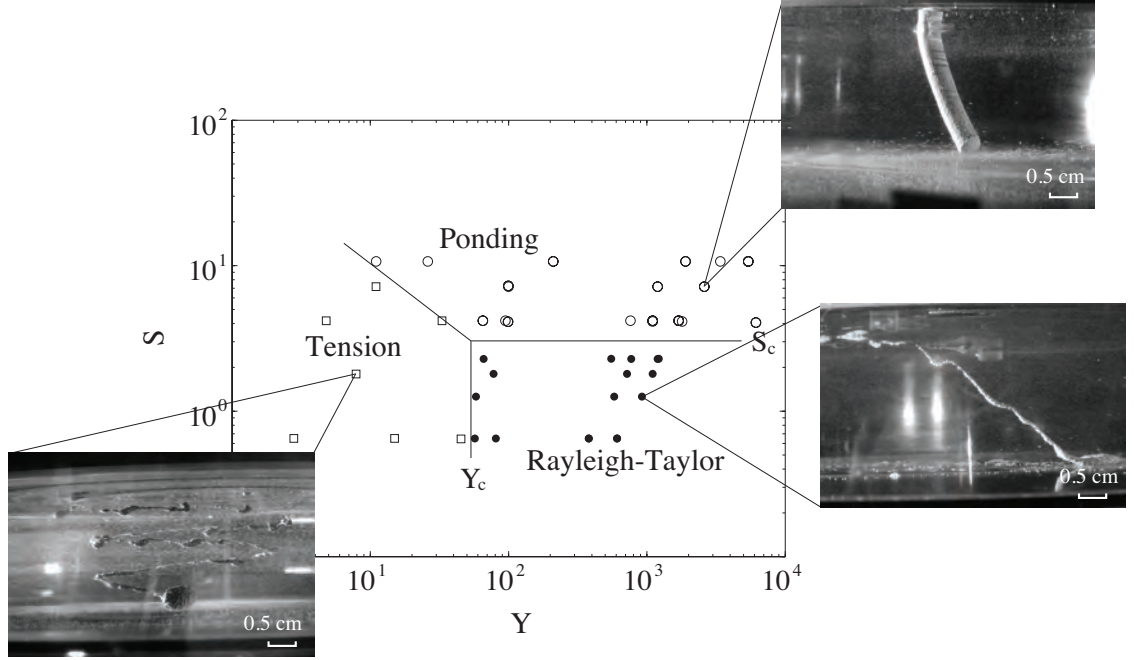


Figure 2.6: Diagram showing injected material behavior. All experiments are plotted in terms of dimensionless numbers Y and S . Transitions between the Tension, R-T, and Ponding regimes are shown by the solid lines ($Y_c \sim 50$ and $S_c \sim 3$). Photo insets show examples of injection behavior under different conditions.

full range of behavior is summarized in a $Y - S$ parameter space (Fig. 2.6). The Rayleigh-Taylor regime is observed for low S and high Y , whereas the Tension regime occurs at low S and low Y . The Ponding regime is observed when S is high except for below $Y = 40$ at which point S increases with decreasing Y .

The transition between the different regimes can be explained in terms of critical values S_c and Y_c . Where $Y < Y_c$ and $t_f < t_y < t_{rt}, t_s$, the injection breaks up in the Tension regime before settling to the base of the ambient fluid layer. Where $Y > Y_c$, $S < S_c$, and $t_{rt} < t_y < t_f, t_s$, the injection undergoes a gravitational instability in the Rayleigh-Taylor regime (Fig. 2.6). When $S > S_c$, the injection ponds over a timescale small compared to all others $t_s < t_y, t_f, t_{rt}$. Under these conditions, the injection

reaches the bottom of the tank very quickly.

2.4.2 Length scales of breakup

The length scale of breakup observed in our experiments is a fundamental result that can be used as a tool to interpret the geological record. The Tension and Rayleigh-Taylor regimes give distinct length scales for breakup. In the Tension regime, the injection breaks up into round blobs with a characteristic size d_b separated by interstitial fluid and a thin strand of particles (Fig. 2.3a). In the Rayleigh-Taylor regime, the gravitational instability is characterized by drips with a maximum wavelength λ (Fig. 2.3b). To better understand this behavior and identify theoretical scalings, we measure d_b and λ in each experiment with image analysis.

The Tension regime

For the Tension regime, we measure the average size of the large blobs once they are distinct (i.e., at $t > 320t_y$, Fig. 2.3a). We are interested in what controls the average size of these blobs. Balancing the imposed viscous stress with the retarding yield stress of the mixture gives a scale for the blob size

$$d_s = C_2 \frac{\mu_a V_c}{\tau_y}, \quad (2.11)$$

which captures the trend in the experimental data (Fig. 2.7a) with the geometric constant $C_2 = 0.001$.

The Rayleigh-Taylor regime

For the Rayleigh-Taylor regime, some care is required because all wavelengths are unstable and we are interested only in the fastest growing or dominant mode (i.e., at $t > 0.25t_{rt}$ in Fig. 2.3b). To identify this feature, in each experiment we determine visually the onset of the instability. Next, we fit a line to the deformed interface and estimate the power spectrum of the nascent gravitational instability [Welch, 1967]. From the spectra, we use a full-width-half-maximum method to estimate the wavelengths of the

dominant mode to a 95% confidence level (Fig. 2.5 and Fig. 2.3). From dimensional analysis the wavelength has the form [Chandrasekhar, 1961],

$$\lambda = C_3 \left(\frac{\nu_i^2}{g^*} \right)^{1/3} \quad (2.12)$$

where $\nu_i = \mu_i/\rho_i$ is the effective kinematic viscosity of the injection and the geometric constant $C_3 \approx 0.2$ (Fig. 2.7b). To compare our results with natural data in both regimes it is useful to introduce L^* which is the ratio of the measured blob size (Tension regime) or measured wavelength (R-T regime) to the dike width.

2.5 Discussion

2.5.1 Aspects of the dynamics of breakup and ponding

The characteristic timescales introduced in Section 2.2.2 are key tools to understanding the time evolution of our experimental plumes (see Section 2.4.1). The transition from one breakup regime to the other occurs where $t_y = t_{rt}$, and is particularly sensitive to the particle volume fraction x_V and to a lesser extent the imposed stirring velocity V_c (Fig. 2.8). The strong dependence on x_V highlights the essential role of the particle microstructure in controlling the evolution of an injection. Indeed, for a given rate of stirring the effect of the initial particle volume fraction on the evolution of the injection can clearly be profound (Fig. 2.3a and b and 2.8). In the R-T regime, shear strain accumulated by the mixture spreads out the particles and reduces both x_V and R_i linearly in time, which, in turn, decreases the local effective viscosity, buoyancy and yield strength of the mixture. From Eqs. 2.5 and 2.6, for a given injection radius R_i and stirring rate V_c , t_{rt} will consequently decline exponentially as x_V decreases with progressive stretching, whereas t_y will increase approximately in proportion to $x_V^{-1/2}$. Thus, it is not surprising that the R-T mechanism is favored for low initial particle volume fractions (Fig. 2.6 and 2.7). Moreover, once the instability begins, the additional component of stretching in the vertical direction on

2.5. Discussion

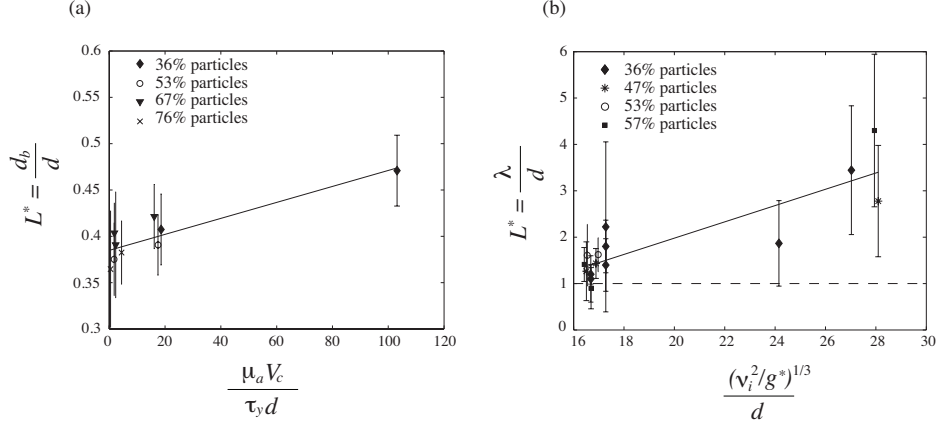


Figure 2.7: (a) Observed vs. predicted blob size d_b for experiments in the Tension regime. Each data point represents one experiment of a given particle concentration (see figure legend for symbol definitions). Observed values of d_b refer to the diameter of the blobs after one half of a cylinder revolution ($t = 380t_y$). We normalize the observed d_b and the scaling law for the blob size (d_s) by the diameter d of the injection. We define this ratio as L^* . Error bars on individual data points represent the 95% confidence level. (b) Observed vs. predicted wavelength λ for experiments in the Rayleigh-Taylor regime. Each data point represents one experiment of a given particle concentration (see figure legend for symbol definitions). The observed λ refers to the wavelength of the fastest growing instability after one half of a cylinder revolution ($t = 0.5t_{rt}$). We normalize λ and the scaling law for a R-T instability by the diameter d of the injection. We define this ratio as L^* . Error bars on individual data points represent the 95% confidence level. The dotted line represents $L^* = 1$.

its growth will spread out particles and further reduce the mixture viscosity, enhancing the growth rate of the instability (Fig. 2.3b and Fig. 2.5).

Whereas the mechanics underlying the growth of the R-T instability are readily observed and explained (Fig. 2.7b), the physical processes governing the disaggregation or yielding of the mixture are less straightforward to identify. In more detail, although yielding behavior is often observed and discussed in the context of concentrated polydisperse mixtures [Jeffrey and Acrivos, 1976; Hoover et al., 2001; Huang et al., 2005], the mechanism giving

2.5. Discussion

rise to the yield stress of the mixture as described by Eq. 2.5 remains a matter for debate. Nevertheless, in Fig. 2.5 we observe that stretching gives rise first to a pinch-and-swell or varicose instability and then to abrupt breakup where the characteristic wavelength of the resulting blobs is captured by the balance between the imposed shear stress acting to stretch the injection and the effective yield stress of the mixture expressed in the scaling in Eq. 2.11. A plausible microstructural picture is that the cohesion of the mixture is governed by the combined effect of lubrication forces between neighboring spherical particles as they are pulled apart during horizontal stretching of the injection under the imposed shear. Because particle-particle lubrication forces resisting disaggregation in tension scale as the inverse of the film thickness cubed [Leal, 1992] a further speculation is that there will be a threshold value of x_V above which the mixture will act effectively as a solid mass over the timescales of stirring and settle to the floor of the tank where it ponds as a dense layer. Indeed, this notion is an explanation for the Ponding regime at $x_V > 0.70$ (Fig. 2.8). Because $t_{rt} \rightarrow \infty$ as $x_V \rightarrow 1$, it is also reasonable to expect that the R-T mechanism will also not enter over these timescales.

Finally, whereas the transition between the Ponding and R-T regimes occurs at a constant S_c value, the transition between the Tension and Ponding regimes is a strong function of both Y and S for $Y < Y_c$ (Fig. 2.6). This behavior can be explained in two ways assuming that $t_{rt} \gg t_y$. In one view, for breakup in Tension to occur as the timescale for settling t_s becomes small (i.e., S increases) the timescale for flow t_f must decrease accordingly (i.e., Y decreases). That is, the faster the injection falls through the flow, the stronger the flow must be to cause breakup of a given mixture. Alternatively, because $Y \propto 1/t_y \propto \tau_y^{1/2}$, as t_s decreases and S becomes large the mixture must be progressively less cohesive for breakup in Tension to occur (Eqs. 2.4 and 2.10). Thus, for a transition to happen, Y must decline as S increases (Fig. 2.6).

2.5. Discussion

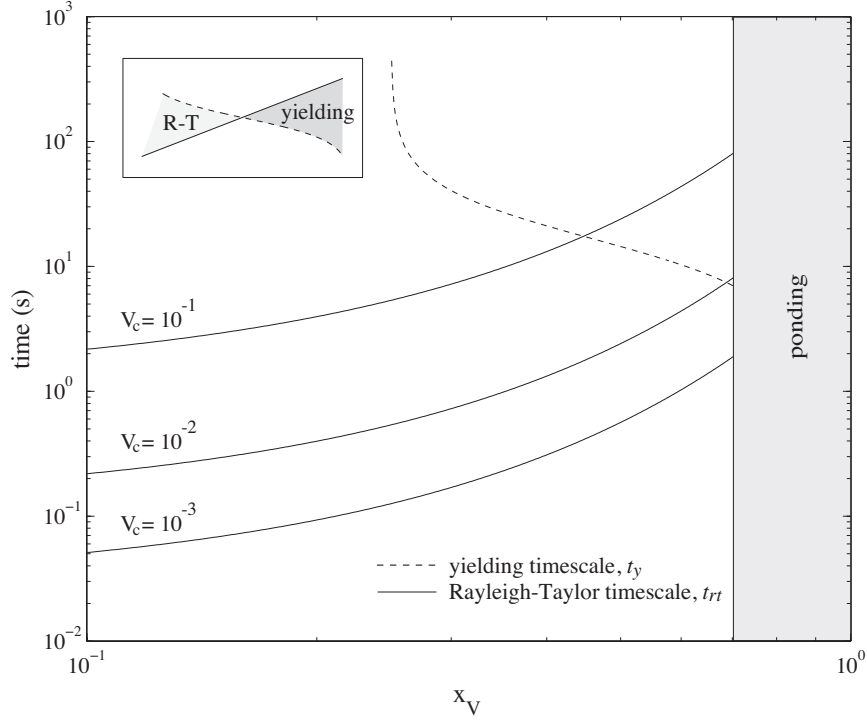


Figure 2.8: Plot showing the characteristic timescales for yielding, t_y (dashed line) and a Rayleigh-Taylor instability, t_{rt} (solid lines) vs. particle concentration, x_V . t_{rt} is shown at different values of imposed velocity, V_c . The inset shows which behavior dominates left or right of where $t_y = t_{rt}$. $R_i = 1$ m. For $x_V > 0.70$ the injection will undergo ponding behavior, which is shown in the shaded region on the right side of the plot. The asymptotic behavior as t_y goes to infinity is set by the critical packing fraction that we define in our model. After Hoover et al. [2001], we use $\phi_c = 0.25$ for spherical particles.

2.6 Implications for magmas

A key result of our work is that enclaves related to the injection of relatively more viscous magma into a convecting magma chamber are likely to be either much smaller than, or comparable in size to the width of the injection (i.e. L^* in Tension $< L^*$ in R-T Fig. 2.7). Implicit in our problem design is that these dikes are relatively more mafic than the resident magma. Consequently, the increase in melt viscosity and onset of yielding behavior on cooling and crystallization of the intrusion will cause these magmas to have a higher effective viscosity than the chamber itself. More generally, however, our results are appropriate for any situation in which the injected magma becomes more viscous than the resident magma. To apply our results to magma chambers we first present a survey of enclave sizes and use these data to develop a plausible Y – S regime diagram for magma chambers. Next, we discuss the implications of this work for magma mixing and the growth and internal differentiation of silicic magma chambers. In particular, we address the length scales of heterogeneity expected from replenishment events and discuss why some silicic magma chambers preserve a record of meter to kilometer scale mafic-silicic layering at their bases whereas others are relatively homogeneous.

2.6.1 Enclave sizes and a regime diagram for magma chambers

Fig. 2.9a shows enclave size ranges found in silicic to intermediate igneous intrusions around the world. The data suggests that there is a dominant size range from centimeters to meters in most of these systems. Millimeter-scale enclaves are present in only a few cases and are predominantly observed to be mafic micro-granular enclaves (MME); whereas, the majority of the meter-scale enclaves are felsic micro-granular enclaves (FME). Although the existing data are limited, this pattern suggests that the break-up scale is generally the same for all enclave compositions and that end-member sizes might be more influenced by composition.

To estimate Y – S conditions we assume that buoyant magma enters a

2.6. Implications for magmas

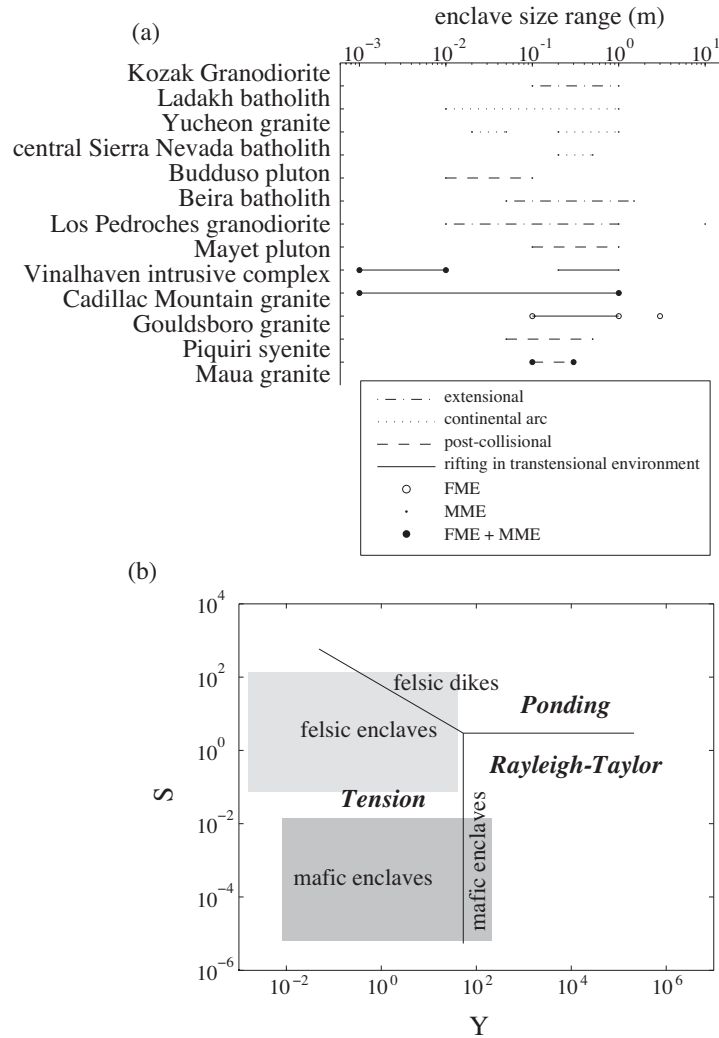


Figure 2.9: (a) Published enclave size data from silicic igneous intrusions around the world. Different line-styles denote tectonic environment (see figure legend) and different end-point symbols refer to type of enclave: FME is felsic micro-granular enclave and MME is mafic micro-granular enclave. Enclave size range is reported in meters. All plutons listed are felsic to intermediate in composition. Data sources: Kumar [2010]; Alves et al. [2009]; Nardi et al. [2008]; Barbey et al. [2008]; Wiebe et al. [2007]; Donaire et al. [2005]; Barbarin [2005]; Kim et al. [2002]; Silva et al. [2000]; Akal and Helvacı [1999]; Wiebe and Adams [1997]; Wiebe et al. [1997]; Pin et al. [1990]. (b) Y – S regime plot for magma chambers. Fields show behavior of felsic and mafic injections into a silicic chamber.

2.6. Implications for magmas

chamber through a dike. We take the dike width to be 1 m, which is reasonable for mafic and lower viscosity silicic magmas [Lister and Kerr, 1991; Petford et al., 1993], and is a value that is consistent with field observations of mafic and silicic feeder dikes for silicic plutons [Wiebe and Adams, 1997; Wiebe and Collins, 1998; Keay et al., 1997] and 10 m as a reasonable value for felsic dikes [Petford et al., 1993, 1994]. We assume that the intrusion enters a 0.1 – 1 km–high convecting silicic magma chamber in which the background flow velocity is in the range $10^{-4} - 10 \text{ m s}^{-1}$. The viscosity variations between the injected and resident magmas can be complicated for the reasons discussed above. We calculate a range in μ_i using the melt viscosity from the Giordano et al. [2008] model together with Eq. 2.7, which takes into account crystal content. For felsic injections that are similar to or more crystal rich than the ambient magma we take $\mu_i = 10^5 - 10^9 \text{ Pa s}$ and for crystallizing mafic magmas we set $\mu_i = 10^2 - 10^6 \text{ Pa s}$. Here we assume a range in crystallinity from 0.3 to 0.6. We define an ambient chamber viscosity $\mu_a = 10^5 \text{ Pa s}$ [Scott and Kohlstedt, 2006; Giordano et al., 2008; Petford, 2009]. Applying these values, we calculate $10^1 \leq S \leq 10^2$ and $10^{-2} \leq Y \leq 10^1$ for felsic intrusions and $10^{-5} \leq S \leq 10^{-2}$ and $10^{-2} \leq Y \leq 10^2$ for mafic intrusions (Fig. 2.9b). Fig. 2.9b shows that depending on the viscosity ratio, (i) a 10 m–wide felsic intrusion will either break-up in tension or pond as a continuous layer, (ii) a 1 m–wide mafic intrusion is more likely to break-up into enclaves than pond as a layer, and (iii) in both cases the mechanisms that lead to break-up in the Tension regime are probably dominant over breakup in the Rayleigh-Taylor regime.

Whereas Fig. 2.9b shows an expected range of $Y - S$ conditions for mafic and felsic injections for reasonable parameter choices, we can use the data in Fig. 2.9a together with the scalings in Eqs. 2.11 and 2.12 to constrain specific breakup regimes, as well as key aspects of the underlying magma dynamics such as the convection velocity. For example, assuming an order 1 m wide dike, the observed mafic enclave size range of order 0.01 – 1 m gives $L^* = 0.01 - 1$ (the ratio of enclave size to injection diameter), which is consistent with the Tension regime. Assuming that the data in Fig. 2.9a are predominantly formed in this regime, we apply typical chamber viscosities

2.6. Implications for magmas

of, for example, a granodiorite with 30 to 50% crystals ($10^5 - 10^9$ Pa s) and plausible yield strength values for subliquidus basalts (5 – 160 Pa) [Hoover et al., 2001] and estimate a range in chamber velocities between $10^{-4} - 10^{-2}$ m s $^{-1}$ required to breakup the injected mafic material into enclaves. For the cases favoring breakup, existing data suggest that this mechanism occurs mostly in the Tension regime (Fig. 2.9). Consequently, new magma is introduced into these chambers potentially as blobs with a scale length that is significantly less than a dike width—order tens of centimeters. Eq. 2.11 can be used to calculate chamber properties (e.g. stirring velocity, viscosity) given field data of enclave sizes or, conversely, to make predictions for L^* , based on estimates of chamber stirring velocity and viscosity.

As a final remark, the Y – S regime of a given injection can evolve in several ways. We have discussed effects related to cooling and crystallization and the range in viscosity ratios we have taken to produce Fig. 2.9b includes these effects. In principle, depending on the rate of injection, cooling and magma chamber overturn, an initially hot, low viscosity basalt may evolve to a high viscosity magma. For example, if the timescale for cooling is less than the timescale for yielding and flow, the Y – S regime is shifted to a higher S value (increase in μ_i). The opposite will occur (i.e. shift to a lower S value) if the timescale for cooling is greater than the timescale for yielding and flow.

In addition to effects related to an evolution in temperature, the amount of water in either the injected magma or the ambient magma influences the Y – S regime. Whereas water contents in calc-alkaline, or water-rich, basalts may exceed 6 wt%, they can be as low as 0.1 wt% in tholeiitic, or water-poor, basalts [Sisson and Layne, 1993]. High water contents will lead to a decrease in both viscosity and liquidus temperature of the basalt [Giordano et al., 2008]. Thus, under comparable crustal magma chamber conditions, injections of water-rich basalt will be under lower Y and lower S conditions than dry basalts. Consequently, water-rich basaltic intrusions into silicic magma chambers are relatively more likely to break up and form enclaves. Increasing the water content of the silicic host magma to oversaturated conditions, say, which is consistent with a number of recent studies [Wallace

et al., 1999; Wallace and Anderson, 1999], can reduce the viscosity of the whole chamber, leading to an increase in stirring velocity and a lower Y condition that favors breakup in the Tension regime.

2.6.2 Breakup vs. ponding in batholiths: Role of compositional contrasts

An intriguing observation is that whereas some silicic batholiths have interleaved basaltic and silicic layers near their bases, others are comparatively homogeneous. Thus, the growth and differentiation of large silicic magma chambers may occur in vastly different ways. As discussed above, based on injection viscosity, our work predicts that the wet basaltic injections characteristic of, for example, arc settings are more likely to break up than dry basaltic injections in continental settings.

In Table 2.3 we present a catalog of silicic plutons and batholiths from around the world that preserve evidence for mafic recharge into a silicic chamber either in the form of mafic layers or enclaves. The data show that, in comparison to mafic-silicic layered intrusions, chambers without mafic layers are water-rich, which means that the intruding magma can have up to 6 wt % H_2O [Sisson and Layne, 1993; Wallace, 2005; Kelley and Cottrell, 2009], which has a large effect on the magma viscosity and can alter how an injected magma deforms (breakup vs. ponding). Whereas all of the unlayered magma chambers reported in Table 2.3 are calc-alkaline and potentially water-rich, the magma composition in chambers with layering has a wide range from water-poor to water-rich. For cases where water-rich magma forms layers (e.g. Elwell et al. [1962]; Blundy and Sparks [1992]; Coleman et al. [1995]; Sisson et al. [1996]; Di Vincenzo and Rocchi [1999]), this may be a result of variations in the ambient magma viscosity and chamber stirring rates rather than properties of the injected mafic magma. Consequently, with no clear trend in the data, tectonic setting may not be the distinguishing feature for whether a chamber will form layers vs. enclaves. Likewise, basalt chemistry, which is indicative of water content, alone cannot provide a link to why mafic-silicic layering is observed in some locations and not

2.6. *Implications for magmas*

others. Instead, our experiments along with the data in Table 2.3 suggest that the rheological contrast between injected and ambient magma and the ambient chamber stirring velocity will determine the deformation regime of the intruding magma.

Table 2.3: Examples of composite plutons with and without mafic layers. Water contents are reported based on a range of typical wt % values for given basalt compositions [Dixon and Clague, 2001; Saal et al., 2002; Wallace, 2005; Kelley and Cottrell, 2009].

Plutons with mafic layers					
Intrusion	Location	Tectonic setting	Basalt type	water content (wt %)	Reference
Adamello	Italy	post-collisional	calc-alkaline	2 – 6	Blundy and Sparks [1992]
Aztec Wash	U.S.A.	extensional	calc-alkaline	2 – 6	Harper et al. [2004]
Cadillac Mountain	U.S.A.	transtensional rifting	tholeiitic	0.1 – 0.5	Wiebe [1994]
Guernsey	U.K.	continental arc	calc-alkaline	2 – 6	Wiebe et al. [1997]
Halfmoon	New Zealand	island arc	calc-alkaline	2 – 6	Elwell et al. [1960, 1962]
Mounte Plebi	Italy	extensional	calc-alkaline and tholeiitic	0.1 – 6	Turnbull et al. [2010]
Pleasant Bay	U.S.A.	transtensional rifting	tholeiitic	0.1 – 0.5	Franceschelli et al. [2005]
Onion Valley	U.S.A.	continental arc	calc-alkaline	2 – 6	Wiebe [1993]
Terra Nova	Antarctica	continental arc	calc-alkaline	2 – 6	Sisson et al. [1996]
					Di Vincenzo and Rocchi [1999]
					Perugini and Poli [2005]
Plutons without mafic layers					
Intrusion	Location	Tectonic setting	Basalt type	water content (wt %)	Reference
Budduso	Italy	continental arc	calc-alkaline	2 – 6	Barbey et al. [2008]
Kozak	Turkey	extensional	calc-alkaline	2 – 6	Akal and Helvaci [1999]
Ladakh	India	continental arc	calc-alkaline	2 – 6	Kumar [2010]
Searchlight	U.S.A.	extensional	calc-alkaline	2 – 6	Bachl et al. [2001]
Wilson Ridge	U.S.A.	extensional	calc-alkaline	2 – 6	Larsen and Smith [1990]

2.6.3 Some comments related to magma mixing and degassing

Assuming the input and resident magmas have Newtonian rheologies, for a given style of chamber convection the extent of mixing depends on the rate of stirring or shearing and the magnitude of the viscosity variations. Comparison of the large number of studies on mixing implicitly highlights that the efficiency of mixing also depends on the geometry of the problem. The structure of the motions that are responsible for mixing are, for example, different in volcanic conduits, convecting magma chambers and magma chambers undergoing a roof collapse [Blake and Campbell, 1986; Turner and Campbell, 1986; Snyder and Tait, 1996b; Jellinek and Kerr, 1999; Perugini et al., 2002; Kennedy et al., 2008; Ruprecht et al., 2008; Ruprecht and Bachmann, 2010]. Two additional issues that have not been explored systematically are the importance of the initial scale length of the injected new magma and the effect of rheological (not just viscosity) variations between the magmas. Magma replenishments in the breakup regime introduce heterogeneity at scale lengths that are small in comparison to the initial dike width. In the limit that these new magma blobs have a viscous response to magma chamber stirring motions, we would expect the rate and efficiency at which this material is stirred in to increase significantly over current estimates [Blake and Campbell, 1986; Turner and Campbell, 1986; Snyder and Tait, 1996b; Jellinek and Kerr, 1999; Perugini et al., 2002]. In the case of mafic magma, the enclaves would begin in a viscous regime followed by rapid thermal equilibrium and increased crystallization to a point at which they are too rigid to be stretched. Mechanically, the timescales for stretching in pure and simple shear down to a scale length at which chemical diffusion operates depend strongly on this initial scale length and so this expectation is not surprising. However, in our experiments breakup occurs as a result of yielding behavior. Indeed the initial size distribution of our analog enclaves includes one scale at the size of a (rotating) particle and another (rotating) “clump” scale governed by a balance between the yield stress of the mixture and imposed viscous stress. From our experiments alone it is not clear *a*

2.6. Implications for magmas

priori how to reduce clumps to individual particles.

A crucial aspect of magma chamber convection not captured in our experiments is that the motions are three-dimensional and time-dependent. Thus, the steady rotation of particle-fluid clumps we observe, for example, may be perturbed in a way that permits additional and effective stretching. However, we note, that the rheological inversion due to thermal equilibrium may hinder additional stretching of enclaves. Although we cannot comment on the occurrence or timescale for such a process, we offer a caution which is that quantifying the extent and efficiency of mixing in numerical models with classical techniques [Schmalzl et al., 1996] assuming Newtonian viscous behavior (e.g., Ruprecht and Bachmann [2010]) is likely to give misleading results.

A final remark related to mafic magmas injected in either the Ponding or Breakup regime is the effect on magma degassing. In the Breakup regime the increased surface area over which the mafic and silicic magma are coupled thermally and chemically through this mechanism should lead to enhanced thermal and chemical exchange between the two magmas. By contrast, in the Ponding regime, mafic magma has less contact with silicic magma, inhibiting thermal and chemical exchange between the magmas. Ruprecht and Bachmann [2010] show that magma mixing and reheating prior to eruption decreases magma viscosity, due to an increase in pre-eruptive temperatures. The higher temperatures, lower viscosities, and accelerated volatile diffusion lead to more efficient degassing, thus inhibiting explosive eruption behavior. Therefore, since the formation of enclaves will favor increased thermal exchange between magmas, which leads to enhanced degassing, the chambers in the breakup regime are more likely to erupt effusively. On the other hand, mafic layers that do not break up hinder thermal exchange between the injected and ambient magmas, which impedes degassing and can lead to explosive eruption behavior.

2.7 Conclusions and future work

Our experiments show that under certain conditions a buoyant particle-rich mixture injected into a shear flow can break up from either the growth of a Rayleigh-Taylor instability or by yielding under tension. The timescales over which each process acts will influence the geometric evolution of the injection. If $Y < Y_c$, the injection will deform by tensile failure of an otherwise cohesive mixture, before a Rayleigh-Taylor instability can grow. This regime produces axisymmetric blobs that are smaller in diameter than the injection size. Alternatively, if $Y > Y_c$ the injection will undergo a Rayleigh-Taylor instability, and break up at length scales similar to the size of the injection. The deformation timescales depend on the particle volume fraction x_V and the imposed stirring velocity V_c . As x_V approaches a threshold value ($x_V > 0.70$ from our experiments), we observe a Ponding regime in which the injection behaves as a solid over the timescale of stirring and sinks to the bottom of the tank.

The scalings for the two breakup regimes have implications for enclave formation in magma chambers and length scales for magma mixing. Our results suggest that enclave sizes will either be comparable to, or much smaller than the injection size. Enclave size distributions can be used to infer aspects of the style of stirring and rheology of the host magma at the time of formation. Similarly, we show that length scales (e.g. d_b or λ) for magma mixing can be estimated for a given particle volume fraction and chamber stirring velocity. In the Tension regime, we expect mixing heterogeneities that scale with or are smaller than the injection size. Whereas, in the Rayleigh-Taylor regimes, mixing length scales will range from the particle scale (thin filament connecting neighboring drips) to the size of the injection.

Although there is no direct link between tectonic setting and layering, our results identify mechanisms for the formation of layering and/or enclaves in magma chambers. From our experiments, we can infer that the absence of layering in some chambers results from a decrease in the viscosity of the input mafic magma (e.g. from the addition of water or from a higher injection temperature) and as a result, the injection is more likely to break up and

2.7. *Conclusions and future work*

form enclaves (i.e. a decrease in the S parameter) than to pond at the base of the chamber. An interesting direction for future work is to investigate the mixing properties and compositional differentiation of magma chambers in this situation. For example, is the breakup to short scale lengths in the Tension regime a major reason why unlayered chambers are so homogeneous? Since the viscosity and yield strength of the injected magma influences the deformation regime, a more important component is perhaps the composition of the mafic injection and/or volatile oversaturation (or not) in the host chamber.

Chapter 3

Magmatic structures in the Tuolumne Intrusive Suite, California: A new model for the formation and deformation of ladder dikes¹

3.1 Introduction

Magmatic structures preserved in plutonic rocks can record information about the physical processes that occur within a magma chamber prior to its solidification. Early work by Balk [1937] emphasizes the importance of internal structures (e.g. aligned minerals, schlieren, enclaves, and ladder dikes) in documenting magmatic flow during pluton emplacement. Paterson [1989] defines magmatic flow as deformation by displacement of melt in combination with rigid-body rotation of crystals. Other studies interpret magmatic structures to result from several processes: flow during magma ascent or emplacement [Abbott, 1989; Tobisch and Cruden, 1995], natural convection [Barrière, 1981; Snyder and Tait, 1996a; Wiebe and Collins, 1998; Weinberg et al., 2001; Žák and Paterson, 2005], and regional deformation [Hutton, 1988; Archanjo et al., 1994]. Wiebe and Collins [1998] suggest that magmatic structures and fabrics can also reflect processes active in a magma

¹Reprinted from *Contributions to Mineralogy and Petrology*, ©2012, with permission from Springer.

3.1. Introduction

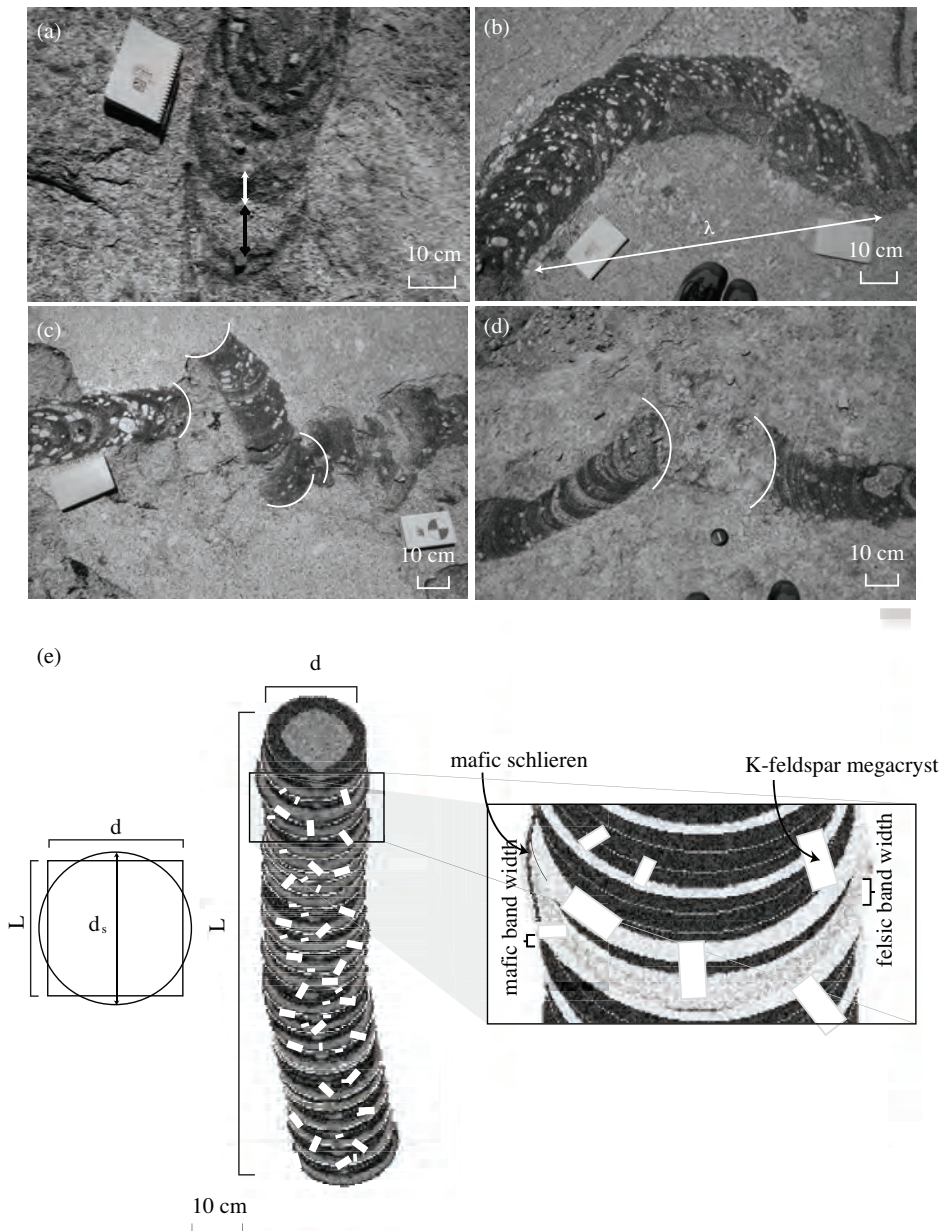


Figure 3.1: Photos highlighting specific features of ladder dikes that we measure in the field. (a) White and black lines indicate mafic and felsic band widths. (b) Large scale meander of tortuous ladder dike. We use λ to denote the wavelength of these undulations (large scale, shown here, as well as small scale undulations). (c) and (d) Break points along ladder dike length. White curved lines mark endpoints of the broken ladder dike segments. (e) Schematic cartoon showing geometry and key length scales of ladder dikes. L is the dike segment length, d is the dike width, d_s is the effective diameter of a circle of equal area to the ladder dike segment area measured in outcrop.

3.1. Introduction

chamber during solidification.

In this paper, we focus on an enigmatic class of magmatic structures called “ladder dikes” [Reid et al., 1993; Weinberg et al., 2001; Paterson, 2009]. In general, ladders dikes are long (up to 25 m), in many cases tortuous, features that consist of alternating mafic and felsic bands (Figure 3.1). Mafic schlieren define the dike margins, and K-feldspar megacrysts that vary in size distribution and concentration appear within the mafic/felsic bands and also as large clusters within the dike margins (Figure 3.1b, c, and e). Here, we present a field study on ladder dikes in the Tuolumne Intrusive Suite (TIS) conducted to test a model for the injection and breakup of dikes in a convecting magma chamber developed in Hodge et al. [2012a]. We focus on one particularly impressive outcrop located in the Cathedral Peak Granodiorite near the Tuolumne River (Figure 3.2; e.g. Reid et al. [1993]; Paterson [2009]). This location offers a unique opportunity to observe a high density of preserved magmatic flow features exposed perpendicular to gravity in a nearly horizontal slice through a solidified magma chamber [Paterson, 2009].

We hypothesize that these features are buoyant, rheologically complex plumes in a stirred magma chamber and, in particular, that their orientation and deformation are related to their rise (or descent) velocity, the stirring velocity within the chamber, and the rheological contrast between the rising plume and ambient magma. These features have been previously referred to as “ladder dikes” [Reid et al., 1993] and “migrating tubes” [Paterson, 2009]. We use a combination of detailed field measurements, laboratory experiments, and scaling theory to argue that meter-scale ladder dikes are relict plumes strongly deformed by shearing motions in the TIS magma chamber. We propose that these delicate features preserve length scales of deformation that can be used to infer fundamental quantities such as chamber stirring velocity and magma rheology at the time of deformation (Figure 3.1).

Our paper is organized in the following way. In the next section we provide background information about the geology of the TIS and summarize current conceptual models for the origin of ladder dikes. Section 3.3 de-

scribes field observations from our case study on ladder dikes from the TIS. In section 3.4, we briefly describe analogue experiments on the deformation and breakup axisymmetric plumes in a shear flow, and we summarize the theoretical scalings found in Hodge et al. [2012a]. These results are then used to understand the deformation of ladder dikes in the TIS and to make specific predictions for properties such as chamber flow velocity and magma rheology. In section 3.5, we describe our interpretation for the formation of ladder dikes based on our field observations and experimental results reported in Hodge et al. [2012a]. In section 3.6, we conclude and discuss directions for further investigations.

3.2 Ladder dikes in the Tuolumne Intrusive Suite

3.2.1 Geologic setting

The Tuolumne Intrusive Suite, located in the central Sierra Nevada range (California) provides well-exposed sections ($\sim 1000 \text{ km}^2$) of a Late Cretaceous (95 Ma to 85 Ma) batholith. A series of four intrusive units make up the TIS with the most evolved unit in the center [Bateman and Chappell, 1979; Bateman, 1992; Žák and Paterson, 2005]. From oldest to youngest: Kuna Crest granodiorite, Half Dome granodiorite, Cathedral Peak K-feldspar megacrystic granodiorite, and Johnson granite porphyry (Figure 3.2). Preservation of magmatic structures related to flow in the TIS indicates that the host material can have a yield stress (i.e. when the particle volume fraction, $x_V > 0.20$) [Saar et al., 2001]. Although magmatic structures (e.g. schlieren and ladder dikes) are common in all intrusive units in the TIS, they are most prevalent in the Half Dome and Cathedral Peak units [Žák and Paterson, 2005]. We present data from only the Cathedral Peak granodiorite.

3.2.2 What are ladder dikes?

Kinematic indicators for flow in magmas (i.e., “magmatic structures”) in silicic batholiths exhibit a large variety of geometries: ladder dikes, pipes, troughs, and small-scale diapirs, schlieren, and folds [Barrière, 1981; Reid

3.2. Ladder dikes in the Tuolumne Intrusive Suite

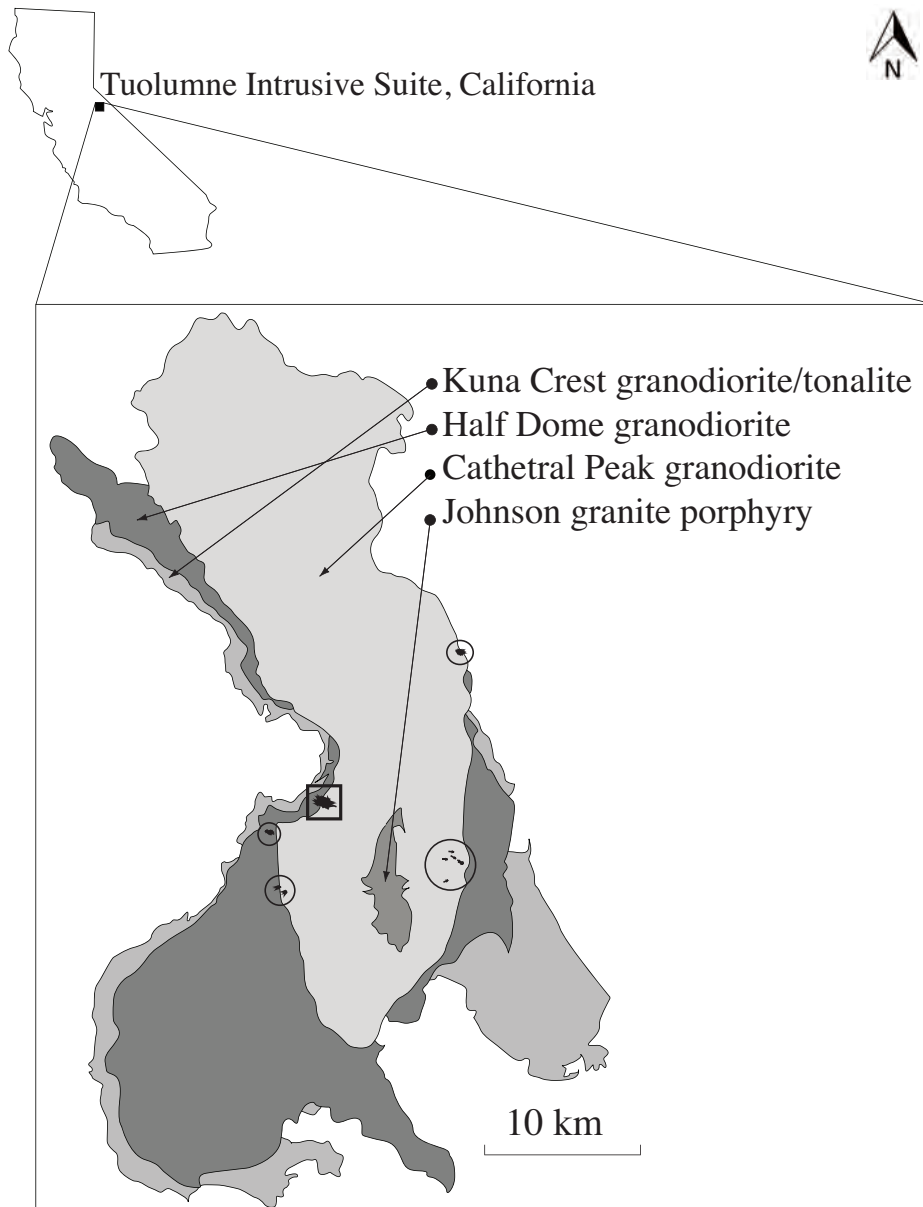


Figure 3.2: General geologic map of Tuolumne intrusive suite (modified from Paterson [2009]). Units are label from oldest (Kuna Crest granodiorite/tonalite) to youngest (Johnson granite porphyry). Small black lines mark ladder dike locations and orientations. Black circles indicate high density of ladder dikes. Black square denotes Glen Aulin outcrop.

3.2. Ladder dikes in the Tuolumne Intrusive Suite

et al., 1993; Wiebe and Collins, 1998; Weinberg et al., 2001; Žák and Paterson, 2005; Paterson et al., 2005; Wiebe et al., 2007; Paterson, 2009]. Among these magmatic structures, ladder dikes are mysterious and their link to magma chamber dynamics is poorly understood [Reid et al., 1993; Weinberg et al., 2001; Paterson, 2009]. According to Reid et al. [1993], ladder dikes occur as “crescent-shaped dark and light layers that appear dike-like in outcrop. Individual curved layers of these ‘ladder dikes’ are nested and for the most part conformable and are younger in the concave direction.” The light and dark layers contain the same petrologic phases (but in different proportions) as the surrounding host granodiorite (Figure 3.1). The dark layers and edges contain magnetite, sphene, hornblende, and biotite, and are lacking plagioclase, alkali feldspar, and quartz. The light layers contain plagioclase with lesser amounts of quartz, k-feldspar, biotite, and minor hornblende [Reid et al., 1993]. Fine-grained mafic layers grade into coarser-grained light layers.

Weinberg et al. [2001] propose an interpretation based on the idea that ladder dikes are preserved plumes of silicic magma that flow relative to the surrounding material. According to their conceptual model, relative motion between fluid layers produces aligned minerals, or schlieren along the plume boundaries [Wilshire, 1969; Barrière, 1981; Abbott, 1989; Weinberg et al., 2001; Wiebe et al., 2007; Paterson, 2009].

Paterson [2009] uses the term “tube” to describe the ladder dikes. This study defines magma tubes as “cylindrical or tube-shaped structures in three dimensions that in sections perpendicular to tube axes display numerous, enclosed (if not removed by subsequent magmatic erosion), elliptical schlieren bounded by layers.” Paterson [2009] subdivides the tube structures into two types: stationary and migrating. The “stationary tubes” appear as roughly symmetric concentric schlieren rings and the “migrating tubes” appear as if a stationary tube migrated, in some cases, tens of meters. The tube structures are present throughout the TIS (initial estimates by Paterson [2009] ~ 1000) and appear to be spatially clustered (0 – 100 tubes per km²).

3.2. Ladder dikes in the Tuolumne Intrusive Suite

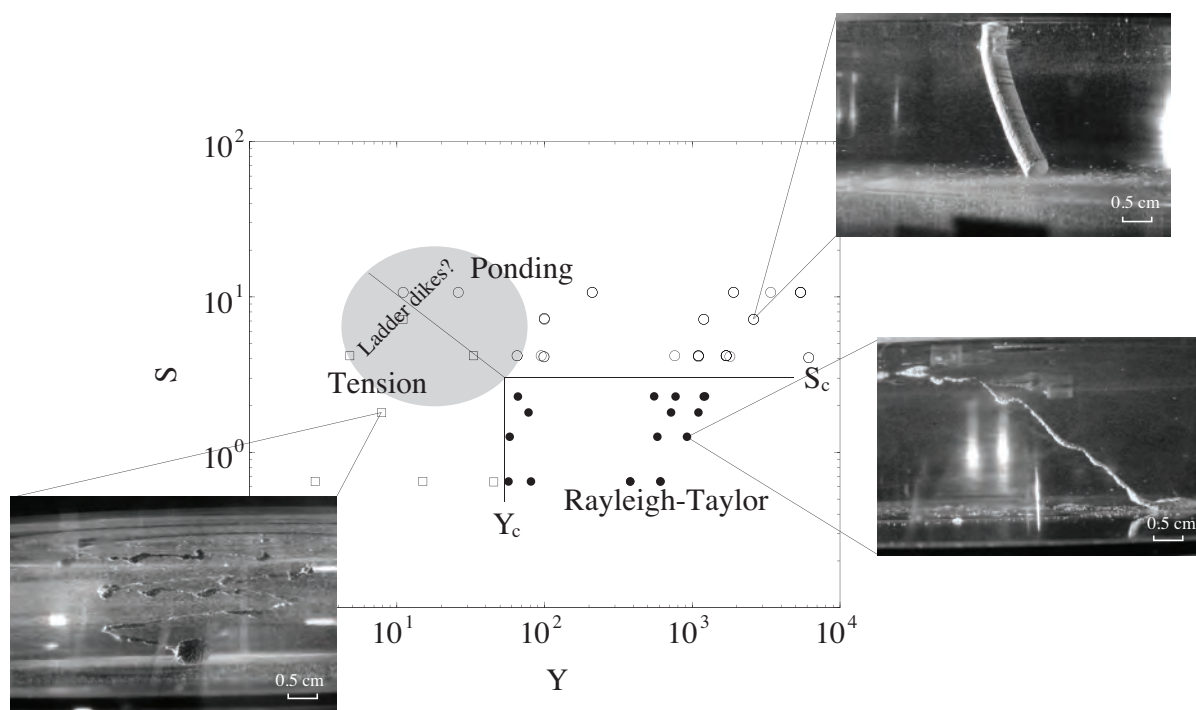


Figure 3.3: Diagram showing injected material behavior from experiments described here and in Hodge et al. [2012a]. Experiments are plotted in terms of dimensionless numbers Y and S . Transitions between the Tension, R-T, and Ponding regimes are shown by the solid lines ($Y_c \sim 40$ and $S_c \sim 3$). Photo insets show examples of injection behavior under different conditions. Gray field denotes predicted $Y - S$ conditions for ladder dikes.

3.2.3 A new quantitative model for the formation and deformation of ladder dikes: Experiments and scaling analysis

In Hodge et al. [2012a], we show that buoyant plumes of polydisperse rigid spheres in corn syrup propagating in a shear flow may breakup or remain intact depending on the rheology of the plume and the intensity of the shearing. Since both the viscosity and yield strength of an injection of magma are related to cooling and crystallization, we use high viscosity (i.e. high particle volume fraction, x_V) suspensions in our experiments. Our laboratory experiments and scaling analysis show that a number of processes acting over distinct timescales govern the major response of a plume to an imposed shear. First, the timescale for a plume to settle (or rise) through the magma chamber is:

$$t_s = \frac{\mu_a h}{\Delta \rho g R_i^2}, \quad (3.1)$$

where μ_a is the viscosity of the ambient chamber, h is the chamber depth, $\Delta \rho = (\rho_i - \rho_a)$ is the density difference between the ambient chamber and the plume, R_i is the plume radius, and g is gravity. A second timescale is that for lateral disaggregation or yielding of the deformed plumes, which has the form:

$$t_y = R_i \sqrt{\frac{\rho_i}{\tau_y}}, \quad (3.2)$$

where τ_y is the yield strength and ρ_i is the density of the plume. The yield strength of the mixture can be written [Wildemuth and Williams, 1984; Hoover et al., 2001],

$$\tau_y = A \left(\frac{x_V / \phi_c - 1}{1 - x_V / \phi_m} \right)^{1/p}, \quad (3.3)$$

where x_V is the particle volume fraction, ϕ_c is the critical packing fraction at which a particle (i.e. crystal) suspension can support an external stress with no deformation, ϕ_m is the volume fraction of solids in closest-packing at which the yield strength approaches infinity, A is a constant that accounts for the total interparticle cohesion, and p depends on the response of the magma to shearing. From Hoover et al. [2001] we set $\phi_c = 0.25$, $p = 1$, and $A = 5.3$,

3.2. Ladder dikes in the Tuolumne Intrusive Suite

since $x_V > \phi_c$ for all of our experiments. In addition, we set $\phi_m = 0.85$ to account for the polydispersivity of the spheres in our experiments (and crystal size distributions in nature) [Yu et al., 1993]. Replacing x_V with experimental values gives yield stresses between 4 – 450 Pa.

Because these plumes are buoyant they can undergo a gravitational Rayleigh Taylor-type instability if they are tilted away from vertical by the imposed shear [e.g. Skilbeck and Whitehead, 1978; Whitehead, 1988]. Consequently a third timescale is that for the growth of such an instability:

$$t_{rt} = \frac{\mu_i}{\Delta\rho g R_i}. \quad (3.4)$$

Here μ_i is the effective viscosity of the plume which for high particle concentrations has the form [Scott and Kohlstedt, 2006]

$$\mu_i = \mu_a \exp(Bx_V), \quad (3.5)$$

where $B = 6$ for our experimental fluids.

Finally, the timescale that takes into account the chamber stirring velocity, V_c has the form,

$$t_f = \frac{R_i}{V_c}. \quad (3.6)$$

We use these four timescales to define two key dimensionless parameters. First, the ratio S takes into account gravitational effects and compares the time for the growth of the first Rayleigh-Taylor instability to the time for the plume to fall through the magma,

$$S = \frac{t_{rt}}{t_s} = \frac{\mu_i R_i}{\mu_a h}, \quad (3.7)$$

which includes a geometrical (R_i/h) and a rheological term (μ_i/μ_a). In our experiments, because R_i and h are fixed, this parameter is essentially a modified viscosity ratio, which only depends on the particle volume fraction through Equation 3.5. Second, we define a ratio Y ,

$$Y = \frac{t_f}{t_y} = \frac{1}{V_c} \left(\frac{\tau_y}{\rho_i} \right)^{1/2}, \quad (3.8)$$

3.3. Ladder dike classification

which compares the timescale for flow to the timescale for disaggregation or yielding by lateral stretching. This parameter quantifies the yielding of a plume of a given rheology depending on the shearing intensity. Qualitatively, low Y conditions promote the disaggregation of the plume, whereas the large yield strength under high Y conditions prevents breakup from lateral stretching.

Our experiments investigate the mechanical and rheological conditions leading to the deformation and breakup of analog rheologically-complex dikes injected as discrete plumes that descend into an underlying imposed shear flow. The main objective of this study is to estimate the rheology and flow dynamics of the host magma at the time of ladder dike deformation. Similar to Paterson [2009], we interpret the ladder dikes to be plumes of magma rising through the host chamber. We interpret their nearly horizontal present-day outcrop expression to be a result of shearing within the chamber. We will argue that the TIS ladder dikes occur in one of two regimes: *ponding* or *breakup* (Figure 3.3). The Ponding regime occurs at high S (> 3) and high Y (> 40), when injections remain intact and undergo little to no deformation. The Tension regime occurs at low Y values (< 40) and S values that increase from ~ 3 as $Y \rightarrow 0$. In this regime an injection yields in tension before a R-T instability can grow, forming discrete particle-fluid blobs that are much smaller than the initial injection diameter and separated by thin filaments of the original mixture. We show that ladder dikes in the TIS undergo one of two types of deformation: Ponding or Tension. We also show that a number of the ladder dikes are close to the regime transition, which suggests that the breakup behavior of these features is sensitive to particularly small changes in crystallinity, as expected from Equations 3.3 and 3.5, and to a lesser extent, chamber flow conditions.

3.3. Ladder dike classification

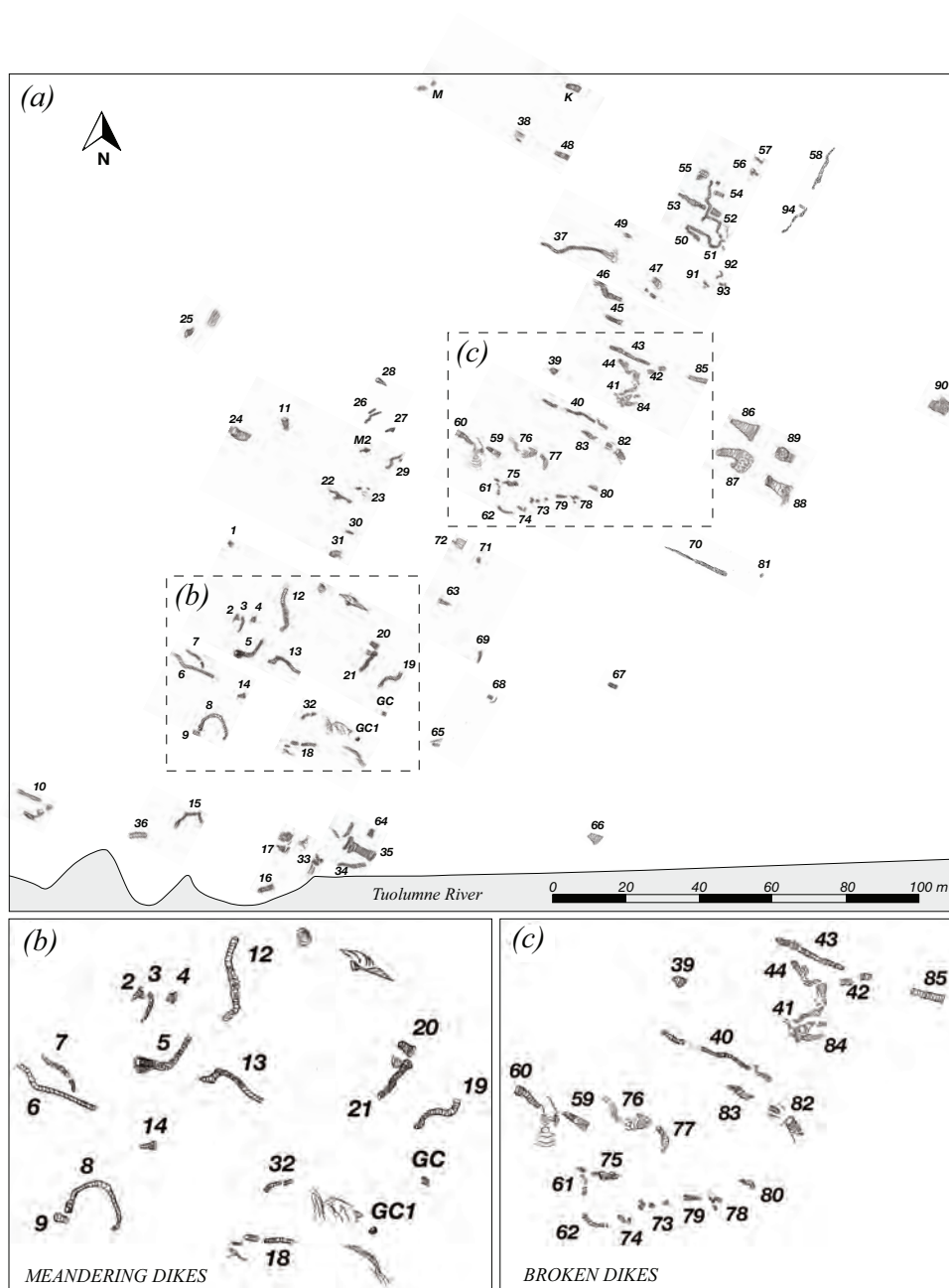


Figure 3.4: (a) Field map from Glen Aulin outcrop with 105 ladder dikes. (b) Detailed zoom of meandering dikes, and (c) detailed zoom of broken dike segments. Map shows the overall orientation and distribution of ladder dikes.

3.3 Ladder dike classification

3.3.1 Dike orientation and geometry

We report the results of a comprehensive field investigation based on 105 ladder dikes in the TIS (Figure 3.4). To analyze the geometry and deformation of these features, we carefully stitch photographs taken along the dike length to make a photomosaic image of each ladder dike (Figure 3.5). These high resolution images are then used to measure the length, width, and orientation, as well as the width of mafic/felsic bands (Figure 3.1). Figure 3.6 shows photographs of a few ladder dikes and emphasizes the large variety of ladder dike geometries observed. Despite this diversity, all of the mapped dikes are located near (~ 30 m) a contact between intrusive units (the Halfdome granodiorite and Cathedral Peak granodiorite), and are oriented N-NW which is roughly perpendicular to the contact (Figure 3.7a). From our mapping, we group together dikes that have similar orientations and geometries and are located within 5 m of one another. The majority of these dikes are between 1 – 10 m in length. Some of the longest ladder dikes that we map are ~ 25 m long and have distinctive meandering map patterns and undulating margins. Figure 3.7b shows the size distribution of all ladder dikes, the majority of which are between 0 – 10 m long. We build a ladder dike classification scheme based on these measurements.

3.3.2 Classification scheme

To compare our field and experimental results in Figure 3.3, we subdivide the ladder dikes into two deformation classes: *broken* and *unbroken* dikes. For broken dikes, we classify them further based on their total length L and total number of segments (Figure 3.1). The total length includes break points along the dike length as long as the segments are less than 10 cm apart (Figure 3.8a). We define three categories: (short) *chains of 2 segments*, (long) *chains of more than 2 segments*, and *complex chains*, where interactions between dikes make interpretation difficult. Within the second group of dikes, we subdivide the dikes according to their total length. We

3.3. Ladder dike classification

define two categories: *isolated* (short) dikes, *meandering* (long) dikes. Finally, out of the 105 ladder dikes observed in this study, we identify a few dikes that have unique features or complex geometries and therefore are unable to be classified. We label these as *complex dikes*.

3.3.3 Group 1: *broken dikes*

A few of the mapped ladder dikes have obvious break-points along their length (see Figure 3.5). In addition to obvious break points that disrupt the long ~ 25 m ladder dikes, a larger scale map pattern (Figure 3.4) reveals that smaller, 1 – 10 m long ladder dikes (e.g. no. 62 – 80) are regularly spaced (1 – 5 m) with similar geometry and orientation. The distribution of ladder dike lengths shows that 45% of the dikes are less than 5 m and 75% are less than 10 m (Figure 3.7b). Interestingly, if we group together neighboring ladder dikes that lie along the same trend and have similar geometries, the sum of these grouped dikes (usually between 2 – 5, with up to 8 segments in each group) measures between 25 – 30 m, which is the length of the longest ladder dikes that we observe at this location. We group dikes based on outcrop patterns from our field map (Figure 3.4). We identify 20 groups in the *broken (long)* category. The groups include any two or more ladder dikes that are located within ~ 5 m of another dike with similar outcrop appearance, geometry, and orientation. The segment length ranges from 0.5 to 12 m. Figure 3.8b shows the distribution of broken dike segment lengths normalized by the reconstructed total length. The number of broken segments in each group ranges from 2 to 9 and we assume that the reconstructed length can be up to 25 m, which is consistent with length of the longest unbroken ladder dikes that we observe.

3.3.4 Group 2: *unbroken dikes*

Almost all ladder dikes in this study have meandering or tortuous map patterns at the meter-scale and irregular margins at centimeter-to-millimeter-scales (Figures 3.5 and 3.6). The irregularities are, however, approximately periodic and the scale of the larger meander-patterns is commonly repeated

3.3. Ladder dike classification

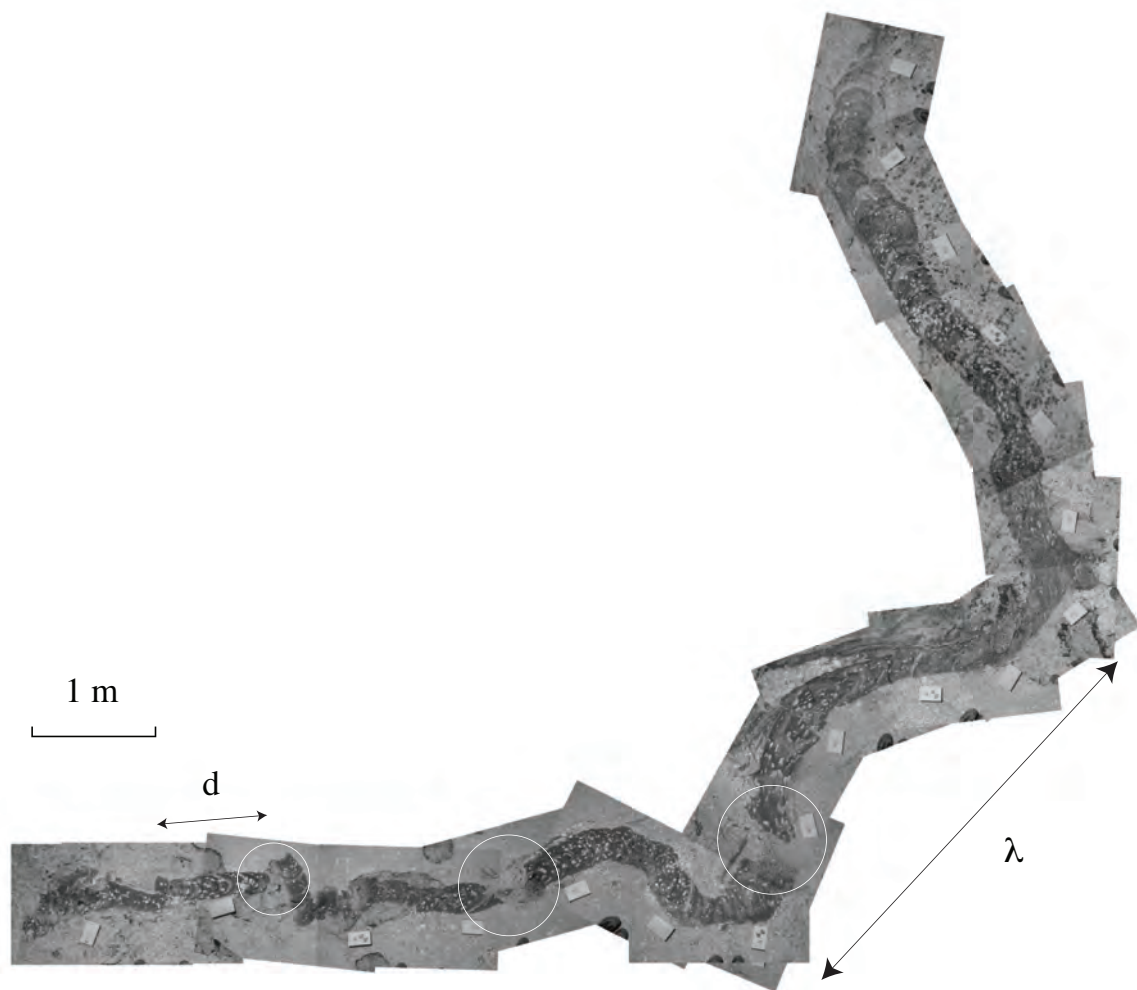


Figure 3.5: Photomosaic showing several meters of one continuous ladder dike (*no.52*) near Glen Aulin, Tuolumne Meadows. Rectangular field notebook (17.8 cm long) shown in each image for scale. White circles highlight breaks along the dike length. The length scale d is measured for broken segments and λ for the dominant wavelength along the dike margins.

3.3. Ladder dike classification

along the length of the ladder dike. With an aim of understanding the mechanisms that govern the spacing of undulations along the dike margins, we measure the wavelength λ between undulation crests using our detailed photomosaics. For each meandering dike, we fit a line to the margins and estimate the power spectrum of the margin tracing [Welch, 1967]. From the spectra, we use a full-width-half-maximum method to estimate the wavelengths of the dominant modes to a 95% confidence level. The distribution of measured wavelength reveals that λ ranges from 0.03 to 2 m, whereas measured widths of mapped ladder dikes ranges from 0.2 to 2.3 m (Figure 3.9). We note that the majority of the ladder dike margins have irregularities that are less than 0.5 m, while the larger-scale meanders are less dominant and range in size from ~ 0.5 to 2 m. The average dike width is approximately 0.5 m. Figure 3.8b (*bottom*) shows the distribution of sinuosity measurements of the *unbroken* dikes.

3.3.5 K-feldspar-rich dikes

We observe a high density of subhedral to anhedral K-feldspar megacrysts (MCs) (1–10 cm) associated with the Glen Aulin ladder dikes. They appear as clusters within the dike margins, or as individual megacrysts, often cross-cutting mafic-felsic banding, and in some cases the margin of the ladder dike (Figure 3.6). The MCs are randomly oriented with alignment parallel to ladder dike banding of crystals smaller than ~ 3 cm. We identify three main subcategories of the K-feldspar-rich dikes. The *long or meandering* dikes have large clusters of K-feldspar MCs within the dike margins. The dense clusters are uniformly distributed and continue along the length of the dike for several meters (e.g. ladder dike no. 70). Where K-feldspar clusters are present, mafic-felsic banding is usually absent. The *isolated* K-feldspar-rich dikes are short (< 10 m) and contain clusters of MCs within the dike margins. The *wide* K-feldspar-rich dikes have thin, wide mafic bands on one end with a large K-feldspar cluster at the other end that gradually transitions into the surrounding Cathedral Peak granodiorite (e.g. ladder dikes no. 87–89). These dikes are up to 8 m wide and range from 10–20

3.3. Ladder dike classification

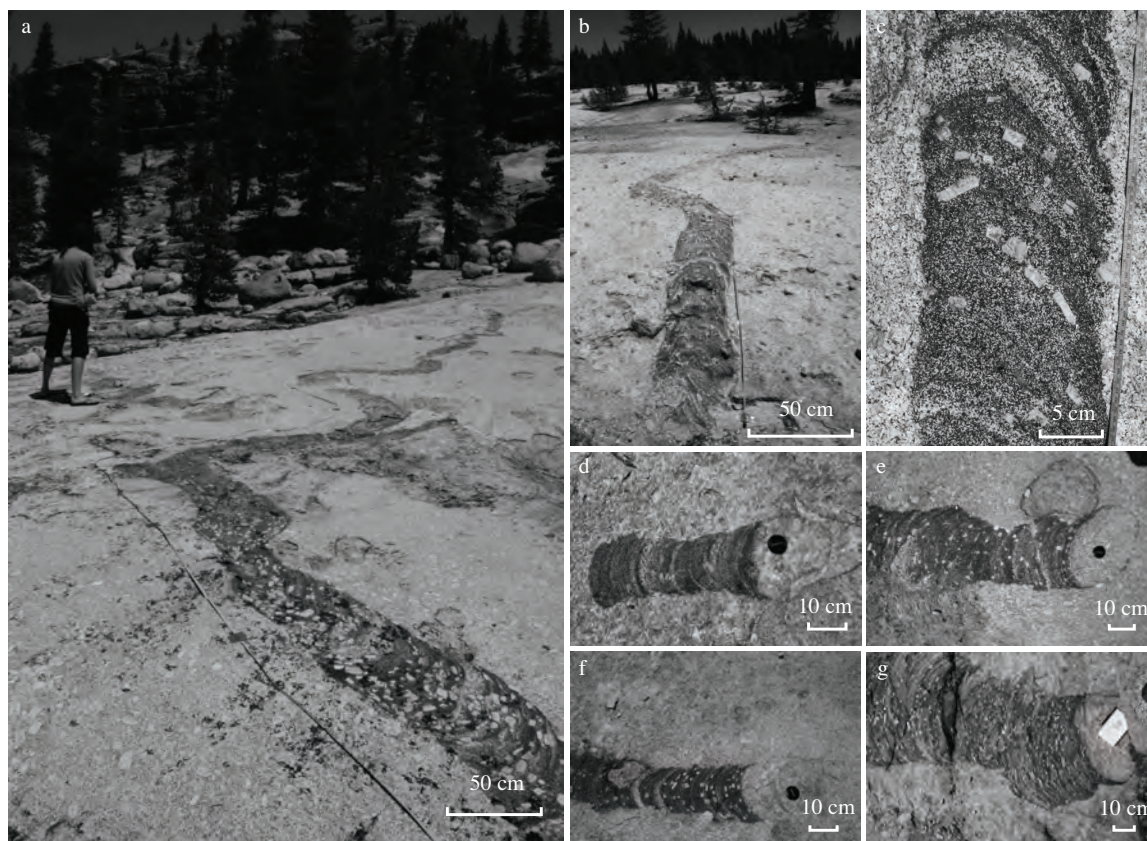


Figure 3.6: (a) – (b) Photos of large-scale meander pattern of ladder dikes near Glen Aulin outcrop. (c) Close-up photo of small-scale irregularities along margin of ladder dike. (d) – (g) Photos of ladder dikes with irregular margins near Glen Aulin, Tuolumne Meadows.

3.4. Comparison with analogue experiments

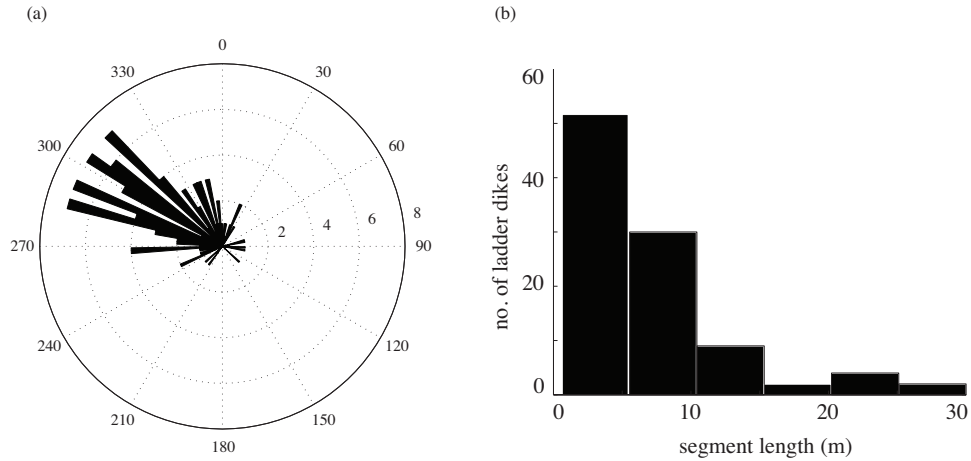


Figure 3.7: (a) Rose diagram of ladder dike orientation data. (b) Histogram of dike length distribution.

m in length.

3.3.6 Mafic-felsic banding

We measure the width of the mafic and felsic bands that make up the ladder dikes (Figures 3.1 and 3.6c-g). In Figure 3.10, we plot the range in widths of the mafic and felsic bands against the length of the ladder dike. The majority of the mafic band widths are between 1 – 6 cm with a few wider bands (20 cm) measured in the shortest dike segments (1 – 10 m long). The felsic bands are mostly between 1 – 10 cm wide with a few thicker (20 cm) band widths. Across all ladder dike sizes (short to long), the mafic bands are thinner than the felsic bands and the longest ladder dikes (> 10 m) have the thinnest bands.

3.4 Comparison with analogue experiments

We use analogue experiments presented in Hodge et al. [2012a] to investigate the extent to which the enhanced viscosity and possibly complex rheology of viscous, crystal-rich plumes govern whether these magmas break up or

3.4. Comparison with analogue experiments

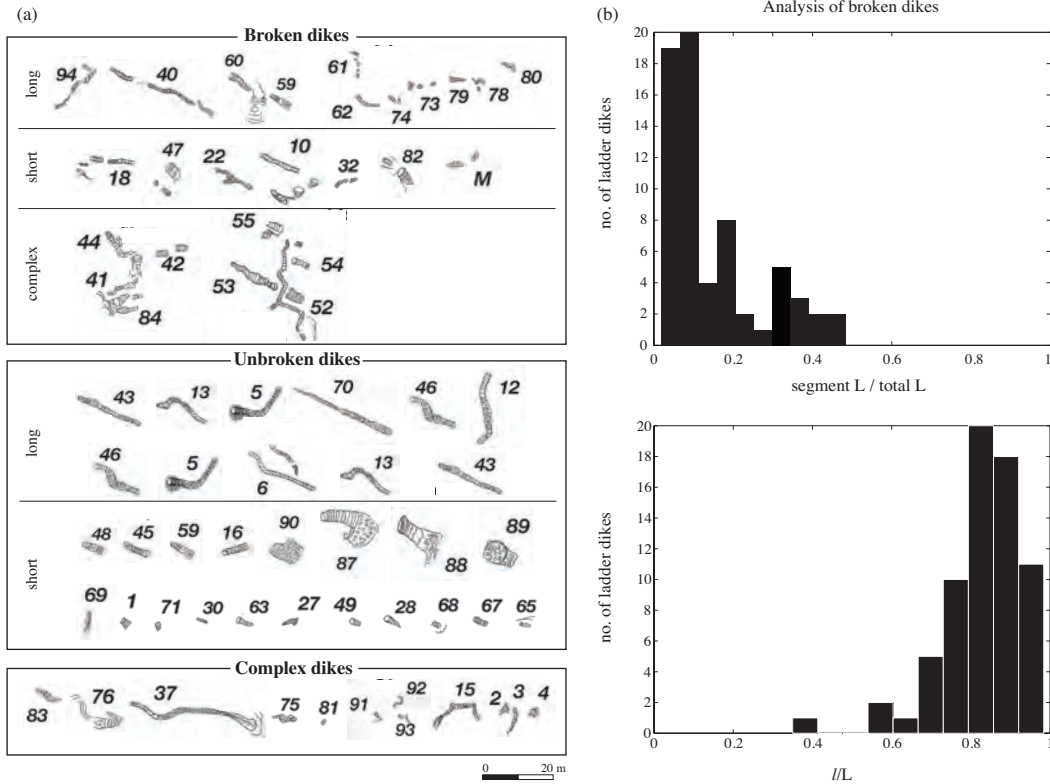


Figure 3.8: (a) Ladder dike classification scheme based on field observations of geometry and size. (b) Histograms (*top*) showing the distribution of broken segment lengths over the reconstructed total length and (*bottom*) the distribution of sinuosity measurements (straight length measured from endpoint to endpoint (l) over the actual meandering length measured through the centerline of the dike (L)) for the *unbroken* group.

3.4. Comparison with analogue experiments

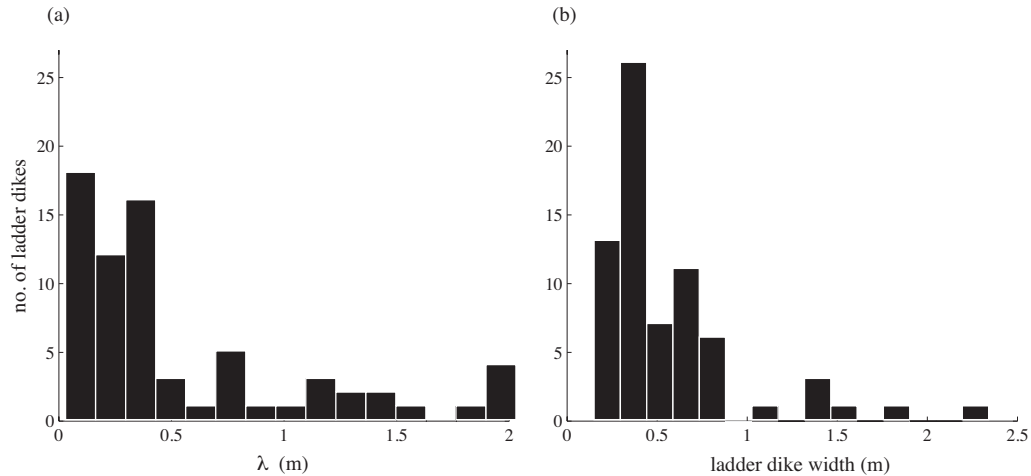


Figure 3.9: (a) Histogram showing λ values for ~ 70 meandering ladder dikes (b) Histogram showing distribution of dike widths for the ~ 70 ladder dikes from which we measure λ .

form ladder dikes in a convecting magma chamber. To capture the effects of solidification on the rheology of magmatic plumes that rise (or fall) in a magma chamber in a straightforward way that can be scaled to the natural magmatic case, we inject buoyant, particle-laden plumes with physical properties that we vary into a lower viscosity simple shear flow (Figure 3.11a). In more detail, we vary the particle concentration and particle size distribution to vary the buoyancy, effective viscosity, and yield strength of the injected plumes. We also vary the strength of the imposed shear in the ambient fluid layer relative to the fall (or rise) speed of the plumes. We quantitatively characterize the deformation of the plumes over a wide range of conditions expected to occur in natural systems.

3.4.1 Experimental results: Constraints on the deformation of ladder dikes

In Hodge et al. [2012a] we show that the stability of our experimental plumes is controlled by the dimensionless parameters S and Y (see Section 3.2.3; Figure 3.3). At low S (< 3) and high Y (> 40), descending plumes are

3.4. Comparison with analogue experiments

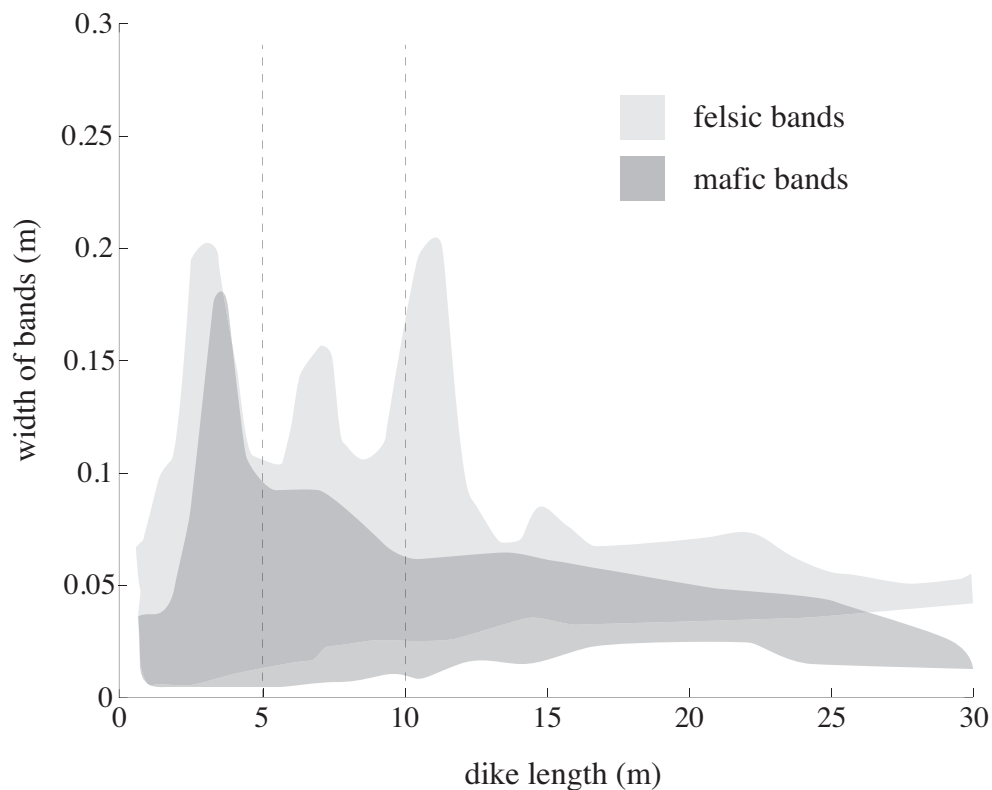


Figure 3.10: Plot of the range in widths of mafic and felsic bands along the length of the ladder dikes vs. the total dike segment length. Dark grey area shows the distribution of width measurements for mafic bands and light grey area shows the distribution of width measurements for felsic bands. Vertical dashed lines mark the division between dike length categories: *short* (< 5 m), *intermediate* (5 – 10 m), and *long* (10 – 30 m)

3.4. Comparison with analogue experiments

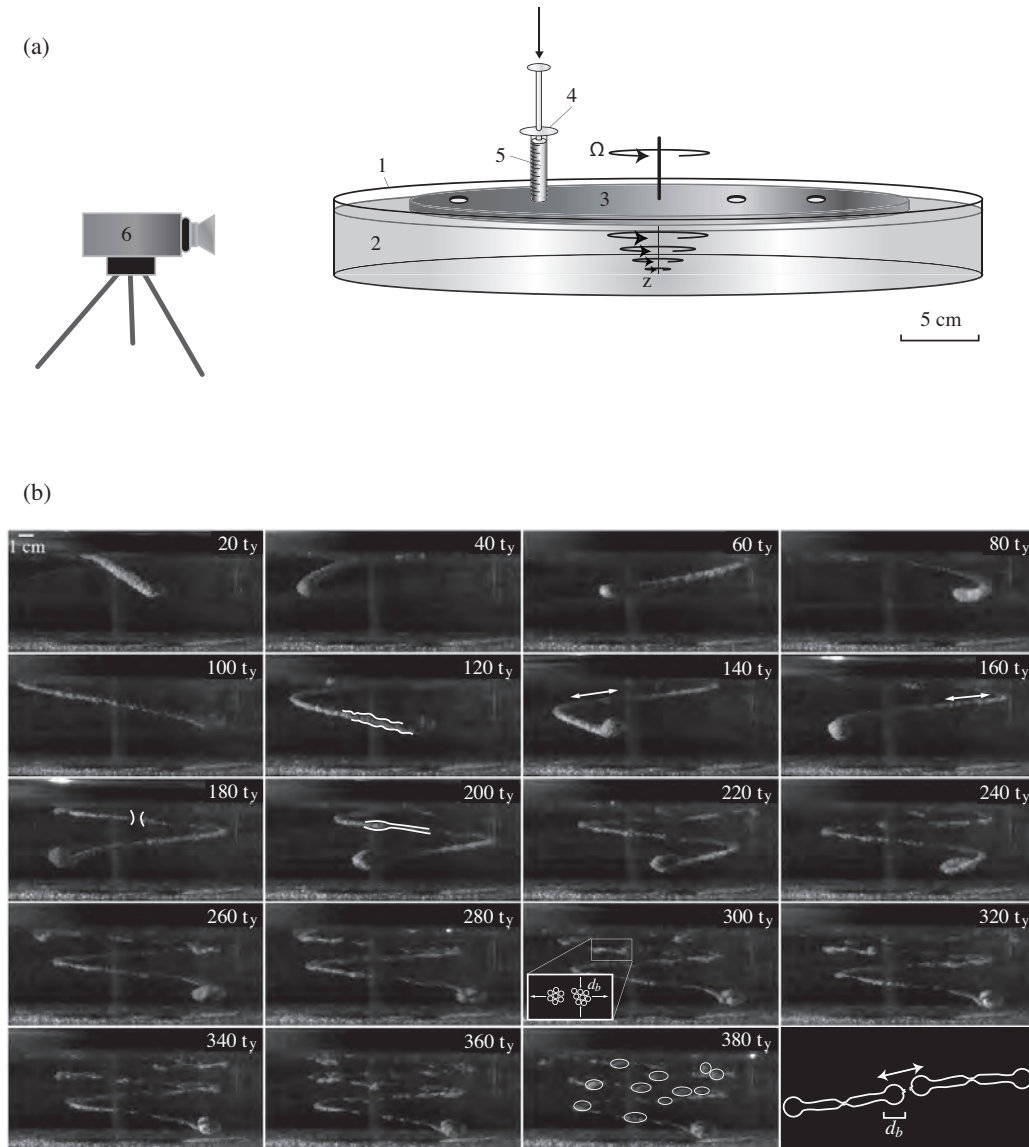


Figure 3.11: Main results from Hodge et al. [2012a]: (a) Cartoon of experimental set-up. (1) tank, (2) corn syrup, (3) upper rotating plate, (4) syringe, (5) particle-corn syrup mixture, (6) high-speed camera. (b) Image sequence showing evolution of injection breakup in the Tension regime experiment. Time is reported in terms of the yield timescale t_y . Image $120t_y$ shows variations in the diameter that are small in comparison to the radius R_i as lateral stretching pulls the injection apart. In images $140 - 160t_y$ small blobs form as yielding becomes the dominant deformation mechanism. The image at $t = 180t_y$ shows the first break in the injection. As the deformation progresses, small blobs of injected material form connected by thin filaments of interstitial corn syrup. The image at $t = 300t_y$ shows discrete blobs forming. Individual blobs are highlighted in the image at $t = 380t_y$.

3.4. Comparison with analogue experiments

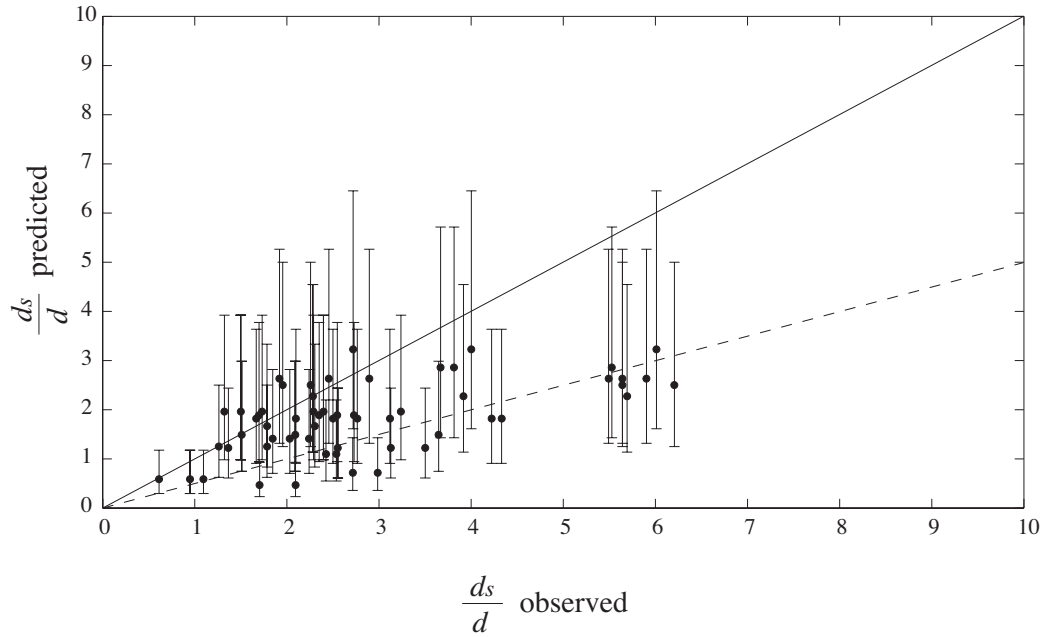


Figure 3.12: Plot of Observed d_s/d values for ladder dikes at Glen Aulin vs. Predicted d_s/d values. The Predicted values are calculated using $\mu_a = 10^6$ Pa·s, $V_c = 10^{-3} - 10^{-1}$ m s $^{-1}$, and $\tau_y = 10$ Pa, which corresponds to $x_V = 0.40$, . Error bars represent the range in Predicted d_s/d values calculated using a range in V_c . The solid line denotes perfect agreement between predicted and observed values, suggesting that these ladder dikes broke up in the Tension regime. The dashed line shows a 2 : 1 relationship between Observed d_s/d and Predicted d_s/d values.

3.4. Comparison with analogue experiments

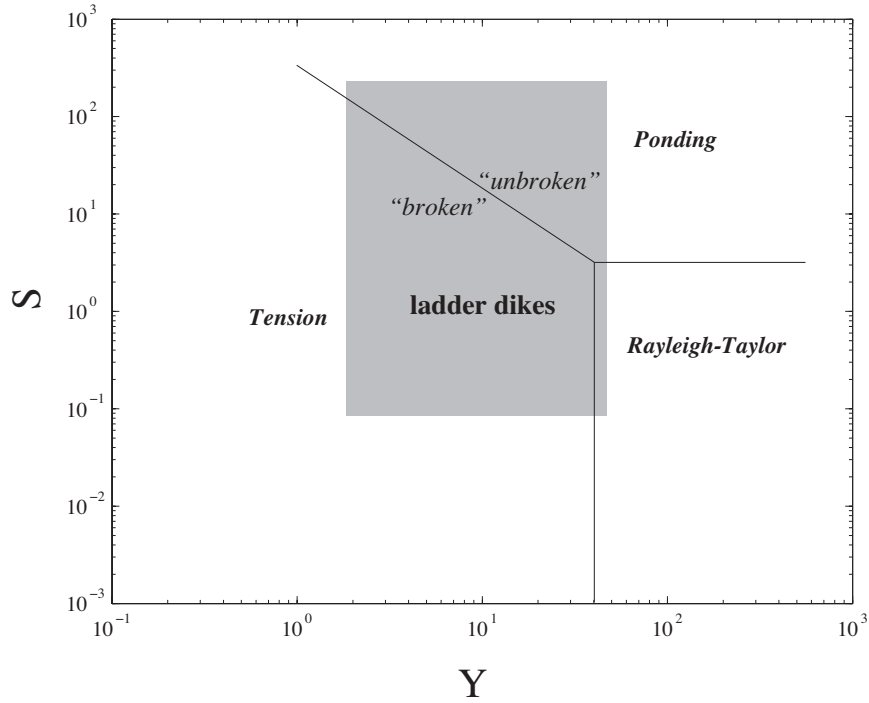


Figure 3.13: $Y - S$ regime plot for magma chambers. Field shows behavior of felsic plumes (broken and unbroken ladder dikes) within a silicic chamber.

stretched and tilted before undergoing R-T instability, forming drips with a wavelength that is comparable to the initial diameter of the injection. At low Y (< 40) and S values that increase from ~ 3 as $Y \rightarrow 0$, plumes yield in tension before an R-T instability can grow, forming discrete particle-fluid blobs that are much smaller than the initial injection diameter and separated by thin filaments of the original mixture. At high S (> 3) and high Y (> 40), injections remain intact, settle through the layer, and pond at the floor. Application of these results to magma chambers shows that the most crystal-rich injections will breakup in the Tension regime (Figure 9 of Hodge et al. [2012a]).

In the Tension regime, the length scale of breakup is a fundamental result that can be used as a tool to interpret magmatic structures. In this regime,

the injection is stretched while the growth of a varicose instability creates periodic variations in diameter until the injection eventually breaks into discrete blobs with a characteristic size d_b separated by interstitial fluid and a thin strand of particles (Figure 3.11b). The evolution of a typical breakup in this regime is illustrated in the time series in Figure 3.11b from experiment V1001. In particular, the image at $120t_y$ shows that the initial stretching leads to the emergence of a varicose instability with a wavelength that is small in comparison to the injection diameter. Here t_y is the timescale for lateral disaggregation or yielding of the deformed plumes defined in Equation 3.2. With increasing deformation ($140 - 160t_y$) small blobs form as yielding of the mixture evolves. At $180t_y$ the injection breaks and by $300t_y$ discrete blobs are apparent (highlighted in image 380 t_y). The images show that deformation begins with lateral stretching that leads, in turn, to pinch and swell or varicose behavior before ultimately yielding.

3.4.2 Quantitative implications for broken ladder dikes

Ladder dikes are usually exposed on planar surfaces, with rare 3D cross-sectional views. It is therefore difficult to assess the nature of these structures in the third dimension. Since we are looking parallel to gravity, we are unable to assess the influence of, for example, a Rayleigh-Taylor instability on the deformation of these features. Consequently, this discussion will focus on the onset of a varicose instability and transition to breakup of the ladder dikes, which is the more relevant regime in nature [Hodge et al., 2012a].

A remarkable discovery of our experiments is the control of the imposed viscous stress and retarding yield stress of the mixture on the average size of large blobs in the Tension regime. We find that the ratio of segment diameter d_s to dike width d follows the scaling (Figure 3.1e),

$$\frac{d_s}{d} = 0.001 \frac{\mu_a V_c}{\tau_y d}, \quad (3.9)$$

where μ_a is the ambient fluid viscosity and V_c is the shear velocity. Here, τ_y is

3.4. Comparison with analogue experiments

the yield strength of the mixture and is defined in Equation 3.3 [Wildemuth and Williams, 1984; Hoover et al., 2001] and 0.001 is an empirical constant.

We use Equation 3.9 to determine whether broken dikes in the TIS were formed by mechanisms occurring in the Tension regime. For this, we calculate an effective diameter for each ladder dike based on the area exposed in outcrop. We compare the calculated diameter values normalized by dike width to theoretical values given by Equation 3.9. The range in yield strength values will depend on the degree of crystallization (or stiffness) of the dike material. We use $\tau_y = 10$ Pa which corresponds to a mean particle volume fraction, $x_V = 0.40$. We calculate a range in μ_i using the melt viscosity model of Giordano et al. [2008] and the suspension viscosity law from Scott and Kohlstedt [2006], which is appropriate at these high crystallinities [Hodge et al., 2012a]. We, thus, take a plausible range of magma viscosities to be $10^5 - 10^8$ Pa·s. A reasonable range of magma stirring velocities is $10^{-3} - 10^{-1}$ m s⁻¹ [Hodge et al., 2012a]. From Equation 3.9, we estimate d_s/d to be between 0.47 and 3.2, which is the same order of magnitude as our field measurements. The relative agreement between our measurements of d_s/d and estimations of d_s/d suggests that the ladder dikes at Glen Aulin, TIS deformed in the Tension regime (Figure 3.12).

3.4.3 The broken/unbroken transition: Why do some dikes break?

Whereas some dikes break up, others remain intact (Figures 3.4, 3.5, 3.8) and, thus, the ladder dikes may preserve a record of varying or transitional Y – S conditions (Figure 3.3). Almost all ladder dikes presented in this study have undulating margins with a wavelength λ that we measure (Figure 3.1 and 3.9). We suspect these axisymmetric undulations are preserved varicose instabilities that did not evolve into discrete blobs. Again, we take $V_c = 10^{-2}$ m s⁻¹ and $\mu_a = 10^6$ Pa s and define a Y – S parameter space for the Tuolumne magma chamber using the following definitions:

$$S = \frac{\mu(x_V)d}{\mu_a H}, \quad (3.10)$$

and

$$Y = \frac{\sqrt{(\tau_y(x_V)/\rho)}}{V_c}. \quad (3.11)$$

Here $H = 10 - 1000$ m is the chamber height, x_V ranges from 0.30 – 0.80, and $d = 0.06 - 3$ m. We estimate S values between $10^{-1} - 10^2$. Using $\tau_y = 1 - 1000$ Pa, $\rho = 2600$ kg m⁻³, and $V_c = 10^{-2}$ m s⁻¹, we estimate Y in the range 10 – 100.

Figure 3.13 shows that ladder dikes probably evolved near the transition between the tension and ponding regimes. In this transition zone, the behavior of each dike is highly sensitive to small changes in x_V , which strongly governs the effective viscosity and yield strength through Equations 3.3 and 3.5 [Hodge et al., 2012a]. An increase in plume viscosity will increase S and an increase in yield strength will increase Y (Figure 3.3 and 3.13). We suggest, therefore, that the broken/unbroken dikes observed in the field reflect dynamical conditions close to the Tension/Ponding transition. In Figure 3.12, we interpret the data that plot on or close to the dashed line to represent incomplete breakup in the Tension regime. Since the ratio d/d_s from field measurements plots on a line that is twice the predicted d/d_s value, we assume that the dikes on this line did not break completely. That is to say, if they broke at least once more, their size (d/d_s) would match the theoretical predictions. The fact that they did not break is possibly related to local variations in τ_y imposed by the amount of crystals in the magma at the time of deformation. We conclude that these dikes must have existed so close to the Tension-Ponding regime transition that a portion of the dike was able to remain in the Ponding regime while another part broke up in the Tension regime.

3.5 The origin of ladder structures

One of the most notable features of ladder dikes is the mafic-felsic banding, which literally resembles the “rungs” of a ladder. In the light of our results, we propose a conceptual model for the formation of ladder dikes (Figure 3.14). Our hypothesis is that the banding occurs in two stages. First, as

3.5. *The origin of ladder structures*

the uniform plume of granodiorite magma propagates vertically through the chamber (Figure 3.14a), a velocity gradient associated with simple shear at the plume's margins promotes the migration of the solid phase toward the edge of the plume (Figure 3.14b) [Leighton and Acrivos, 1987; Huang and Bonn, 2007]. This process results in the formation of a thin schlieren layer by accumulation of mafic minerals at the plume's most outer margin (Figure 3.14c). The second stage occurs when the high concentration of mafic minerals in the thin schlieren layer has a yield strength (Equation 3.3). At this point the schlieren boundary layer has become rigid enough to break under tension from lateral stretching induced by convection in the chamber. This extensive stretching and tilting caused by shearing motions within the chamber finally breaks the outer mafic margin of the plume revealing its flowing granodiorite core (Figure 3.14d). Ladder rungs form because the core of the plume is still flowing when the schlieren boundary layer breaks. However, once the conditions for breakup by tension are met (i.e. $Y < 40$), the ladder dike starts to break at a much larger scale (Figures 3.8a and 3.14e).

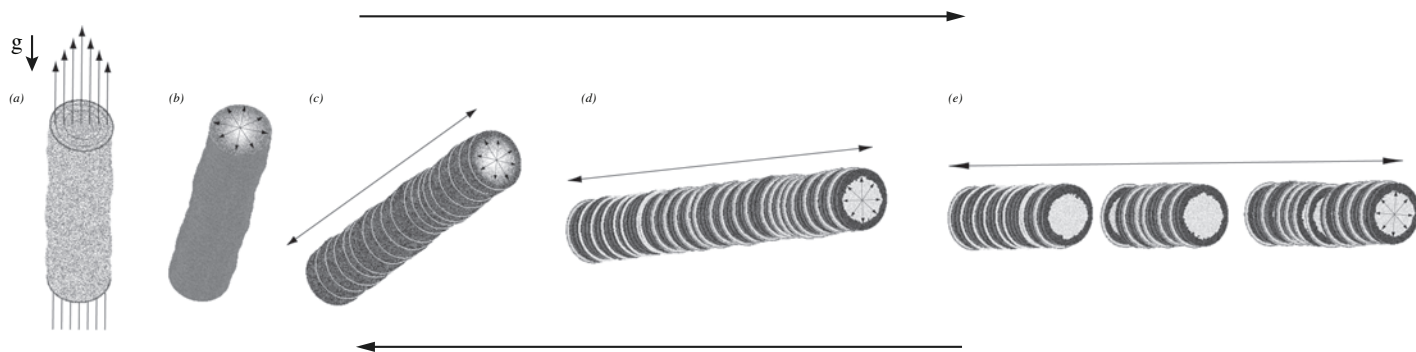


Figure 3.14: Evolution (from left to right) of ladder dike deformation: mafic-felsic banding and large-scale breakup that result from shearing motions within magma chamber as plume becomes tilted away from vertical. Top and bottom arrows show shearing direction. (a) As the cylindrical plume of granodiorite magma propagates through the chamber, a velocity gradient forms due to simple shear; (b) Mafic minerals migrate toward regions of low velocity and concentrate at the plume boundary; (c) Segregation of particles creates a thin schlieren boundary layer that eventually yields under tension and breaks; (d) Progressive stretching eventually breaks the mafic bands into thinner segments, revealing more of the plumes interior felsic phases. (e) Large-scale breakup of ladder dike.

3.6. Conclusion

Our picture that ladder dikes begin as a vertical plume of magma ascending or descending in a velocity gradient related to magma chamber flow is consistent with previous conceptual models [Weinberg et al., 2001; Paterson, 2009]. However, unlike previous studies, our model captures quantitatively and self-consistently key geometrical features of ladder dikes such as their orientation perpendicular to gravity, their periodic mafic-felsic banding, and the occurrence and length scales of their breakup. Previous studies [Weinberg et al., 2001; Paterson, 2009], which suggest ladder dikes form as migrating tubes of magma or stacked troughs are unable to capture these observations and are not consistent with our data analysis. In particular, migrating tubes and stacked troughs would predict two perpendicular directions of flow within the chamber: vertical flow to create the "tube" structure and horizontal flow to cause migration of the tube, which previous models use to explain the stacked mafic-felsic banding characteristic to all ladder dikes. In contrast to this picture, our quantitative analysis of field data that are understood with laboratory experiments and scaling theory show that the ladder dikes may be tilted plumes of magma that are broken up by shearing motions in the magma chamber such that breakup occurs along the dike length in the direction of maximum stretching (Figure 3.14e).

3.6 Conclusion

Our new comprehensive fieldwork combined with analogue experiments and scaling theory supports the following conclusions. Ladder dikes that were once as long as ~ 25 m have been broken up by shearing motions in the chamber prior to solidification. Length-scales of broken dike segments are consistent with a chamber stirring velocity close to $V_c = 10^{-3}$ m s $^{-1}$ and a yield strength up to $\tau_y = 10^3$ Pa of the injected material. Ladder dikes in the TIS formed close to the Tension-Ponding transition and therefore, small or localized variations in crystallinity within the dike margins strongly influenced whether ladder dikes broke-up or remained intact. Mafic-felsic banding is the result of initial segregation of mafic minerals toward the margin of the plume followed by lateral stretching and breaking of the outermost

3.6. Conclusion

mafic layer of the plume to reveal the felsic core. Our combined field, laboratory, and theoretical approach puts a new quantitative mechanical framework to the formation and deformation of ladder dikes. Our model captures the large-scale breakup and orientation, as well as the mafic-felsic banding, however, there remain a number of key questions about ladder dikes. In the future we aim to understand the following: (1) the spatial distribution of K-feldspar megacrysts within the ladder dike margins as well as at the outcrop scale; (2) the spatial clustering of ladder dikes throughout the TIS; (3) their proximity to contacts (specifically where they occur in large clusters) with either host rock or another intrusive unit in the TIS; and (4) their nearly perpendicular orientation to that contact.

Chapter 4

Linking enclave formation to magma rheology

4.1 Introduction

Mafic to intermediate magmatic enclaves hosted in intermediate to silicic igneous rocks provide direct evidence for mechanical mixing of two compositionally and thermally distinct magmas within the same chamber [Eichelberger, 1975; Vernon, 1984; Bacon and Metz, 1984; Bacon, 1986; Didier and Barbarin, 1991; Wiebe et al., 1997; Clynne, 1999]. The wide variety of sizes and shapes of preserved magmatic enclaves highlights the inherent complexity of the interactions between the input and resident magmas (Figure 4.1). Where they are observed, enclaves range in size from a few millimeters to several meters in diameter and their shapes, although often axisymmetric, can also be ovoid, elongate, disk-like, blade-like, or elliptical [Kumar, 2010; Alves et al., 2009; Nardi et al., 2008; Barbey et al., 2008; Feeley et al., 2008; Wiebe et al., 2007; Donaire et al., 2005; Barbarin, 2005; Paterson et al., 2004; Kim et al., 2002; Silva et al., 2000; Akal and Helvaci, 1999; Clynne, 1999; Wiebe and Adams, 1997; Wiebe et al., 1997; Thomas and Tait, 1997; Barbarin, 2005; Pin et al., 1990; Didier and Barbarin, 1991; Bacon, 1986; Vernon, 1984; Bacon and Metz, 1984].

Field observations of enclaves in both intrusive rocks [Vernon, 1984; Didier, 1987; Didier and Barbarin, 1991; Blundy and Sparks, 1992; Wiebe, 1993; Elburg, 1996; Wiebe et al., 1997; Wiebe and Collins, 1998; Paterson et al., 2004; Barbarin, 2005; Kumar, 2010] and lava flows [Bacon and Metz, 1984; Bacon, 1986; Thomas and Tait, 1997; Clynne, 1999; Feeley et al.,

4.1. Introduction

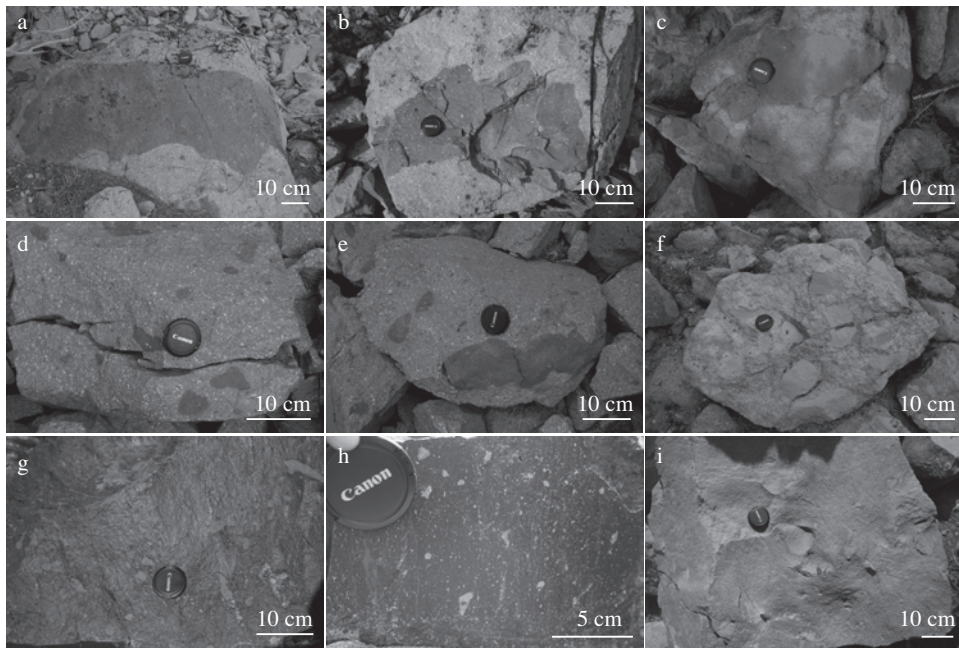


Figure 4.1: Examples of magmatic inclusions from different lava flows. Inclusions size ranges from 1 m down a few mm: (a), (b), (d), and (e) from Chaos Crag, Lassen Volcano; photos (c) and (f) from Mt. Helen Dome, Lassen Volcano; (g) and (h) from Glass Mountain, Medicine Lake Volcano; and (i) from Grotto Cove, Crater Lake.

4.1. Introduction

2008] suggest that they form during the mechanical mixing of the injected and host magmas as a consequence of differences in density, viscosity and possibly yield strength of the two magmas. In a recent analog study, we identify dynamical conditions in which an injected magma may break up to form enclaves (Hodge et al. [2012a], hereafter HCJ12). Here, we apply the results and theoretical scalings for breakup size to understand a new and comprehensive characterization of enclave size distributions and compositional variations in 6 lava flows and domes in the Cascades. Our aim is to use these field data, together with scaling analyses developed in HCJ12 to propose a quantitative connection between the existence and size distribution of enclaves and the rheological properties and dynamical regime of the flow in which they were produced. We have applied a similar approach to understand the structure of deformed and broken “ladder dikes” in the Cathedral Peak granodiorite (Tuolumne Intrusive Suite, California) [Hodge et al., 2012b].

The main goal of this paper is use the results of HCJ12 to link statistical properties of enclave size distributions determined for six Cascade lava flows to the physical properties and flow regimes of the host and injected magmas. A novel result of HCJ12 is that the breakup of meter scale dikes to millimeter or centimeter scale enclaves probably occurs where driving viscous stresses related to host magma flow act against the retarding yield strength of an injected crystallizing mafic magma. Assuming that enclave formation occurs in this restrictive dynamical regime, a key implication that we explore first is that median diameters from enclave size distributions provide quantitative constraints on the yield strength of the enclave magma that are more reliable than estimates from empirical correlations based on crystallinity [Hoover et al., 2001]. The structure of the enclave size distributions also records information about the style and extent of enclave fragmentation, which can, in turn, constrain rheological variations between host and enclave magmas. We use fractal analysis of our enclave size distributions to show that in all six lava flows the progressive fragmentation of the injected magma is self-similar and characterized by a fractal dimension D_f (Section 4.5.2). We find a small but statistically significant dependence of D_f on the effective viscosity ratio

between host and enclave magmas and argue that large variations in effective viscosity lead to a greater extent of breakup.

4.2 Enclaves in 6 Cascade lava flows

4.2.1 Crater Lake

Mount Mazama is a Pleistocene volcano located along the Cascade arc. Approximately 7,700 years ago, a climactic caldera-forming sequence of pyroclastic eruptions created what is the present-day Crater lake [Bacon, 1986; Bacon and Druitt, 1988; Bacon and Lanphere, 2006]. The caldera and surrounding deposits from pre- and post-climactic events, provide a window into a wide range of magmatic processes. Specifically, the eruptive records of Mount Mazama provide evidence for volcanic growth over timescales up to thousands of years. The compositional range of magmas that erupted in the Mount Mazama region spans from 47.6% to 73.2% SiO₂ [Bacon and Lanphere, 2006]. We focus our study on two pre-climactic lava flows and their enclaves (Figure 4.2b): the Holocene Liao Rock rhyodacite flow which contains abundant andesitic enclaves (mostly < 3 cm, but up to 10 cm in diameter) and the Grotto Cove andesite (previously referred to as the 70,000 year old lava flow in Bacon [1986]) which contains mafic andesitic enclaves that range from 2 to 100 cm in diameter.

4.2.2 Medicine Lake Volcano

The Pleistocene to Holocene Medicine Lake volcano is a shield volcano located in the southern Cascade range, California, whose erupted products range from basaltic to high-silica lavas [Grove and Donnelly-Nolan, 1986; Grove et al., 1997; Donnelly-Nolan et al., 2008]. We focus on two lava flows at the Medicine Lake Volcano: the Glass Mountain dacite and the Hoffman flow rhyolite (Figure 4.2c). Both locations provide good evidence for the formation and emplacement of a large volume of silicic melt that is host to very small (millimeter-scale) blobs of mafic magma.

4.2. Enclaves in 6 Cascade lava flows

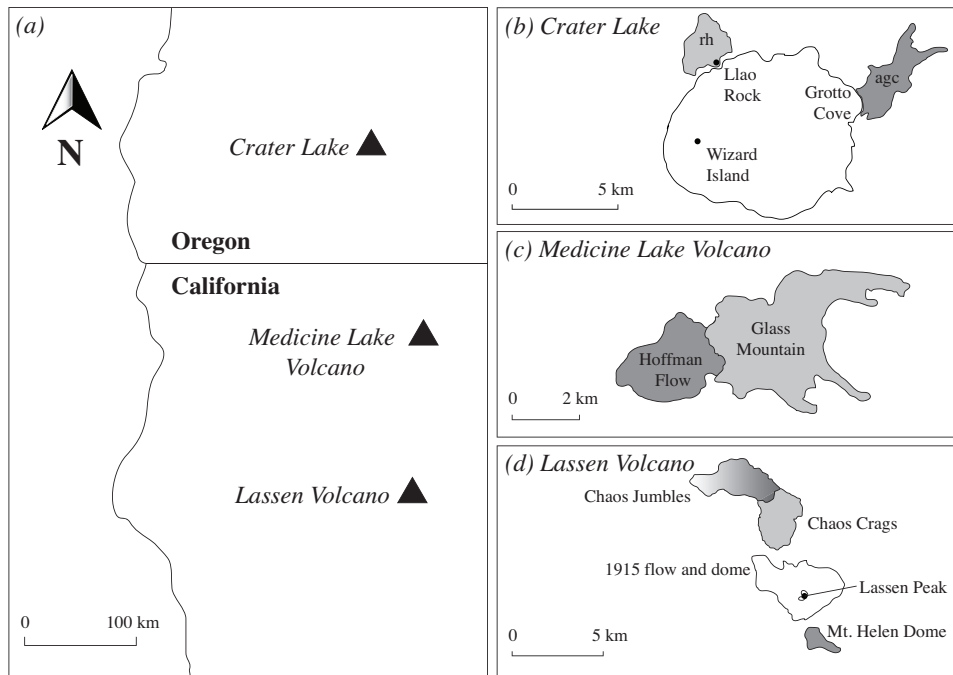


Figure 4.2: (a) Map of southern Cascade volcanos from this study. (b) Modified geologic map of Lloa Rock and the Grotto Cove andesite at Crater Lake from Bacon and Lanphere [2006]. (c) Geologic map of Glass Mountain and Hoffman flow modified from Grove and Donnelly-Nolan [1986]. (d) Modified geologic map of Chaos Crag and Mt. Helen Dome near Lassen Volcano from Feeley et al. [2008].

4.2.3 Lassen Volcano

The Lassen Volcanic Center is a Pleistocene to Holocene stratovolcano located in the Southernmost part of the Cascade range, California (Figure 4.2a & c). The Holocene Chaos Crags comprise a series of six dacite to rhyodacite domes that represent a 1100 year old eruptive sequence [Clynne, 1999]. The Crags Domes highlight the interaction between mafic and felsic magmas common in the Lassen Volcanic Center [Tepley et al., 1999]. The rhyodacite to dacite lavas that make up the six domes (A-F) are host to basaltic to andesitic enclaves. The enclaves range in size from approximately 1 to 50 cm in diameter with some as large as 150 cm [Heiken and Eichelberger, 1980]. In addition to the Chaos Crags Dome C, our work focuses on the Pleistocene Mount Helen dacite dome, another well-studied example of mafic-silicic interactions at the Lassen Volcanic Center. The Mount Helen dome is host to abundant mafic enclaves that range in size from a few millimeters up to 1 meter in diameter [Feeley et al., 2008].

4.3 Methods

We chose six Cascade lava flows based on their high abundance of magmatic enclaves (Figures 4.1 and 4.2). Our goal was to sample a range in host (rhyolite to andesite) and enclave (andesite to basalt) compositions. The data presented in this paper are from two lava flows at each location. At Crater Lake, we took measurements of andesite enclaves in the Llao Rock rhyodacite and mafic andesite inclusions in the Grotto Cove andesite. The enclaves in the Llao Rock flow range in size from a few millimeters up to 12 cm in diameter; whereas, the andesite of Grotto Cove hosts large mafic andesite enclaves that are up to 40 cm in diameter (Figure 4.3). At Medicine Lake Volcano, CA, the Glass Mountain dacite hosts small (0.1 – 12 cm in diameter) enclaves of basaltic-andesite and the rhyolite of the Hoffman Flow is host to anhydrous basaltic enclaves that range in size from a few millimeters up to 20 cm in diameter. At Lassen Volcano, the Mount Helen dacite dome and the rhyodacite Dome C of the Chaos Crags both host large

4.3. Methods

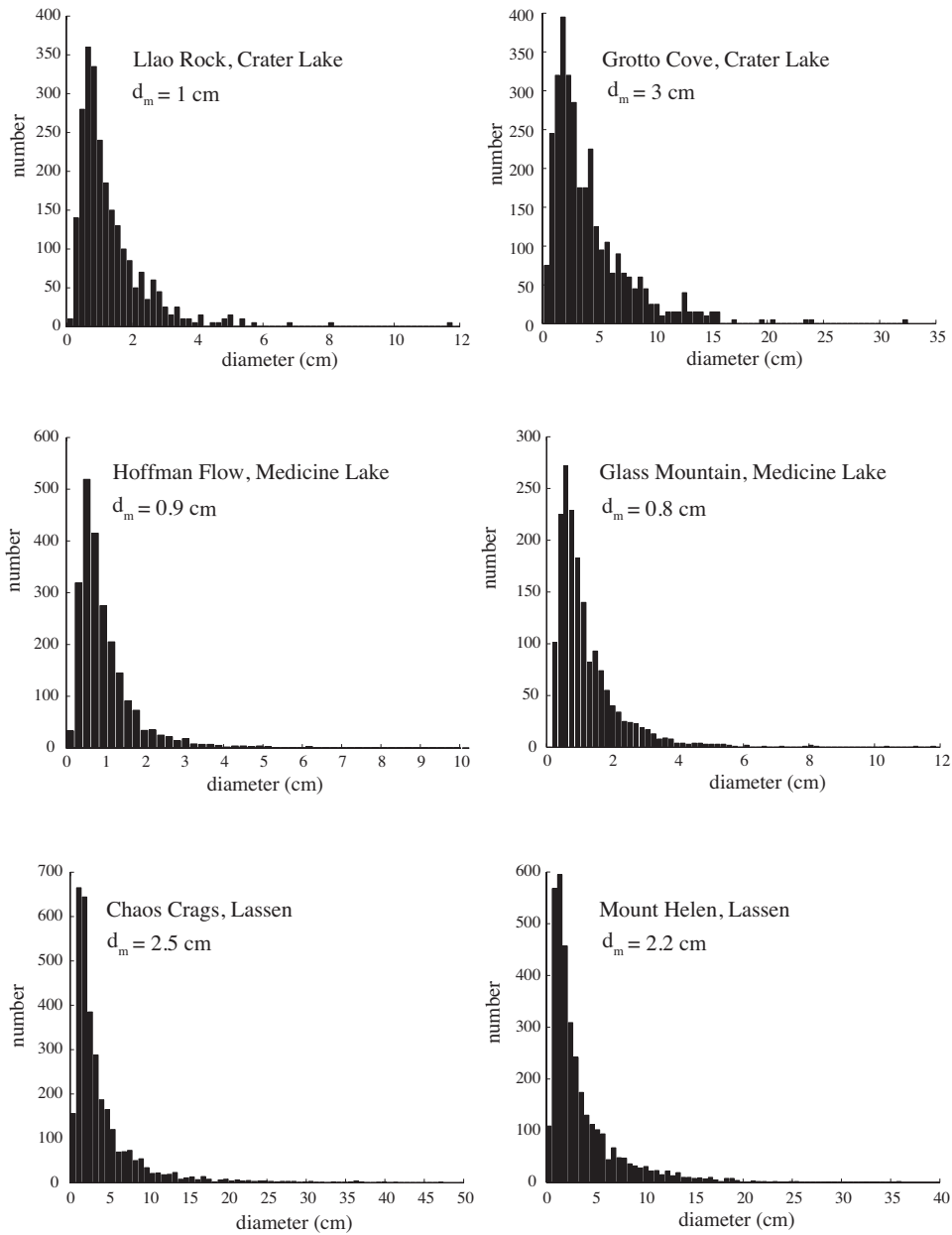


Figure 4.3: Enclave size distribution plots from our field locations. We calculate a diameter from the measured area of each enclave. The longest axis of some of the larger ellipsoidal enclaves is not represented in this plot as we use a spherical shape to convert the area to a diameter. In general, the largest enclaves (longest long axis) from each location is approximately twice the length of the largest diameter shown here. d_m is the median enclave size in each lava flow.

(up to 50 cm in diameter) enclaves of basaltic andesite (Figure 4.3).

4.3.1 Field methods

To sample both the smallest (millimeter to centimeter-scale) and largest (meter-scale) enclaves in a statistically meaningful way, we took outcrop photos at several different scales (a few centimeters up to tens of meters). Our sampling approach was to carry out multiple parallel traverses in which two people used different cameras to image the same section of outcrop. To sample km-scale sections of each lava flow, we combine data from several such traverses. Our cumulative dataset for all six locations comprises nearly 5000 enclaves.

4.3.2 Image analysis

We use ImageJ to analyze approximately 2000 digital photographs of enclaves. In each photo, we first carefully hand-trace the edges of individual enclaves. Next, we find the area A of each enclave and estimate an effective diameter $d = \sqrt{A}$, which is an appropriate average value given the remarkable variability and complexity in enclave shapes (Figure 4.1). Our size distributions (Figure 4.3) all exhibit a positive skew with most of the data to the left of the mean enclave diameter. Thus, we take the median enclave size d_m as a representative of each size distribution.

4.3.3 Fractal analysis

Fractal analysis is a common method for identifying the self-similar fragmentation of Earth materials from initially large to small length scales (e.g. Matsushita [1985]; Turcotte [1986]; Sammis et al. [1986]; Storti et al. [2003]; Gonnermann and Manga [2005]; Perugini et al. [2006]; Perugini et al. [2011]). Here, we use the word fragmentation to refer to the breakup of order 1 to 10 m wide mafic dikes into mm to cm sized enclaves. Previous studies demonstrate that enclaves preserved in igneous rocks have size distributions that exhibit fractal behavior [Perugini and Poli, 2000; Holtz et al., 2004; Ventura et al., 2006; Perugini et al., 2007]. For our unimodal distributions,

we find a power law dependence of the total number of fragments N larger than d_m such that

$$N(d > d_m) = kd^{-D_f}, \quad (4.1)$$

where d is the fragment dimension, d_m is the median enclave size in the distribution (Figure 4.3), k is a constant, and D_f is the fractal dimension of the size distribution [Mandelbrot, 1982]. This relationship shows that the breakup of big fragments into smaller fragments is a length scale-invariant process. That is, where size distributions are fractal the implication is that the same physical process governing deformation and breakup is acting at all length scales. To determine the fractal dimension D_f for our size distributions, we first take the logarithm of Equation 4.1:

$$\log(N) = -D_f \log(d). \quad (4.2)$$

We then determine D_f from the slope of the data in $\log(1/d)$ vs. $\log(N)$ space (Figure 4.6).

Before we search for fractal behavior in the enclave size distributions it is useful to bin the data to reduce the variance in d . Bin widths for d are chosen such that the best fit to the data in a least-squares sense gives a sum of the residuals $R^2 > 0.8$. Fits to the binned data from all 6 flows give $1.8 < D_f < 2.5$ (Figure 4.6). However, a closer inspection of the results shows that the Grotto Cove, Chaos Crag, and Mount Helen enclaves are characterized by a smaller fractal dimensions ($D_f = 1.8 \pm 0.5$) and a larger median enclave size ($2 \leq d_m \leq 3$ cm) than the enclaves measured in the Llao Rock flow, Glass Mountain and Hoffman flows ($D_f = 2 \pm 0.5$ and $0.5 \leq d_m \leq 1$ cm). We return to this observation in Section 4.5.2.

4.3.4 Physical properties of host and enclave magmas from compositional data

In all 6 flows there is local variability in enclave composition and textures, which many previous studies have attributed to differences in in-

4.3. Methods

truding magma composition and/or enclave formation processes [Grove and Donnelly-Nolan, 1986; Bacon, 1986; Bacon and Druitt, 1988; Tepley et al., 1999; Feeley et al., 2008]. We take an average composition for each lava flow for both the host and enclave material, assuming that these compositions are essentially similar to the initial host and injected magmas. Local variability relative to these average compositions obviously introduces a variance that affects estimates of the density and effective viscosity of the host and injected magmas. However, these variations are very small in comparison to the much larger differences between the average compositions of the host and injected magmas and do not affect the results or the conclusions of this study.

We use MELTS and Rhyolite-MELTS to estimate a maximum temperature for the host and enclave magmas. For these calculations, we use the temperature at which a minimum solid fraction (i.e. phenocryst content observed in the field) is present in the melt. In order to model the crystallization path for each magma, we model the cooling history for each magma with MELTS and Rhyolite-MELTS using the compositional data in Table 1 [Gualda et al., 2012; Feeley et al., 2008; Kinzler et al., 2000; Tepley et al., 1999; Asimow and Ghiorso, 1998; Ghiorso and Sack, 1995; Bacon and Druitt, 1988; Bacon, 1986; Grove and Donnelly-Nolan, 1986; Eichelberger, 1980]. We use the host temperature reported in Table 1 as a lower-bound for the enclave magma temperature range, assuming that this is the minimum possible temperature the injected magma will reach as it mixes with the host. We calculate melt viscosities with the Giordano et al. [2008] viscosity calculator. The effective viscosity of the host magma is calculated using the phenocryst content observed in the field [Scott and Kohlstedt, 2006]. We estimate a lower and upper bound for the effective viscosity [Scott and Kohlstedt, 2006] and yield strength [Hoover et al., 2001] of the enclave magmas, using two different crystallinities. To establish a lower bound for the enclave magma crystallinity, we use the phenocryst content observed in the field. To obtain an upper bound for the enclave magma crystallinity, we use MELTS to calculate the solid fraction present in the magma when it cools to the temperature of the host magma. We note that this assumption over-

4.3. *Methods*

estimates the minimum-temperature of the enclave magma, as the timescale for breakup of the injected magma is less than that for thermal equilibration between the host and enclave, for all enclaves larger than a few millimeters.

<i>Host</i>	Rock type	SiO₂ (wt.%)	Temp. (°C)	x_V (%)	H₂O (wt.%)	density (g cm⁻³)	Ref.
Llao Rock	rhyodacite	70.30	930	6-14	3-5	2.22	1
Grotto Cove	andesite	61.60	1020	20-30	3-5	2.27	2
Glass Mountain	dacite	65.50	900	1-3	3-5	2.29	3, 4
Hoffman Flow	rhyolite	71.20	850	5-10	3-5	2.24	3, 4
Chaos Crags	rhyodacite	68.88	980	30-35	2-4	2.23	5, 6
Mount Helen	dacite	64.94	1025	25-30	2-4	2.40	7
<i>Enclave</i>							
Llao Rock	andesite	53.80	930-1095	1-50	2-4	2.2-2.3	1
Grotto Cove	mafic andesite	60.00	1020-1110	1-50	1-3	2.2-2.3	2
Glass Mountain	basaltic-andesite	53.80	900-1175	1-73	1-5	2.3-2.5	3, 4
Hoffman Flow	basalt	49.60	850-1230	1-90	0.10	2.7-3.1	3, 4
Chaos Crags	basaltic-andesite	56.74	980-1050	1-50	1-3	2.3-2.4	5, 6
Mount Helen	basaltic-andesite	58.60	1025-1050	1-45	1-3	2.3-2.4	7

Table 4.1: Physical properties of six lava flows. SiO₂ wt.% and H₂O wt.% data from: (1) Bacon and Druitt [1988], (2) Bacon [1986], (3) Grove and Donnelly-Nolan [1986], (4) Kinzler et al. [2000], (5) Tepley et al. [1999], (6) Eichelberger [1980], (7) Feeley et al. [2008]. We report x_V for the host rocks as the range in phenocryst content and x_V for the enclaves as a range between phenocryst content (lower bound) and calculated solid fractions using MELTS and Rhyolite-MELTS (upper bound) that would crystallize as the enclave magma cooled to the initial temperature of the host magma [Gualda et al., 2012; Asimow and Ghiorso, 1998; Ghiorso and Sack, 1995]. We use Rhyolite-MELTS and MELTS to constrain the host temperature as the temperature at which the minimum solid fraction (x_V lower-bound) is present in the melt. We report the range in enclave temperature with the minimum constrained by the host temperature and the maximum constrained using MELTS as the temperature at which the minimum solid fraction x_V is present in the melt.

4.4 A model for linking magma rheology to enclave sizes

HCJ12 show that buoyant, rheologically complex plumes ascending or descending in a very viscous shear flow can be strongly deformed or broken up, depending on the flow regime in the magma chamber (Figure 4.4). Whether and to what extent these analog dikes become fragmented depends on a flow regime defined by two key parameters (Figure 4.5). The parameter S is the ratio of the timescale t_{rt} for the growth of a gravitational Rayleigh-Taylor-type (R-T) instability on an injected plume that is tilted with respect to gravity [Skilbeck and Whitehead, 1978] to the timescale t_s for an injection to rise or sink through the magma chamber:

$$S = \frac{t_{rt}}{t_s} = \frac{\mu_i d_i}{\mu_h h}, \quad (4.3)$$

Here, h is the chamber depth, d_i is the plume width, μ_h is the viscosity of the host magma, and μ_i is the effective viscosity of the plume which for high particle concentrations has the form [Scott and Kohlstedt, 2006]

$$\mu_i = \mu_h \exp(Bx_V), \quad (4.4)$$

where x_V is the particle volume content, and $B = 6$ for our experimental fluids.

The parameter Y is the ratio of the timescale for shearing of a rheologically complex dike of width d_i by flow in the magma chamber t_f to the timescale for lateral disaggregation or yielding of the dike t_y :

$$Y = \frac{t_f}{t_y} = \frac{1}{V_c} \left(\frac{\tau_y}{\rho_i} \right)^{1/2}. \quad (4.5)$$

Here V_c is the characteristic flow velocity of the host magma, ρ_i is the density of the injected dike, and τ_y is the yield strength, which depends on the volume

4.4. A model for linking magma rheology to enclave sizes

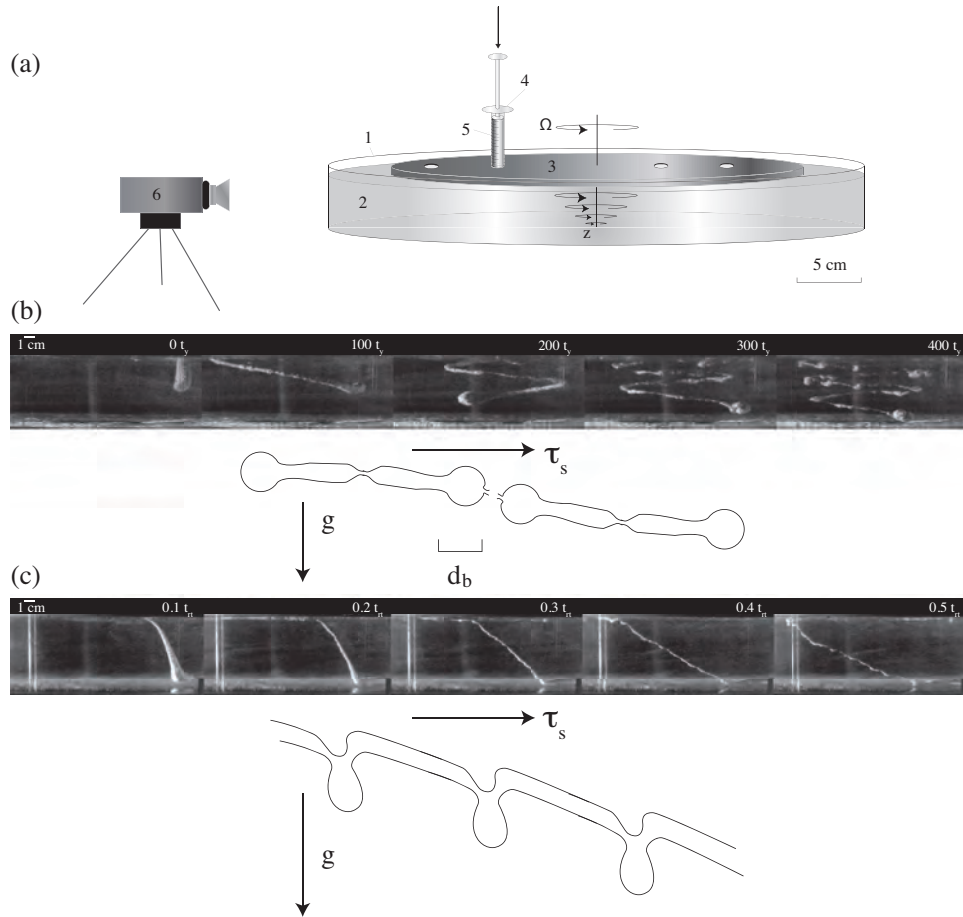


Figure 4.4: Main results from Hodge et al. [2012a]: (a) Cartoon of experimental set-up. (1) tank, (2) corn syrup, (3) upper rotating plate, (4) syringe, (5) particle-corn syrup mixture, (6) high-speed camera. (b) Image sequence showing evolution of injection breakup in the tension regime experiment. Time is reported normalized to the yield timescale t_y . Image $200t_y$ shows variations in the diameter that are small in comparison to the radius R_i as lateral stretching pulls the injection apart. In images $300t_y$ and $400t_y$ small blobs form as yielding becomes the dominant deformation mechanism. The cartoon highlights the initial varicose instability which eventually leads to breakup into blobs with a characteristic size d_b . (c) Image sequence during R-T regime experiment. Time is reported normalized to t_{rt} . The images show the formation of a gravitational instability accompanied by lateral stretching. Stretching in the thin tail of the injection is shown by the cartoon zoom in the image at $t = 0.3t_{rt}$. The instability begins at $t = 0.4t_{rt}$ and progresses as material is pulled laterally along the injection into the drips. The cartoons show the dominant forces acting to deform the plume. In both cartoons, g is gravity and τ_s is the horizontal shear stress.

4.4. A model for linking magma rheology to enclave sizes

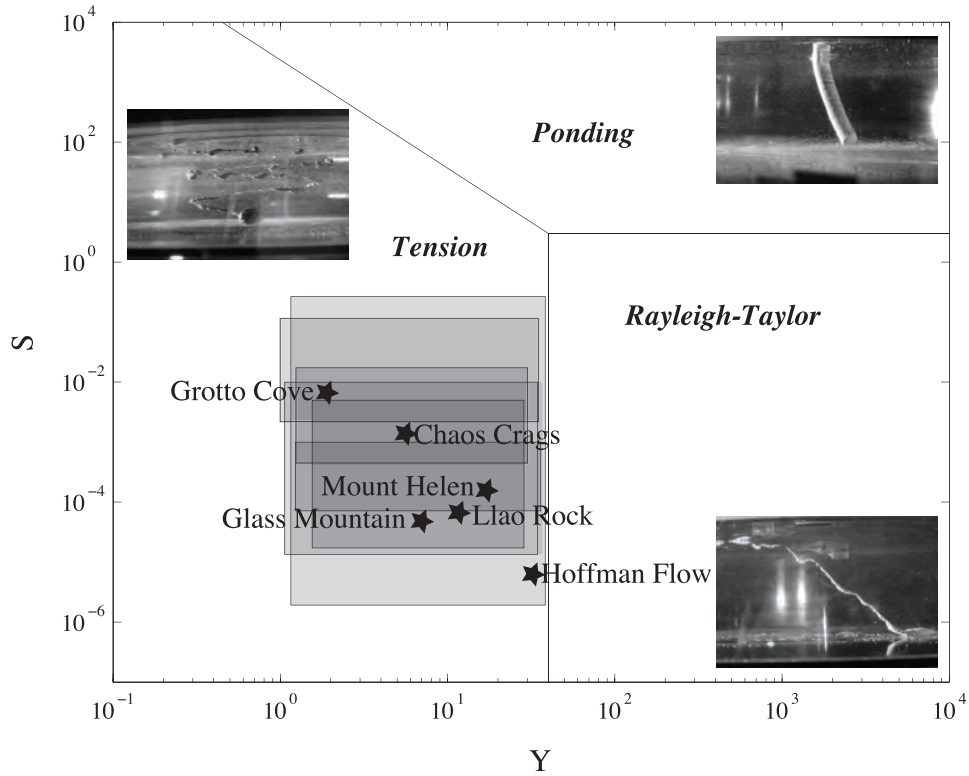


Figure 4.5: Y-S regime diagram for enclaves in lava flows. Fields show the range in the Y and S parameters that account for the chamber conditions (geometry and flow dynamics), the viscosity ratio between enclave and host magmas, and the yield strength of the injected magma that we calculate using a range in τ_y that is based on the possible range in solid fraction in the enclave magma (phenocryst content as a lower bound and solid fraction present in the magma as it reaches the host magma temperature as an upper bound). The stars within each field indicate Y values that we obtain using a yield strength value calculated from scaling laws in Hodge et al. [2012a] which takes into account the breakup length scale d_m that we measure in the field. Photo insets show examples of plume behavior under different conditions observed in the experiments in Hodge et al. [2012a].

fraction of crystals and has the form [Hoover et al., 2001]

$$\tau_y = A \left(\frac{x_V/\phi_c - 1}{1 - x_V/\phi_m} \right)^{1/p}. \quad (4.6)$$

Here ϕ_c is the critical packing fraction at which a particle (i.e. crystal) suspension can support an externally-imposed yield stress with no deformation, ϕ_m is the volume fraction of solids in closest-packing at which the yield strength approaches infinity, A is a constant that accounts for the total interparticle cohesion, and p depends on the response of the magma to shearing. From Hoover et al. [2001] we set $\phi_c = 0.25$, $p = 1$, and $A = 5.3$, since $x_V > \phi_c$ for all experiments. In addition, we set $\phi_m = 0.85$ to account for the polydispersivity of the spheres in the experiments (and crystal size distributions in nature) [Yu et al., 1993]. Qualitatively, disaggregation of a strong analog dike will occur for $Y < 40$, whereas it will remain intact for larger Y conditions.

4.5 Results and Discussion

4.5.1 A Y-S regime for enclaves in lava flows

HCJ12 show that dike fragmentation can occur in two regimes that give distinct enclave scale lengths (Figures 4.4 and 4.5). Whereas the growth of gravitational Rayleigh-Taylor-type instabilities can cause tilted dikes to break up in the form of drips with a scale length that is a few times the initial width of a dike injection, disaggregation in the tension regime leads to blobs with a scale length much smaller than the initial dike injection. Assuming that the mafic to intermediate magma injections ultimately giving rise to the enclave size distribution shown in Figure 4.3 are 1-10 m wide dikes [Petford et al., 1993], the data suggest that the magma mixing dynamics preserved in these lava flows, occurred in the tension regime. In this regime, dike breakup occurs primarily as a result of viscous stresses related to flow in the host chamber acting against the yield strength of crystallizing dike magmas. In comparison to the initial dike injection width d_i , the resulting blobs have a

4.5. Results and Discussion

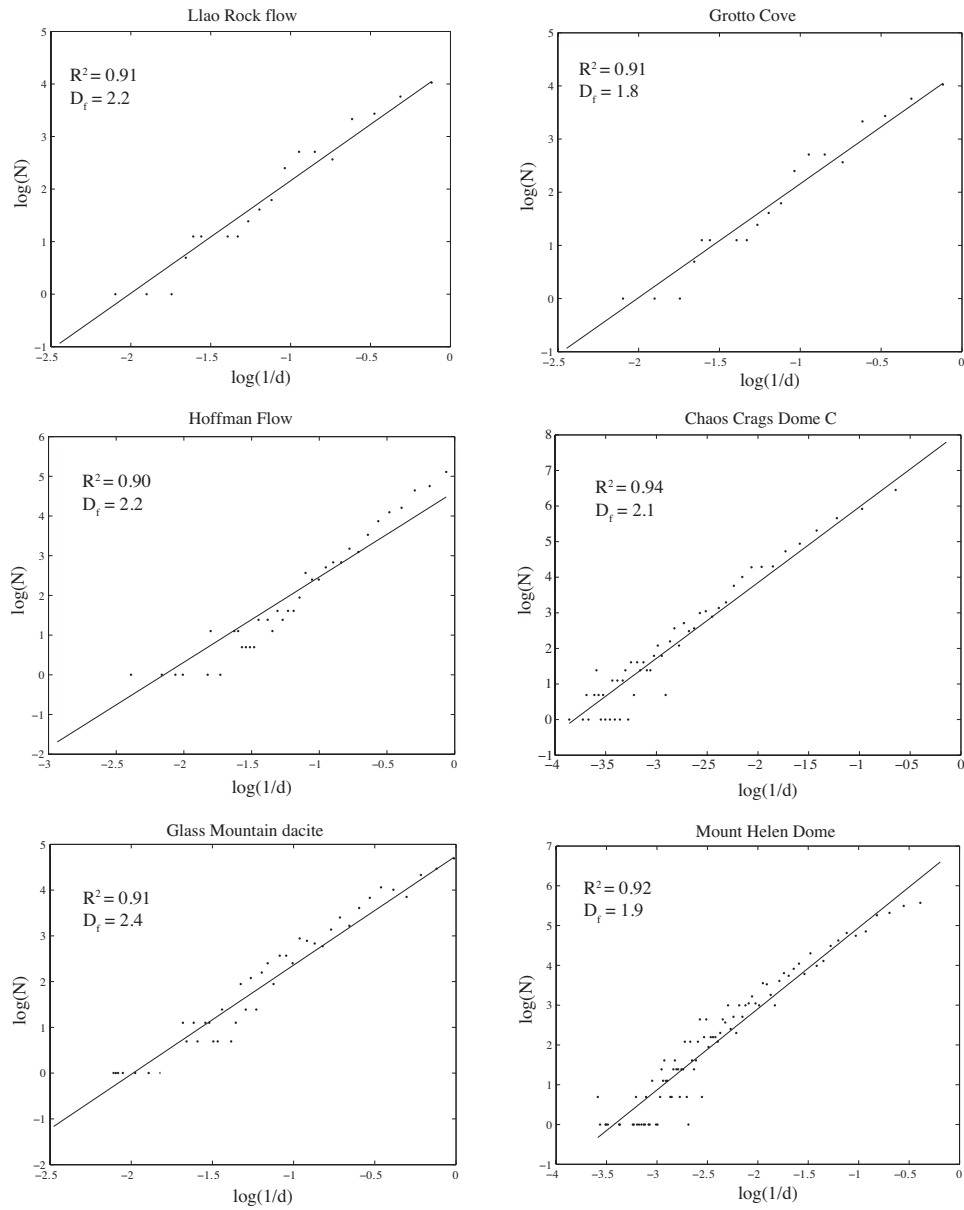


Figure 4.6: $\log(1/r)$ vs. $\log(N)$ plots used to determine the fractal dimension (D_f) for enclaves in each lava flow.

4.5. Results and Discussion

characteristic diameter $d_b \approx d_m$ given by:

$$\frac{d_m}{d_i} = 0.001 \frac{\mu_h V_c}{\tau_y d_i}, \quad (4.7)$$

where μ_h is the host viscosity, V_c is the ambient chamber velocity, d_i is the initial dike width, and τ_y is the yield strength of the intruding material.

Assuming enclave production occurs in the tension regime and that the injection dike widths and host magma viscosity can be inferred from field and petrologic constraints, Equation 4.7 implies that $d_m/d_i \propto V_c/\tau_y$, and that (V_c/τ_y) cannot vary such that $Y > 40$ (to remain in the Tension regime). For a given yield strength τ_y , this constraint limits the possible range in chamber flow velocities V_c (or vice versa). A popular way to estimate the yield strength of magmas related to a touching framework of crystals is through Equation 4.6. Using upper and lower bounds for the solid fraction in the enclave magma discussed in Section 4.3.4, we obtain $\sim 0.3 < \tau_y < 300$ Pa for all data (Table 4.2), which restricts $V_c \geq 10^{-2}$ m s⁻¹. Using these values, we plot a Y-S parameter space for enclave formation in each of the six lava flows in Figure 4.5.

Location	μ_h (Pa s)	μ_e (Pa s)	τ_y (Pa) ¹	τ_y (Pa) ²	S	Y	d_m (cm)	D_f
Llao Rock	4×10^4	$5 \times 10^{2-3}$	0.3-300	35	5×10^{-5}	12	1	2.2
Grotto Cove	3×10^3	$5 \times 10^{3-4}$	0.3-160	1	6×10^{-3}	2	3	2
Glass Mountain	1×10^4	$5 \times 10^{2-4}$	0.3-100	15	5×10^{-5}	7	1	2.2
Hoffman Flow	3×10^5	$2 \times 10^{2-6}$	0.3-350	300	7×10^{-6}	30	1	2.2
Chaos Crags	2×10^4	$4 \times 10^{3-4}$	0.3-350	10	1×10^{-3}	5	2.5	2
Mount Helen	2×10^5	$1 - 2 \times 10^4$	0.3-250	70	2×10^{-4}	20	2.2	2

Table 4.2: Calculated properties of six lava flows using data reported in Table 4.1, median enclave size d_m , and fractal dimension D_f for each lava flow. We estimate magma effective viscosity using the Giordano et al. [2008] model to calculate melt viscosity together and the effective viscosity relationship (see Equation 4.4) from Scott and Kohlstedt [2006], which accounts for the solid fraction in the melt. We calibrate the Scott and Kohlstedt fit to capture the effective viscosity for both low (0 – 40%) and high (> 40%) crystal fractions (see HCJ12a for a more complete discussion). μ_h is host effective viscosity and μ_e is enclave effective viscosity. We use two methods to calculate the enclave magma’s yield strength: (1) the phenocryst content (Table 4.1) with results from Hoover et al. [2001] (see Equation 4.6), and (2) the scaling law from Hodge et al. [2012a] (see Equation 4.7) which utilizes the breakup length scale d_m that we measure in the field. We use a range in chamber heights $h = 100 - 1000$ m and we take the initial dike width $d_i = 1$ m. (1) [Hoover et al., 2001], (2) [Hodge et al., 2012a]

We can further refine the yield strength of the enclave magma, and thus the Y – S regime for each lava flow using d_m from the data analysis. If we apply this value as a unique constraint and the order of magnitude estimate for $V_c \sim 10^{-2} \text{ m s}^{-1}$ as a lower bound to Equation 4.7 we obtain the Y-S values shown as star-symbols (Figure 4.5). We note that in all six cases, these points plot within the Y-S ranges determined using the scaling for τ_y from Equation 4.6.

In Figure 4.5, the variation in the Y values calculated from the data analysis in Figure 4.3 is related to variations in the median enclave diameter d_m in the data for each lava flow. Variations in the S parameter arise mostly from the range in chamber height ($h = 100 - 1000 \text{ m}$) that we prescribe (Table 4.2), but also from viscosity variations between the host and enclave magmas (Equation 4.3 and Table 4.2). For a given h and d_i , we can explore variations in S caused only by viscosity contrast between the host and enclave magmas and classify the lava flows into two groups: low-S (Llao Rock, Glass Mountain, and the Hoffman Flow) and high-S (Grotto Cove, Chaos Crag, and Mount Helen). The high-S group (hereafter: *Group HS*) has S-values between 10^{-1} and 10^{-4} and d_m between 2 and 3 cm . The low-S group (hereafter: *Group LS*) has S-values between 10^{-4} and 10^{-6} and d_m values $\sim 1 \text{ cm}$ (Figure 4.7a). Since the variation in S is a function of the viscosity ratio between injected and host magma, we note that *Group HS* corresponds to a low viscosity contrast and *Group LS* corresponds to a high viscosity contrast.

4.5.2 The character of enclave fragmentation

A fractal dimension D_f for our enclave distributions characterizes the extent to which an injection at the large scale of a dike width ultimately breaks up over the range of scale lengths we observe in the field. The power law behavior in Figure 4.6 implies that the same physical process acts at all scales. A visual example of such a continuous process of fragmentation of a rheologically complex plume in a shear flow is shown in the time-series in Figure 4.4b. In this case, the majority of the evolution of the stretching

and breakup of the analog dike is governed largely by a balance between the viscous stress related to imposed shearing and the retarding yield strength of the buoyant mixture. All lava flows in this study show similar fractal dimensions that are consistent with previous studies [Perugini and Poli, 2000; Holtz et al., 2004; Ventura et al., 2006; Perugini et al., 2007].

Although the range in D_f is similar for all lava flows (Figure 4.6), indicating comparable evolutions and extents of fragmentation from the largest to the smallest enclave sizes [Turcotte, 1986], the mean fractal dimensions for the LS and HS groups are distinct, which suggests that viscosity variations between the enclave and host magmas influence the breakup size, and consequently the extent of fragmentation (Figure 4.7a and b). Additionally, our data confirm a relationship between median enclave size d_m and fractal dimension D_f (Figure 4.7c), such that *Group LS* and *HS* lava flows form two clusters that have high D_f and low d_m values, and low D_f and high d_m values, respectively. This result implies that large viscosity contrasts between the host and enclave magmas enhance the efficiency of fragmentation.

One common speculation for the variability of enclave sizes in, for example, the Chaos Crags Dome C is that original blobs of magma that form as a result of stirring motions in the chamber (largest enclaves) will undergo further deformation and breakup during ascent through the conduit (M. Clynne, personal communication). An interesting outcome of this study is that D_f is more or less similar in all flows, even though enclaves originally produced in the chamber may be subjected to further deformation during eruption. This result suggests that the same physics govern deformation and fragmentation from the chamber through the conduit. A crucial difference, of course, is that assuming the flow velocities in the chamber and conduit are close in an order of magnitude sense, the predominant strain rate giving rise to the viscous stress deforming enclaves $V_c/d \gg V_c/h$, where d is the conduit diameter. Thus, a greater extent of fragmentation in the conduit may occur for enclave magmas with a given yield strength.

4.5. Results and Discussion

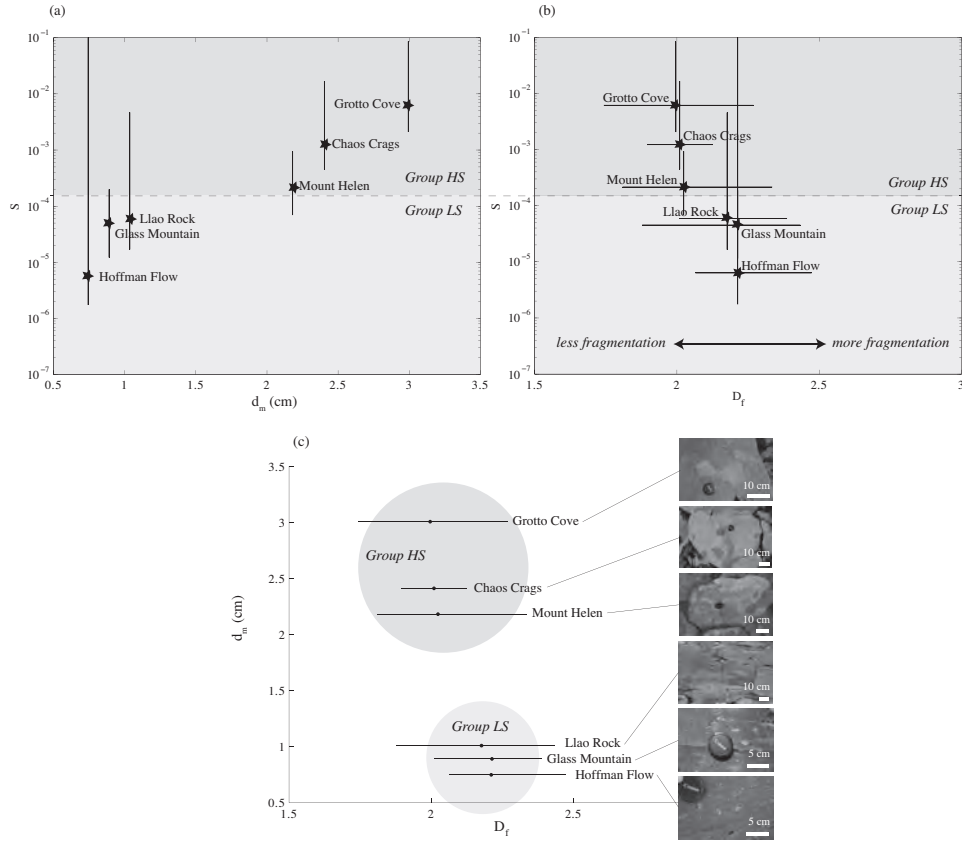


Figure 4.7: Plot of (a) median enclave size d_m ; and (b) fractal dimension D_f vs. the S parameter for each lava flow. Dashed line shows division between *Group HS* (top) and *Group LS* (bottom). (c) Plot of fractal dimension vs. median enclave size d_m for each lava flow. Photo insets show enclaves at each location. Shaded circles denote *Group HS* and *Group LS*.

4.6 Conclusions

We analyze an extensive dataset of enclave size distributions using results and scaling theory from HCJ12 to demonstrate that field observations of enclave sizes can reliably constrain aspects of the rheological and flow conditions that govern the deformation and breakup of dikes of relatively more mafic magma injected into a silicic magma chamber. Our data analysis understood with experiments and scaling theory is consistent with millimeter to centimeter-scale enclaves forming in a regime in which meter-scale dikes with a yield strength disaggregate as the result of viscous stresses related to magma chamber flow. Our results also identify a corresponding characteristic breakup length scale d_m that constrains the yield strength of the injected magma more reliably than existing empirical models for yield strength that are based on crystal content. From fractal analysis, the evolution of breakup from the initial injection size (dike width) to the mm-cm scale enclaves is self similar. The extent of breakup in all 6 domes is roughly similar with a fractal dimension $D_f \sim 2$. However, the fractal dimension has a small but statistically significant dependence on effective viscosity ratio consistent with greater extents of fragmentation occurring where viscosity contrasts are large.

This study provides a method to use field data of enclave size distributions to back out key physical properties of the host and enclave magmas and to constrain chamber flow conditions at the time of enclave formation. Our work assumes enclave production occurs in the tension regime where, for example, a 1 m-wide dikes will breakup into mm to cm size enclaves, which sets limits on the ratio between V_c and τ_y such that $Y > 40$. Therefore, an important direction for future work is finding a way to independently constrain chamber stirring velocities V_c . Additionally, because we sample six lava flows in the Cascades, another obvious direction for future work would be to expand this dataset to include other lava flows that host enclaves in an attempt to map a wider range in viscosity variations.

Chapter 5

Conclusion

In this thesis my aim was to build understanding of how silicic magma chamber grow, differentiate, and ultimately erupt. More specifically, I was interested in what controls the extent to which a new injection of magma will disaggregate and breakup or remain intact and form continuous layers upon injection into a magma chamber. The main goal was to develop a method to utilize field observations of magmatic structures observed in volcanic and plutonic rocks (e.g. mafic enclaves and ladder dikes) as a tool to constrain aspects of the styles of flow, stirring, and mixing within a magma chamber, as well as the rheological contrast between two mixing magmas. In this section, I provide a summary of the main findings from each of the three research chapters and discuss possible directions for future work.

5.1 Summary

Chapter 2 presents laboratory experiments and scaling theory used to investigate the mechanical and rheological conditions leading to the deformation and breakup of analog crystal-rich dikes injected as discrete plumes that descend into an underlying shear flow. In this chapter, I show that depending on the rheology of the host and injected material as well as the ambient flow conditions, a rheologically complex dike will breakup in one of two regimes: (*i*) the Rayleigh-Taylor regime in which $Y > Y_c$ and the breakup length scale is similar to the injection width; or (*ii*) the Tension regime in which $Y < Y_c$ and the breakup length scale is much smaller than the injection width. In the Ponding regime above a certain particle volume fraction, an injected plume will behave as a solid over the timescale of stirring in the tank. The scaling results for the breakup size in both the Rayleigh-Taylor and Tension

regimes place restrictions on the length scales of deformation that can occur during magma mixing. Furthermore, in the case of a 1 meter wide dike entering a silicic magma chamber, the resulting enclave sizes (millimeters to centimeters) will be much smaller than the initial dike width. The major result of this study is that enclave size distributions can be used to infer aspects of the style of stirring and rheology of the host magma at the time of enclave formation.

Chapter 3 and 4 were aimed to test the results of Chapter 2. Chapter 3 presents a new comprehensive field study of ladder dikes in the Tuolumne Intrusive Suite. This field study, understood with experiments and scaling theory, shows that ladder dikes represent broken segments of previously long (> 25 m), buoyant, and rheologically complex plumes that rose or fell while being deformed by shearing motions in the magma chamber. In this chapter, I describe the new quantitative mechanical framework that this study places on the formation and deformation of ladder dikes. The model captures both the large scale breakup patterns as well as the mafic-felsic banding—features that have, until now, only been described conceptually in previous studies.

Chapter 4 presents an extensive field investigation of enclave formation in lava flows. Applying again the results described in Chapter 2, I link field data of enclave size distributions to aspects of the rheological and flow conditions within the chamber necessary for enclave formation. I identify the characteristic breakup length scale in each lava flow that I use to constrain the yield strength of the enclave-forming magma more reliably than other empirical models that use crystal content to calculate yield strength. I use fractal analysis to show that the breakup of a 1 m wide dike into millimeter to centimeter size enclaves is self similar and the corresponding fractal dimension has a small but statistically significant dependence on the effective viscosity ratio between host and enclave magmas.

5.2 Future work

The length scales of thermal and compositional heterogeneity introduced by the breakup of new inputs of mafic or silicic magma will control how

a magma chamber evolves both thermally and compositionally and possibly how and when it will erupt. For example, if a new intrusion of hot mafic magma is broken up into small blobs, heat will be transferred more efficiently to the host magma than it would from a continuous mafic layer. Therefore, understanding the link between the breakup and deformation of a new injection of hot mafic magma and the mobilization (or remobilization) of a viscous crystal-rich batch of eruptible silicic magma may place constraints on what volcanologists should monitor at active volcanos—for example, changes in heat flow that may signal the input and subsequent breakup of a hot, mantle-derived mafic magma (e.g., Yellowstone Volcano; Lowenstern et al. [2006]) [Bachmann and Bergantz, 2004; Huber et al., 2012].

A major result discussed in Chapter 2 is that the breakup scale sets the scale for thermal and compositional interactions between the new injection and the host magma. New magma inputs that disaggregate in the breakup regime introduce heterogeneity at scale lengths that are small in comparison to the initial dike width. The increased surface area over which the new mafic and host silicic magma are coupled thermally and chemically through this mechanism should lead to enhanced thermal and chemical exchange between the two magmas. In the limit that these new magma blobs have a viscous response to stirring motions in the magma chamber, it is possible that the rate and efficiency at which this material is incorporated into the host magma will increase greatly over current estimates [Blake and Campbell, 1986; Turner and Campbell, 1986; Snyder and Tait, 1996b; Jellinek and Kerr, 1999; Perugini et al., 2002]. In Chapter 2, I mention that the absence of mafic layering in some chambers may come as a result of a decrease in the viscosity of the input mafic magma (perhaps from the addition of water or from a higher injection temperature) and as a result, the injection will be more likely to break up and form enclaves. One interesting direction for future work is to look at the mixing properties and compositional differentiation of magma chambers for this case, which would suggest that the breakup to short length scales can explain why silicic plutons that do not preserve mafic layers are so homogenous. Moreover, the spectrum of scales of thermal and compositional heterogeneity that result from the breakup of

5.2. Future work

a new injection will govern how efficiently magma chambers heat up and also how they evolve chemically as a result of mechanical mixing.

There are a number of unanswered questions from my work presented in Chapter 3 on ladder dikes. One of the many noteworthy features of ladder dikes are the huge K-feldspar megacrysts that are present not only within the ladder dike margins but also throughout the Cathedral Peak Granodiorite. Understanding the spatial distribution of these megacrysts may provide more information on the flow history of the ladder dikes during deformation. The spatial clustering of ladder dikes remains an enigma—why are they not everywhere? One goal for a future investigation would be to understand why they are located so close to contacts (specifically where they are clustered) with other intrusive units and what their nearly perpendicular orientation to these contacts tells us about their formation and deformation history.

In Chapter 4, I conclude that because enclaves are produced in the Tension regime, the presence of millimeter-centimeter size enclaves puts constraints on the initial dike width ($\sim 1 - 10$ m) and the ratio between the chamber stirring velocity and the injected magma's yield strength so that the Y parameter in our regime diagram is less than 40. An independent constraint on the chamber stirring velocity would further restrict the yield strength necessary for breakup. Because the data presented in Chapter 4 comprise six lava flows from the Cascades, it would be useful to look at other enclaves and host compositions to fill out a wider range in viscosity variations on my regime diagram.

Bibliography

- J. Abbott, Richard N. Internal structures in part of the South Mountain batholith, Nova Scotia, Canada. *Geological Society of America Bulletin*, 101(11):1493–1506, 1989.
- C. Akal and C. Helvaci. Mafic microgranular enclaves in the Kozak granodiorite, Western Anatolia. *Tr. J. of Earth Sciences*, 8:1–17, 1999.
- A. Alves, V. de Assis Janasi, A. Simonetti, and L. Heaman. Microgranitic enclaves as products of self-mixing events: a study of open-system processes in the Mau granite, So Paulo, Brazil, Based on in situ Isotopic and Trace Elements in Plagioclase. *Journal of Petrology*, 50(12):2221–2247, 2009.
- C. Archanjo, J.-L. Bouchez, M. Corsini, and A. Vauchez. The Pombal granite pluton: Magnetic fabric, emplacement and relationships with the Brasiliano strike-slip setting of NE Brazil (Paraíba State). *Journal of Structural Geology*, 16(3):323 – 335, 1994.
- P. D. Asimow and M. S. Ghiorso. Algorithmic modications extending MELTS to calculate subsolidus phase relations. *American Mineralogist*, 83:1127–1132, 1998.
- C. A. Bachl, C. F. Miller, J. S. Miller, and J. E. Faulds. Construction of a pluton: Evidence from an exposed cross section of the Searchlight pluton, Eldorado Mountains, Nevada. *Geological Society of America Bulletin*, 113(9):1213–1228, 2001.
- O. Bachmann and G. W. Bergantz. On the origin of crystal-poor rhyolites:

Bibliography

- Extracted from batholithic crystal mushes. *Journal of Petrology*, 45(8): 1565–1582, 2004.
- C. R. Bacon. Magmatic inclusions in silicic and intermediate volcanic rocks. *J. Geophys. Res.*, 91(B6):6091–6112, 1986.
- C. R. Bacon and T. H. Druitt. Compositional evolution of the zoned calcaline magma chamber of Mount Mazama, Crater Lake, Oregon. *Contributions to Mineralogy and Petrology*, 98:224–256, 1988.
- C. R. Bacon and M. A. Lanphere. Eruptive history and geochronology of Mount Mazama and the Crater Lake region, Oregon. *Geological Society of America Bulletin*, 118(11-12):1331–1359, 2006.
- C. R. Bacon and J. Metz. Magmatic inclusions in rhyolites, contaminated basalts, and compositional zonation beneath the Coso volcanic field, California. *Contributions to Mineralogy and Petrology*, 85:346–365, 1984.
- R. A. Bagnold. Experiments on a Gravity-Free Dispersion of Large Solid Spheres in a Newtonian Fluid under Shear. *Proceedings of the Royal Society of London. Series A, Mathematical and Physical Sciences*, 225 (1160):49–63, 1954.
- R. A. Balley. Eruptive history and chemical evolution of the precaldera and postcaldera basalt-dacite sequences, Long Valley, California: implications for magma sources, current magmatic unrest, and future volcanism. *U.S. Geol. Surv. Prof. Paper 1692*, 2004.
- R. Balk. *Structural behavior of igneous rocks*. New York: Springer, 1937.
- B. Barbarin. Mafic magmatic enclaves and mafic rocks associated with some granitoids of the central Sierra Nevada batholith, California: nature, origin, and relations with the hosts. *Lithos*, 80(1-4):155 – 177, 2005.
- P. Barbey, D. Gasquet, C. Pin, and A. Bourgeix. Igneous banding, schlieren and mafic enclaves in calc-alkaline granites: The Budduso pluton, Sardinia. *Lithos*, 104(1-4):147 – 163, 2008.

Bibliography

- M. Barrière. On curved laminae, graded layers, convection currents and dynamic crystal sorting in the Ploumanac'h (Brittany) subalkaline granite. *Contributions to Mineralogy and Petrology*, 77:214–224, Oct. 1981.
- P. C. Bateman. Plutonism in the central part of Sierra Nevada Batholith, California. *U.S. Geological Survey Professional Paper*, 1483:186, 1992.
- P. C. Bateman and B. W. Chappell. Crystallization, fractionation, and solidification of the Tuolumne Intrusive Series, Yosemite National Park, California. *Geological Society of America Bulletin*, 90(5):465–482, 1979.
- M. Belzons, R. Blanc, J. L. Bouillot, and C. Camoin. Viscosité d'une suspension diluée et bidimensionnelle de sphères. *CR Acad. Sci., Paris*, 292(13):939–944, 1981.
- I. N. Bindeman and J. W. Valley. Formation of low- $\Delta^{18}\text{O}$ rhyolites after caldera collapse at Yellowstone, Wyoming, USA. *Geology*, 28(8):719–722, 2000.
- S. Blake and I. H. Campbell. The dynamics of magma-mixing during flow in volcanic conduits. *Contributions to Mineralogy and Petrology*, 94:72–81, 1986.
- J. D. Blundy and R. S. J. Sparks. Petrogenesis of mafic inclusions in granitoids of the Adamello Massif, Italy. *Journal of Petrology*, 33(5):1039–1104, 1992.
- Y. Bottinga and D. F. Weill. The viscosity of magmatic silicate liquids; a model calculation. *Am J Sci*, 272(5):438–475, 1972.
- J. F. Brady and G. Bossis. The rheology of concentrated suspensions of spheres in simple shear flow by numerical simulation. *Journal of Fluid Mechanics Digital Archive*, 155(-1):105–129, 1985.
- I. H. Campbell and J. S. Turner. The influence of viscosity on fountains in magma chambers. *Journal of Petrology*, 27(1):1–30, 1986.

Bibliography

- L. Caricchi, L. Burlini, P. Ulmer, T. Gerya, M. Vassalli, and P. Papale. Non-Newtonian rheology of crystal-bearing magmas and implications for magma ascent dynamics. *Earth and Planetary Science Letters*, 264(3-4): 402 – 419, 2007.
- R. G. Cawthorn and F. Walraven. Emplacement and crystallization time for the Bushveld Complex. *Journal of Petrology*, 39(9):1669–1687, 1998.
- S. Chandrasekhar. *Hydrodynamic and hydromagnetic stability*. Oxford University Press, 1961.
- R. L. Christiansen. Yellowstone magmatic evolution: its bearing on understanding large-volume explosive volcanism. In: *Explosive Volcanism: Inception, Evolution, and Hazards*. Washington, DC National Academy Press, pages 84–95, 1984.
- M. A. Clyne. A complex magma mixing origin for rocks erupted in 1915, Lassen Peak, California. *Journal of Petrology*, 40(1):105–132, 1999.
- D. S. Coleman, A. F. Glazner, J. S. Miller, K. J. Bradford, T. P. Frost, J. L. Joye, and C. A. Bachl. Exposure of a late cretaceous layered mafic-felsic magma system in the central Sierra Nevada batholith, California. *Contributions to Mineralogy and Petrology*, 120:129–136, 1995.
- J. Deubener, R. Mller, H. Behrens, and G. Heide. Water and the glass transition temperature of silicate melts. *Journal of Non-Crystalline Solids*, 330(1-3):268 – 273, 2003.
- G. Di Vincenzo and S. Rocchi. Origin and interaction of mafic and felsic magmas in an evolving late orogenic setting: the Early Paleozoic Terra Nova Intrusive Complex, Antarctica. *Contributions to Mineralogy and Petrology*, 137:15–35, 1999.
- J. Didier. Contribution of enclave studies to the understanding of origin and evolution of granitic magmas. *Geologische Rundschau*, 76:41–50, 1987. ISSN 0016-7835.

Bibliography

- J. Didier and B. Barbarin. *Enclaves and granite petrology, developments in petrology*. Elsevier Science Ltd, 1991.
- D. B. Dingwell. Viscosity and anelasticity of melts and glasses. *Mineral physics and crystallography. A handbook of physical constants*, 2:209 – 217, 1995.
- J. E. Dixon and D. A. Clague. Volatiles in basaltic glasses from Loihi Seamount, Hawaii: evidence for a relatively dry plume component. *Journal of Petrology*, 42(3):627–654, 2001.
- F. D. W. Dodge and R. W. Kistler. Some additional observations on inclusions in the granitic rocks of the Sierra Nevada. *Journal of Geophysical Research*, 95:17841–17848, Oct. 1990.
- T. Donaire, E. Pascual, C. Pin, and J.-L. Duthou. Microgranular enclaves as evidence of rapid cooling in granitoid rocks: the case of the Los Pedroches granodiorite, Iberian Massif, Spain. *Contributions to Mineralogy and Petrology*, 149:247–265, 2005.
- J. M. Donnelly-Nolan, T. L. Grove, M. A. Lanphere, D. E. Champion, and D. W. Ramsey. Eruptive history and tectonic setting of Medicine Lake Volcano, a large rear-arc volcano in the southern Cascades. *Journal of Volcanology and Geothermal Research*, 177:313–328, 2008.
- J. C. Eichelberger. Origin of andesite and dacite: Evidence of mixing at Glass Mountain in California and at other circum-Pacific volcanoes. *Geological Society of America Bulletin*, 86(10):1381–1391, 1975.
- J. C. Eichelberger. Vesiculation of mafic magma during replenishment of silicic magma reservoirs. *Nature*, 288(5790):446–450, 12 1980.
- A. Einstein. Eine neue Bestimmung der Molekuldimensionen. *Annalen der Physik*, 324(2):289–306, 1906.
- M. A. Elburg. U-Pb ages and morphologies of zircon in microgranitoid enclaves and peraluminous host granite: evidence for magma mingling. *Contributions to Mineralogy and Petrology*, 123:177–189, 1996.

Bibliography

- R. W. D. Elwell, R. R. Skelhorn, and A. R. Drysdall. Inclined granitic pipes in the diorites of Guernsey. *Geological Magazine*, 97(2):89–105, 1960.
- R. W. D. Elwell, R. R. Skelhorn, and A. R. Drysdall. Net-veining in the diorite of Northeast Guernsey, Channel Islands. *The Journal of Geology*, 70(2):pp. 215–226, 1962.
- T. Feeley, L. Wilson, and S. Underwood. Distribution and compositions of magmatic inclusions in the Mount Helen dome, Lassen Volcanic Center, California: Insights into magma chamber processes. *Lithos*, 106(1-2):173 – 189, 2008.
- F. Folgar and I. Tucker, Charles L. Orientation behavior of fibers in concentrated suspensions. *Journal of Reinforced Plastics and Composites*, 3(2):98–119, 1984.
- M. Franceschelli, M. Puxeddu, G. Cruciani, A. Dini, and M. Loi. Layered amphibolite sequence in NE Sardinia, Italy: remnant of a pre-Variscan mafic silicic layered intrusion? *Contributions to Mineralogy and Petrology*, 149:164–180, 2005.
- T. P. Frost and G. A. Mahood. Field, chemical, and physical constraints on mafic-felsic magma interaction in the Lamarck granodiorite, Sierra Nevada, California. *Geological Society of America Bulletin*, 99(2):272–291, 1987.
- F. Gadala-Maria and A. Acrivos. Shear-induced structure in a concentrated suspension of solid spheres. *Journal of Rheology*, 24(6):799–814, 1980.
- N. Gay. Orientation of mineral lineation along the flow direction in rocks: A discussion. *Tectonophysics*, 3:559–562, Dec. 1966.
- M. S. Ghiorso and R. O. Sack. Chemical mass transfer in magmatic processes IV. A revised and internally consistent thermodynamic model for the interpolation and extrapolation of liquid-solid equilibria in magmatic systems at elevated temperatures and pressures. *Contributions to Mineralogy and Petrology*, 119:197–212, 1995.

Bibliography

- D. Giordano and D. B. Dingwell. Non-Arrhenian multicomponent melt viscosity: A model. *Earth and Planetary Science Letters*, 208(3-4):337 – 349, 2003.
- D. Giordano, J. K. Russell, and D. B. Dingwell. Viscosity of magmatic liquids: A model. *Earth and Planetary Science Letters*, 271(1-4):123 – 134, 2008.
- H. M. Gonnermann and M. Manga. Flow banding in obsidian: A record of evolving textural heterogeneity during magma deformation. *Earth and Planetary Science Letters*, 236(1-2):135 – 147, 2005.
- H. M. Gonnermann and M. Manga. The Fluid Mechanics Inside a Volcano. *Annual Review of Fluid Mechanics*, 39:321–356, Jan. 2007.
- T. L. Grove and J. M. Donnelly-Nolan. The evolution of young silicic lavas at Medicine Lake Volcano, California: Implications for the origin of compositional gaps in calc-alkaline series lavas. *Contributions to Mineralogy and Petrology*, 92:281–302, 1986.
- T. L. Grove, J. M. Donnelly-Nolan, and T. Housh. Magmatic processes that generated the rhyolite of Glass Mountain, Medicine Lake volcano, N. California. *Contributions to Mineralogy and Petrology*, 127:205–223, 1997.
- G. A. R. Gualda, M. S. Ghiorso, R. V. Lemons, and T. L. Carley. Rhyolite-MELTS: a modified calibration of MELTS optimized for silica-rich, fluid-bearing magmatic systems. *Journal of Petrology*, 2012.
- A. N. Halliday, G. A. Mahood, P. Holden, J. M. Metz, T. J. Dempster, and J. P. Davidson. Evidence for long residence times of rhyolitic magma in the Long Valley magmatic system: the isotopic record in precaldera lavas of Glass Mountain. *Earth and Planetary Science Letters*, 94:274–290, 1989.
- J. Happel. Viscosity of Suspensions of Uniform Spheres. *Journal of Applied Physics*, 28:1288–1292, 1957.

Bibliography

- B. E. Harper, C. F. Miller, G. C. Koteas, N. L. Gates, R. A. Wiebe, D. S. Lazzareschi, and J. W. Cribb. Granites, dynamic magma chamber processes and pluton construction: the Aztec Wash pluton, Eldorado Mountains, Nevada, USA. *Geological Society of America Special Papers*, 389: 277–295, 2004.
- G. Heiken and J. C. Eichelberger. Eruptions at Chaos Crags, Lassen Volcanic National Park, California. *Journal of Volcanology and Geothermal Research*, 7(3-4):443 – 481, 1980.
- K. U. Hess, D. B. Dingwell, C. Gennaro, and V. Mincione. Viscosity-temperature behaviour of dry melts in the qz-ab-or system. *Chemical Geology*, 174(1-3):133 – 142, 2001.
- W. Hildreth. Volcanological perspectives on Long Valley, Mammoth Mountain, and Mono Craters: several contiguous but discrete systems. *Journal of Volcanology and Geothermal Research*, 136(3-4):169 – 198, 2004.
- W. Hildreth, A. N. Halliday, and R. L. Christiansen. Isotopic and Chemical Evidence Concerning the Genesis and Contamination of Basaltic and Rhyolitic Magma Beneath the Yellowstone Plateau Volcanic Field. *J. Petrology*, 32(1):63–138, 1991.
- K. F. Hodge, G. Carazzo, and A. M. Jellinek. Experimental constraints on the deformation and breakup of injected magma. *Earth and Planetary Science Letters*, 325-326:52 – 62, 2012a.
- K. F. Hodge, G. Carazzo, X. Montague, and A. Jellinek. Magmatic structures in the Tuolumne Intrusive Suite, California: a new model for the formation and deformation of ladder dikes. *Contributions to Mineralogy and Petrology*, pages 1–14, 2012b.
- F. Holtz, S. Lenné, G. Ventura, F. Vetere, and P. Wolf. Non-linear deformation and break up of enclaves in a rhyolitic magma: A case study from Lipari Island (southern Italy). *Geophysical Research Letters*, 31:24611, 2004.

Bibliography

- S. R. Hoover, K. V. Cashman, and M. Manga. The yield strength of subliquidus basalts – experimental results. *Journal of Volcanology and Geothermal Research*, 107(1-3):1–18, 2001.
- N. Huang and D. Bonn. Viscosity of a dense suspension in couette flow. *Journal of Fluid Mechanics*, 590:497–507, 2007.
- N. Huang, G. Ovarlez, F. Bertrand, S. Rodts, P. Coussot, and D. Bonn. Flow of wet granular materials. *Phys. Rev. Lett.*, 94(2):028301, 2005.
- C. Huber, O. Bachmann, and J. Dufek. Crystal-poor versus crystal-rich ignimbrites: A competition between stirring and reactivation. *Geology*, 40(2):115–118, 2012.
- D. H. W. Hutton. Granite emplacement mechanisms and tectonic controls: Inferences from deformation studies. *Royal Society of Edinburgh Transactions*, 79:245–255, 1988.
- T. Irvine. Terminology for layered intrusions. *Journal of Petrology*, 23(2):127–162, 1982.
- G. B. Jeffery. The motion of ellipsoidal particles immersed in a viscous fluid. *Royal Society of London Proceedings Series A*, 102:161–179, 1922.
- D. J. Jeffrey and A. Acrivos. The rheological properties of suspensions of rigid particles. *AIChE Journal*, 22:417–432, 1976.
- A. M. Jellinek and D. J. DePaolo. A model for the origin of large silicic magma chambers: precursors of caldera-forming eruptions. *Bulletin of Volcanology*, 65(5):402 – 419, 2003.
- A. M. Jellinek and R. C. Kerr. Mixing and compositional stratification produced by natural convection: 2. Applications to the differentiation of basaltic and silicic magma chambers and komatiite lava flows. *J. Geophys. Res.*, 104(B4):7203–7218, 1999.
- A. M. Jellinek, R. C. Kerr, and R. W. Griffiths. Mixing and compositional stratification produced by natural convection: 1. Experiments and their

Bibliography

- application to Earth's core and mantle. *J. Geophys. Res.*, 104(B4):7183–7201, 1999.
- Z. Jurado-Chichay and G. P. L. Walker. The intensity and magnitude of the Mangaone subgroup plinian eruptions from Okataina Volcanic Centre, New Zealand. *Journal of Volcanology and Geothermal Research*, 111(1-4): 219 – 237, 2001.
- S. Keay, W. J. Collins, and M. T. McCulloch. A three-component Sr-Nd isotopic mixing model for granitoid genesis, Lachlan fold belt, eastern Australia. *Geology*, 25(4):307–310, 1997.
- K. A. Kelley and E. Cottrell. Water and the Oxidation State of Subduction Zone Magmas. *Science*, 325(5940):605–607, 2009.
- B. M. Kennedy, M. A. Jellinek, and J. Stix. Coupled caldera subsidence and stirring inferred from analogue models. *Nature Geoscience*, 1(6):385–389, 2008.
- J. Kim, K. Shin, and J. Lee. Petrographical study on the Yucheon granite and its enclaves. *Geosciences Journal*, 6:289–302, 2002. ISSN 1226-4806.
- R. J. Kinzler, J. M. Donnelly-Nolan, and T. L. Grove. Late Holocene hydrous mafic magmatism at the Paint Pot Crater and Callahan flows, Medicine Lake Volcano, N. California and the influence of H₂O in the generation of silicic magmas. *Contributions to Mineralogy and Petrology*, 138:1–16, 2000.
- T. Koyaguchi. Magma mixing in a conduit. *Journal of Volcanology and Geothermal Research*, 25(3-4):365 – 369, 1985.
- I. M. Krieger and T. J. Dougherty. A mechanism for Non-Newtonian flow in suspensions of rigid spheres. *Journal of Rheology*, 3(1):137–152, 1959.
- S. Kumar. Mafic to hybrid microgranular enclaves in the Ladakh batholith, northwest Himalaya: Implications on calc-alkaline magma chamber processes. *Journal of the Geological Society of India*, 76:5–25, 2010. ISSN 0016-7622.

Bibliography

- L. L. Larsen and E. I. Smith. Mafic enclaves in the Wilson Ridge pluton, northwestern Arizona: implications for the generation of a calc-alkaline intermediate pluton in an extensional environment. *J. Geophys. Res.*, 95 (B11):17693–17716, 1990.
- G. L. Leal. *Laminar flow and convective transport processes : scaling principles and asymptotic analysis*. Butterworth-Heinemann, 1992.
- D. Leighton and A. Acrivos. The shear-induced migration of particles in concentrated suspensions. *Journal of Fluid Mechanics Digital Archive*, 181(-1):415–439, 1987.
- A. M. Lejeune and P. Richet. Rheology of crystal-bearing silicate melts: An experimental study at high viscosities. *J. Geophys. Res.*, 100, 1995.
- A. M. Lejeune, Y. Bottinga, T. W. Trull, and P. Richet. Rheology of bubble-bearing magmas. *Earth and Planetary Science Letters*, 166:71–84, 1999.
- G. S. Leonard, J. W. Cole, I. A. Nairn, and S. Self. Basalt triggering of the c. AD 1305 Kaharoa rhyolite eruption, Tarawera Volcanic Complex, New Zealand. *Journal of Volcanology and Geothermal Research*, 115(3-4):461 – 486, 2002.
- J. R. Lister and R. C. Kerr. Fluid-mechanical models of crack propagation and their application to magma transport in dykes. *J. Geophys. Res.*, 96 (B6):10049–10077, 1991.
- E. Llewellyn and M. Manga. Bubble suspension rheology and implications for conduit flow. *Journal of Volcanology and Geothermal Research*, 143 (1-3):205 – 217, 2005.
- J. B. Lowenstern, R. B. Smith, and D. P. Hill. Monitoring super-volcanoes: geophysical and geochemical signals at Yellowstone and other large caldera systems. *Philosophical Transactions of the Royal Society A: Mathematical, Physical and Engineering Sciences*, 364(1845):2055–2072, 2006.
- B. B. Mandelbrot. *The fractal geometry of nature*. W. H. Freeman, 1982.

Bibliography

- M. Manga. Orientation distribution of microlites in obsidian. *Journal of Volcanology and Geothermal Research*, 86(1-4):107 – 115, 1998.
- M. Manga, J. Castro, K. V. Cashman, and M. Loewenberg. Rheology of bubble-bearing magmas. *Journal of Volcanology and Geothermal Research*, 87(1-4):15 – 28, 1998.
- B. D. Marsh. On the crystallinity, probability of occurrence, and rheology of lava and magma. *Contributions to Mineralogy and Petrology*, 78(1): 85–98, 1981. doi: 10.1007/BF00371146.
- M. Matsushita. Fractal Viewpoint of Fracture and Accretion. *Journal of the Physical Society of Japan*, 54:857, 1985.
- J. Mewis and C. Macosko. *Rheology Principles, Measurements and Applications*. Wiley-VCH, 1994.
- J. V. Milewski. A packing study of milled fiber glass and glass beads. *ACS Division of Organic Coatings and Plastics Chemistry Preprints*, 33(2): 57–66, 1973.
- T. Murase and A. R. McBirney. Properties of some common igneous rocks and their melts at high temperatures. *Geological Society of America Bulletin*, 84:3653–3592, 1973.
- M. D. Murphy, R. S. J. Sparks, J. Barclay, M. R. Carroll, A.-M. Lejeune, T. S. Brewer, R. Macdonald, S. Black, and S. Young. The role of magma mixing in triggering the current eruption at the Soufriere Hills volcano, Montserrat, West Indies. *Geophysical Research Letters*, 25:3433–3436, 1998.
- L. V. Nardi, J. Plá-Cid, M. Bitencourt, and L. Z. Stabel. Geochemistry and petrogenesis of post-collisional ultrapotassic syenites and granites from southernmost Brazil: the Piquiri Syenite Massif. *Anais da Academia Brasileira de Ciências*, 80:353 – 371, 2008.
- J. S. Pallister, R. P. Hoblitt, and A. G. Reyes. A basalt trigger for the 1991 eruptions of Pinatubo volcano? *Nature*, 356(6368):426–428, 04 1992.

- S. Paterson. A review of criteria for the identification of magmatic and tectonic foliations in granitoids. *Journal of Structural Geology*, 11:349–363, 1989.
- S. Paterson, R. Vernon, and J. Žák. Mechanical instabilities and physical accumulation of K-feldspar megacrysts in granitic magma, Tuolumne batholith, California, USA. *Journal of the Virtual Explorer*, 18, 2005.
- S. R. Paterson. Magmatic tubes, pipes, troughs, diapirs, and plumes: Late-stage convective instabilities resulting in compositional diversity and permeable networks in crystal-rich magmas of the Tuolumne batholith, Sierra Nevada, California. *Geosphere*, 5(6):496–527, 2009.
- S. R. Paterson, G. S. Pignotta, and R. H. Vernon. The significance of microgranitoid enclave shapes and orientations. *Journal of Structural Geology*, 26(8):1465 – 1481, 2004.
- D. Perugini and G. Poli. Chaotic dynamics and fractals in magmatic interaction processes: a different approach to the interpretation of mafic microgranular enclaves. *Earth and Planetary Science Letters*, 175(1-2):93 – 103, 2000.
- D. Perugini and G. Poli. Viscous fingering during replenishment of felsic magma chambers by continuous inputs of mafic magmas: Field evidence and fluid-mechanics experiments. *Geology*, 33(1):5–8, 2005.
- D. Perugini, G. Poli, and G. D. Gatta. Analysis and simulation of magma mixing processes in 3D. *Lithos*, 65(3-4):313 – 330, 2002.
- D. Perugini, M. Petrelli, and G. Poli. Diffusive fractionation of trace elements by chaotic mixing of magmas. *Earth and Planetary Science Letters*, 243(3-4):669 – 680, 2006.
- D. Perugini, L. Valentini, and G. Poli. Insights into magma chamber processes from the analysis of size distribution of enclaves in lava flows: A case study from Vulcano Island (Southern Italy). *Journal of Volcanology and Geothermal Research*, 166:193–203, 2007.

- D. Perugini, A. Speziali, L. Caricchi, and U. Kueppers. Application of fractal fragmentation theory to natural pyroclastic deposits: Insights into volcanic explosivity of the Valentano scoria cone (Italy). *Journal of Volcanology and Geothermal Research*, 202, May 2011.
- N. Petford. Which effective viscosity? *Mineral Mag*, 73(2):167–191, 2009.
- N. Petford, R. C. Kerr, and J. R. Lister. Dike transport of granitoid magmas. *Geology*, 21(9):845–848, 1993.
- N. Petford, J. R. Lister, and R. C. Kerr. The ascent of felsic magmas in dykes. *Lithos*, 32(1-2):161 – 168, 1994.
- R. J. Phillips, R. C. Armstrong, R. A. Brown, A. L. Graham, and J. R. Abbott. A constitutive equation for concentrated suspensions that accounts for shear-induced particle migration. *Physics of Fluids A: Fluid Dynamics*, 4(1):30–40, 1992.
- C. Pin, M. Binon, J. M. Belin, B. Barbarin, and J. D. Clemens. Origin of microgranular enclaves in granitoids: equivocal Sr-Nd evidence from Hercynian rocks in the Massif Central (France). *J. Geophys. Res.*, 95 (B11):17821–17828, 1990.
- W. S. Pitcher. *The nature and origin of granite*. Geol. Soc. Am. Memoir, no. 5, 2 edition, 1997.
- R. L. Powell. Rheology of suspensions of rodlike particles. *Journal of Statistical Physics*, 62:1073–1094, 1991.
- M. Rahnama, D. L. Koch, and E. S. G. Shaqfeh. The effect of hydrodynamic interactions on the orientation distribution in a fiber suspension subject to simple shear flow. *Physics of Fluids*, 7(3):487–506, 1995.
- J. Reid, John B., D. P. Murray, O. D. Hermes, and E. J. Steig. Fractional crystallization in granites of the Sierra Nevada: How important is it? *Geology*, 21(7):587–590, 1993.

Bibliography

- J. B. Reid, O. C. Evans, and D. G. Fates. Magma mixing in granitic rocks of the central Sierra Nevada, California. *Earth and Planetary Science Letters*, 66:243 – 261, 1983.
- M. A. Richards and R. W. Griffiths. Deflection of plumes by mantle shear flow: experimental results and a simple theory. *Geophysical Journal*, 94 (3):367–376, 1988.
- R. Roscoe. The viscosity of suspensions of rigid spheres. *British Journal of Applied Physics*, 3(8):267–269, 1952.
- P. Ruprecht and O. Bachmann. Pre-eruptive reheating during magma mixing at Quizapu volcano and the implications for the explosiveness of silicic arc volcanoes. *Geology*, 38(10):919–922, 2010.
- P. Ruprecht, G. W. Bergantz, and J. Dufek. Modeling of gas-driven magmatic overturn: Tracking of phenocryst dispersal and gathering during magma mixing. *Geochemistry, Geophysics, Geosystems*, 9:Q07017, July 2008.
- A. E. Saal, E. H. Hauri, C. H. Langmuir, and M. R. Perfit. Vapour undersaturation in primitive mid-ocean-ridge basalt and the volatile content of Earth’s upper mantle. *Nature*, 419(6906):451–455, 10 2002.
- M. O. Saar, M. Manga, K. V. Cashman, and S. Fremouw. Numerical models of the onset of yield strength in crystal-melt suspensions. *Earth and Planetary Science Letters*, 187(3-4):367 – 379, 2001.
- S. Y. Sahin. Geochemistry of mafic microgranular enclaves in the tamdere quartz monzonite, south of dereli/giresun, eastern pontides, turkey. *Chemie der Erde - Geochemistry*, 68(1):81 – 92, 2008.
- C. G. Sammis, R. H. Osborne, J. L. Anderson, M. Banerdt, and P. White. Self-similar cataclasis in the formation of fault gouge. *Pure and Applied Geophysics*, 124:53–78, 1986.

Bibliography

- B. Scaillet, A. Whittington, C. Martel, M. Pichavant, and F. Holtz. Phase equilibrium constraints on the viscosity of silicic magmas II: implications for mafic-silicic mixing processes. *Geological Society of America Special Papers*, 350:61–72, 2000.
- J. Schmalzl, G. A. Houseman, and U. Hansen. Mixing in vigorous, time-dependent three-dimensional convection and application to Earth’s mantle. *Journal of Geophysical Research*, 101:21847–21858, 1996.
- T. Scott and D. Kohlstedt. The effect of large melt fraction on the deformation behavior of peridotite. *Earth and Planetary Science Letters*, 246(3-4):177 – 187, 2006.
- H. R. Shaw. Viscosities of magmatic silicate liquids; an empirical method of prediction. *Am J Sci*, 272(9):870–893, 1972.
- H. R. Shaw, T. L. Wright, D. L. Peck, and R. Okamura. The viscosity of basaltic magma; an analysis of field measurements in Makaopuhi lava lake, Hawaii. *American Journal of Science*, 266:225–264, 1968.
- A. Sierou and J. F. Brady. Rheology and microstructure in concentrated noncolloidal suspensions. *Journal of Rheology*, 46:1031, 2002.
- M. M. V. G. Silva, A. M. R. Neiva, and M. J. Whitehouse. Geochemistry of enclaves and host granites from the Nelas area, central Portugal. *Lithos*, 50(1-3):153 – 170, 2000. ISSN 0024-4937.
- J. H. Simmons, R. K. Mohr, and C. J. Montrose. Non-Newtonian viscous flow in glass. *Journal of Applied Physics*, 53(6):4075–4080, 1982.
- T. Sisson and G. Layne. H₂O in basalt and basaltic andesite glass inclusions from four subduction-related volcanoes. *Earth and Planetary Science Letters*, 117(3-4):619 – 635, 1993.
- T. W. Sisson, T. L. Grove, and D. S. Coleman. Hornblende gabbro sill complex at Onion Valley, California, and a mixing origin for the Sierra Nevada batholith. *Contributions to Mineralogy and Petrology*, 126:81–108, 1996.

Bibliography

- J. N. Skilbeck and J. A. Whitehead. Formation of discrete islands in linear island chains. *Nature*, 272(5653):499–501, 04 1978.
- J. V. Smith. Structures on interfaces of mingled magmas, Stewart Island, New Zealand. *Journal of Structural Geology*, 22(1):123 – 133, 2000.
- D. Snyder and S. Tait. Replenishment of magma chambers: comparison of fluid-mechanic experiments with field relations. *Contributions to Mineralogy and Petrology*, 122:230–240, 1995. ISSN 0010-7999.
- D. Snyder and S. Tait. Magma mixing by convective entrainment. *Nature*, 379(6565):529–531, 02 1996a.
- D. Snyder and S. Tait. Magma mixing by convective entrainment. *Nature*, 379(6565):529–531, 02 1996b.
- R. Sparks and L. Marshall. Thermal and mechanical constraints on mixing between mafic and silicic magmas. *Journal of Volcanology and Geothermal Research*, 29(1-4):99 – 124, 1986. ISSN 0377-0273.
- F. Spera, A. Borgia, J. Strimple, and M. Feigenson. Rheology of melts and magmatic suspensions 1. Design and calibration of concentric cylinder viscometer with application to rhyolitic magma. *Journal of Geophysical Research (Solid Earth)*, 93:10273–10294, 1988.
- J. J. Stickel and R. L. Powell. Fluid mechanics and rheology of dense suspensions. *Annual Review of Fluid Mechanics*, 37:129–149, 2005.
- F. Storti, A. Billi, and F. Salvini. Particle size distributions in natural carbonate fault rocks: insights for non-self-similar cataclasis. *Earth and Planetary Science Letters*, 206(1-2):173 – 186, 2003.
- C. A. Stover, D. L. Koch, and C. Cohen. Observations of fibre orientation in simple shear flow of semi-dilute suspensions. *Journal of Fluid Mechanics*, 238:277–296, 1992.

Bibliography

- G. I. Taylor. The viscosity of a fluid containing small drops of another fluid. *Proceedings of the Royal Society of London. Series A, Containing Papers of a Mathematical and Physical Character (1905-1934)*, 138:41–48, 1932.
- F. J. Tepley, J. P. Davidson, and M. A. Clynne. Magmatic interactions as recorded in plagioclase phenocrysts of Chaos Crags, Lassen Volcanic Center, California. *Journal of Petrology*, 40(5):787–806, 1999.
- N. Thomas and S. Tait. The dimensions of magmatic inclusions as a constraint on the physical mechanism of mixing. *Journal of Volcanology and Geothermal Research*, 75(1-2):167 – 178, 1997.
- N. Thomas, S. Tait, and T. Koyaguchi. Mixing of stratified liquids by the motion of gas bubbles: application to magma mixing. *Earth and Planetary Science Letters*, 115(1-4):161 – 175, 1993.
- O. Tobisch, B. McNulty, and R. Vernon. Microgranitoid enclave swarms in granitic plutons, central Sierra Nevada, California. *Lithos*, 40(2-4):321 – 339, 1997.
- O. T. Tobisch and A. R. Cruden. Fracture-controlled magma conduits in an obliquely convergent continental magmatic arc. *Geology*, 23(10):941–944, 1995.
- D. L. Turcotte. Fractals and fragmentation. *Journal of Geophysical Research*, 91:1921–1926, 1986.
- R. Turnbull, S. Weaver, A. Tulloch, J. Cole, M. Handler, and T. Ireland. Field and Geochemical Constraints on MaficFelsic Interactions, and Processes in High-level Arc Magma Chambers: an Example from the Halfmoon Pluton, New Zealand. *Journal of Petrology*, 51(7):1477–1505, 2010.
- J. Turner and I. Campbell. Convection and mixing in magma chambers. *Earth-Science Reviews*, 23(4):255 – 352, 1986. ISSN 0012-8252.
- J. Žák and S. Paterson. Characteristics of internal contacts in the Tuolumne batholith, central Sierra Nevada, California (USA): Implications for

Bibliography

- episodic emplacement and physical processes in a continental arc magma chamber. *Geological Society of America Bulletin*, 117:1242–1255, 2005.
- G. Ventura, P. D. Gaudio, and G. Iezzi. Enclaves provide new insights on the dynamics of magma mingling: A case study from Salina Island (Southern Tyrrhenian Sea, Italy). *Earth and Planetary Science Letters*, 243(1-2): 128 – 140, 2006.
- R. H. Vernon. Microgranitoid enclaves in granites—globules of hybrid magma quenched in a plutonic environment. *Nature*, 309(5967):438–439, 1984.
- P. Wallace and A. Anderson. *Volatiles in Magmas*. In: *H. Sigurdsson et al. (Editors) Encyclopedia of Volcanoes*. Academic Press, 1999.
- P. Wallace, A. Anderson, and A. Davis. Gradients in H₂O, CO₂ and exsolved gas in a large-volume silicic magma system: interpreting the record preserved in melt inclusions from the Bishop Tuff. *Journal of Geophysical Research*, 104:20097–20122, 1999.
- P. J. Wallace. Volatiles in subduction zone magmas: concentrations and fluxes based on melt inclusion and volcanic gas data. *Journal of Volcanology and Geothermal Research*, 140(1-3):217 – 240, 2005.
- S. L. Webb and D. B. Dingwell. Non-Newtonian rheology of igneous melts at high stresses and strain rates: experimental results for rhyolite, andesite, basalt, and nephelinite. *Journal of Geophysical Research (Solid Earth)*, 95:15695–15701, 1990.
- R. Weinberg, A. Sial, and R. Pessoa. Magma flow within the Tavares pluton, northeastern Brazil: Compositional and thermal convection. *Geological Society of America Bulletin*, 113(4):508–520, 2001.
- P. Welch. The use of fast Fourier transform for the estimation of power spectra: A method based on time averaging over short, modified periodograms. *Audio and Electroacoustics, IEEE Transactions on*, 15(2):70 – 73, June 1967.

Bibliography

- J. A. Whitehead. Fluid models of geological hotspots. *Annual Review of Fluid Mechanics*, 20:61–87, 1988.
- R. Wiebe, D. Smith, M. Sturm, E. King, and M. Seckler. Enclaves in the Cadillac Mountain granite (coastal Maine): samples of hybrid magma from the base of the chamber. *Journal of Petrology*, 38(3):393–423, 1997.
- R. A. Wiebe. Structural and magmatic evolution of a magma chamber: the Newark Island layered intrusion, Nain, Labrador. *Journal of Petrology*, 29(2):383–411, 1988.
- R. A. Wiebe. The Pleasant Bay layered gabbro-diorite, coastal Maine: ponding and crystallization of basaltic injections into a silicic magma chamber. *Journal of Petrology*, 34(3):461–489, 1993.
- R. A. Wiebe. Silicic magma chambers as traps for basaltic magmas: The Cadillac Mountain intrusive complex, Mount Desert Island, Maine. *The Journal of Geology*, 102(4):pp. 423–437, 1994.
- R. A. Wiebe. Mafic-silicic layered intrusions: the role of basaltic injections on magmatic processes and the evolution of silicic magma chambers. *Geological Society of America Special Papers*, 315:233–242, 1996.
- R. A. Wiebe and S. D. Adams. Felsic enclave swarms in the Gouldsboro granite, coastal Maine: a record of eruption through the roof of a silicic magma chamber. *The Journal of Geology*, 105(5):pp. 617–628, 1997.
- R. A. Wiebe and W. J. Collins. Depositional features and stratigraphic sections in granitic plutons: implications for the emplacement and crystallization of granitic magma. *Journal of Structural Geology*, 20(9-10): 1273 – 1289, 1998.
- R. A. Wiebe, M. Jellinek, M. J. Markley, D. P. Hawkins, and D. Snyder. Steep schlieren and associated enclaves in the Vinalhaven granite, Maine: possible indicators for granite rheology. *Contributions to Mineralogy and Petrology*, 153:121–138, 2007.

- C. R. Wildemuth and M. C. Williams. Viscosity of suspensions modeled with a shear-dependent maximum packing fraction. *Rheologica Acta*, 23: 627–635, 1984.
- H. G. Wilshire. Mineral layering in the Twin Lakes Granodiorite. *Geol. Soc. Am. Memoir*, 115:235261, 1969.
- C. Wilson, B. Houghton, M. McWilliams, M. Lanphere, S. Weaver, and R. Briggs. Volcanic and structural evolution of Taupo Volcanic Zone, New Zealand: a review. *Journal of Volcanology and Geothermal Research*, 68 (1-3):1 – 28, 1995.
- A.-B. Yu, N. Standish, and A. McLean. Porosity calculation of binary mixtures of nonspherical particles. *Journal of the American Ceramic Society*, 76(11):2813–2816, 1993.

Appendix A

Appendix

A.1 General concept of rheology

Rheology is the branch of physics that deals with the deformation and flow of materials. Specifically, rheology describes how a material will behave in response to an applied stress.

A.1.1 Mathematical description

A rheological law is a constitutive equation that relates the stress on a material (solid or fluid) to the strain (or strain-rate) it experiences via measurable parameters (e.g. viscosity of a fluid). In doing so, it relates two second-order tensors by using a fourth-order tensor. The general form of the equation is given by

$$\tau_{ij} = c_{ijkl}\epsilon_{ij} \tag{A.1}$$

where τ_{ij} is stress and ϵ_{ij} is strain. For a linear elastic material, c_{ijkl} is the fourth-order elastic modulus tensor. It has 81 components. If the material is isotropic (i.e. when the constitutive equation is isotropic and the array of constants c_{ijkl} remains unaffected with respect to rotation or reflection of coordinates), the number of elastic constants shrinks from 81 to 2—the elastic modulus and Poisson’s ratio. Elastic behavior obeys Hooke’s law, which states that the force (stress) applied is equal to the strain experienced by a material multiplied by the elastic modulus. This type of behavior results in instantaneous strain with the application of stress, where stress and strain are linearly related and the strain is recoverable below a certain amount strain (i.e. Hooke’s law is not valid at large strains). Elastic behavior is well represented by the behavior of a spring (Figure A.1a).

A.1. General concept of rheology

For a fluid, the two material coefficients that relate stress and strain rate are the viscosity μ and the second coefficient of viscosity λ . Stresses on the x-plane are

$$\tau_{xx} = -p + 2\mu\epsilon_{xx} + \lambda(\epsilon_{xx} + \epsilon_{yy} + \epsilon_{zz}) \quad \tau_{xy} = 2\mu\epsilon_{xy} \quad (\text{A.2})$$

In the absence of a velocity field, the normal stress is equal to the hydrostatic pressure. In terms of velocity gradients eq. A.2 becomes

$$\tau_{xx} = -p + 2\mu\frac{\partial u}{\partial x} + \lambda\nabla \cdot \mathbf{u} \quad \tau_{xy} = 2\mu\left(\frac{\partial u}{\partial y} + \frac{\partial v}{\partial x}\right) \quad (\text{A.3})$$

For incompressible fluid, μ is the only material property in the constitutive equation.

A.1.2 Rheology models

The rheology of fluids is subdivided into two classes—Newtonian and non-Newtonian. Newtonian viscous behavior is commonly modeled by a dashpot (Fig. A.1b), whereby the strain-rate is linearly proportional to the applied stress through the viscosity (Fig. A.2). Any departure from this behavior is said to be non-Newtonian. For an incompressible fluid, the flow is unaffected by changes in hydrostatic pressure (normal stresses) so the pressure term (isotropic stress) in equation A.2 can be ignored the total stress τ_{ij} will be taken to be the shear stress only. All the models presented in this proposal assume that the fluid is incompressible.

Broadly speaking, non-Newtonian fluids can be subdivided into two classes: time-independent fluids $\eta = \mu(\dot{\epsilon})$ and time-dependent fluids $\eta = \mu(\dot{\epsilon}, t)$. For the time-independent case, viscosity depends on strain-rate and can be modeled using a power law

$$\tau = \eta\dot{\epsilon}^n \quad (\text{A.4})$$

where n is the flow behavior index. The viscosity is reported at a specific strain-rate as an “apparent viscosity,” η . This class of non-Newtonain fluids

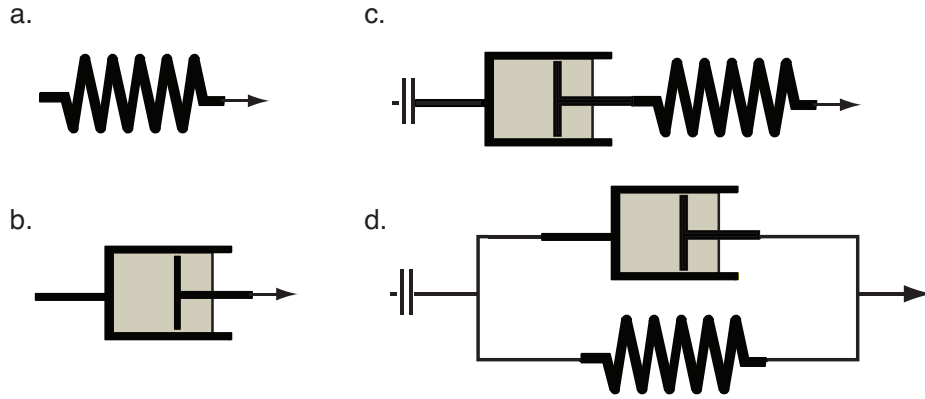


Figure A.1: Spring and dashpot models for the deformation of materials. *a.* elastic model; *b.* viscous model; viscoelastic models: dashpot and spring in *c.* series and *d.* parallel

is further subdivided into shear-thinning $n < 1$ (viscosity decreases with increasing strain-rate) and shear-thickening $n > 1$ (viscosity increases with increasing strain-rate) (Fig. A.2). For the time-dependent case, viscosity depends both on strain-rate and the time over which the strain-rate is applied. Time-dependent fluids are subdivided into thixotropy behavior (a decrease in apparent viscosity over time under a constant strain-rate or applied stress, followed by a gradual recovery upon removal of strain-rate or applied stress) and rheopexy behavior (an increase in apparent viscosity over time under a constant strain-rate or applied stress, followed by a gradual recovery upon removal of strain-rate or applied stress).

Ideal plastic behavior means that no deformation occurs below a critical yield stress τ_o . For the case of a Bingham plastic, above τ_o , the material behaves like a Newtonian fluid with constant viscosity (Fig. A.2)

$$\tau = \tau_o + \mu\dot{\epsilon}. \quad (\text{A.5})$$

Below the yield stress, the material behaves like a solid. The Herschel-Bulkley model describes viscoplastic material that exhibits yielding behavior below a critical yield stress and exhibits power-law behavior (i.e. shear

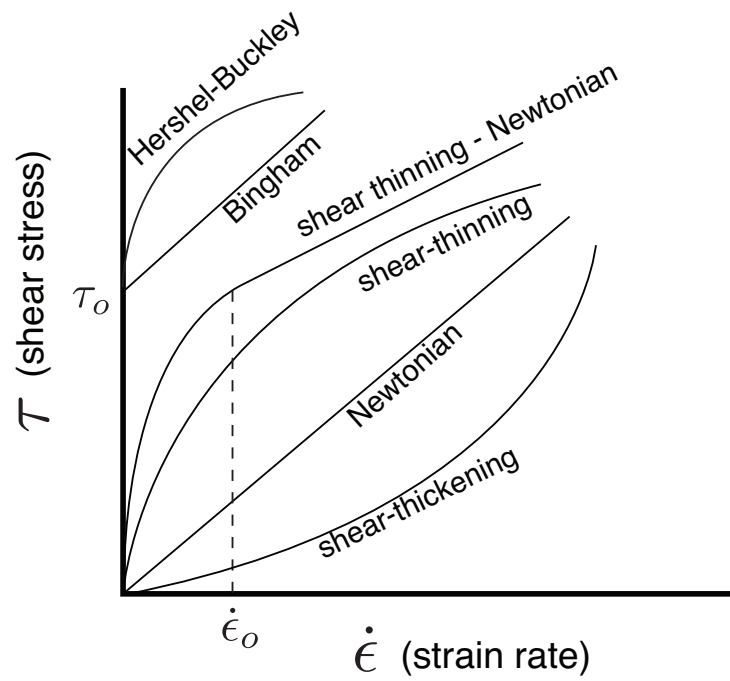


Figure A.2: Stress-strain rate curves for various rheology models.

A.1. General concept of rheology

thinning) once the yield stress has been reached

$$\tau = \tau_o + \eta\dot{\epsilon}^n. \quad (\text{A.6})$$

The physical rationale behind shear thinning behavior can be attributed to mechanisms such as the alignment of elongate particles with flow direction, deformation of spherical droplets (e.g. squishing bubbles) in a fluid, or breaking up particle aggregates in a suspension.

Viscoelastic behavior combines both an elastic response for which, according to Hooke's law, stress is directly proportional to strain, but independent of strain-rate and a viscous response for which, according to Newton's Law, stress is proportional to strain-rate, but independent of strain. Viscoelastic materials, unlike elastic materials which store all energy due to deformation, dissipate energy under deformation. This phenomenon is called hysteresis (see Fig. A.3a).

Stress relaxation and creep are two important properties of viscoelastic material. Stress relaxation occurs when the stress on a material reaches a peak under fixed strain and then decreases (or relaxes) over time (see Fig. A.3b). A common model for viscoelastic behavior, specifically stress relaxation, is Maxwell's model of a dashpot and spring in series (Fig. A.1c). In this case, the stresses are equal and the strains (viscous + elastic) are additive (i.e. the total deformation is equal to the sum of deformation in the spring and in the dashpot). Under a constant applied stress, the spring deforms (stretches) according to Hooke's Law. At a later time, the dash-pot begins to flow as the spring gradually returns to its original length. The total strain is given by:

$$\epsilon = \frac{\tau}{\mu}t + \frac{\tau}{E} \quad (\text{A.7})$$

Where μ is the viscosity of the dashpot and E is the elastic modulus of the spring. Once the material has fully responded to the force (stress) and the force is removed, the material does not return to its original dimensions due to flow of the dashpot (i.e. strain is not fully recoverable). A Maxwell material subjected to a instantaneous constant strain will undergo stress

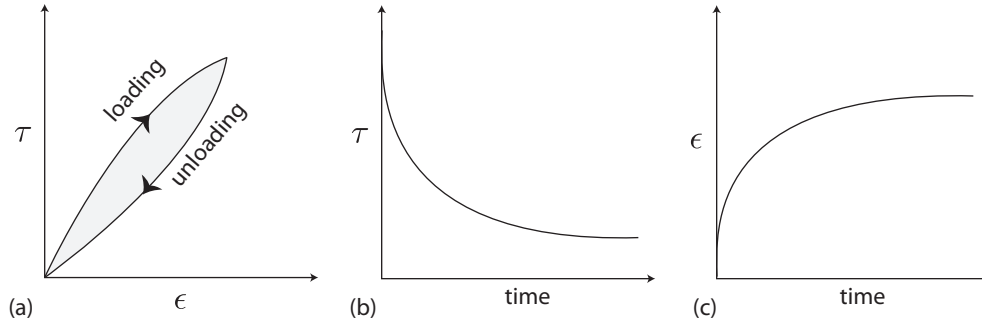


Figure A.3: (a) Stress-strain curves show hysteresis of loading and unloading of viscoelastic material. Shaded region between curves represents energy dissipation. (b) Stress relaxation with time for viscoelastic material held under fixed strain. (c) Creep of viscoelastic material with time under instantaneously-applied constant stress.

relaxation over time.

$$\tau = \tau_o \exp\left(-\frac{E}{\mu}t\right) \quad (\text{A.8})$$

The characteristic time for this process is called the relaxation time—a measure of the time required for the stored energy in the spring to move to the dashpot and dissipate—and is given by:

$$t_{relax} = \frac{\mu}{E} \quad (\text{A.9})$$

Creep refers to the general characteristic of a viscoelastic material to undergo increased deformation under a constant stress, until an asymptotic level of strain is reached (see Fig. A.3c). This phenomenon is conventionally studied using a Kelvin model, which illustrates a type of viscoelastic behavior whereby a dashpot and spring are arranged in parallel (Fig. A.1d). Because of this arrangement, the deformation is equal in both elements, but the total stress applied is the sum of the stress on the spring and the stress on the dashpot:

$$\tau = E\epsilon + \mu\dot{\epsilon}. \quad (\text{A.10})$$

As the material deforms, its movement is hindered by the elastic response of the spring which provides a continuously increasing restoring force to

prevent deformation. When the force is removed, the material returns to its original shape; however, the restoring process is slowed by the viscous response of the dashpot. Under constant applied stress, the elastic response of the spring is suppressed by the dashpot and the strain on the material evolves as:

$$\epsilon = \frac{\tau}{E} \left[1 - \exp\left(-\frac{E}{\mu}t\right) \right]. \quad (\text{A.11})$$

The Maxwell and Kelvin models are not valid for large strains.

Another type of yielding behavior is characterized by a yield strain (see Fig. A.2). Deformation at low strain-rates exhibits non-Newtonian behavior (e.g. shear-thinning) and past a certain strain-rate (or strain) the material behaves like a Newtonian fluid.

A.2 Suspension rheology

A.2.1 Flow around rigid particles

The volume fraction of particles in a suspending fluid has a large effect on the rheological properties of the suspension which macroscopically can lead to, e.g., power-law, plastic, and/or yielding behavior. Particles affect the properties of a suspension in three ways:

1. Particles increase viscosity because flow must go around them (see Fig. A.4).
2. At the particle-fluid boundary there exists a layer of fluid that is essentially “stuck” to the particle making that part of the flow more or less rigid.
3. Particles can interact with each other generating their own velocity field which can lead to hydrodynamic (i.e. non-Brownian) self diffusion. The diffusion of particles causes concentration and viscosity gradients in the suspension.

For these reasons, viscosity models for particle-fluid mixtures characterize the effective viscosity of the suspension as a function of the solid volume

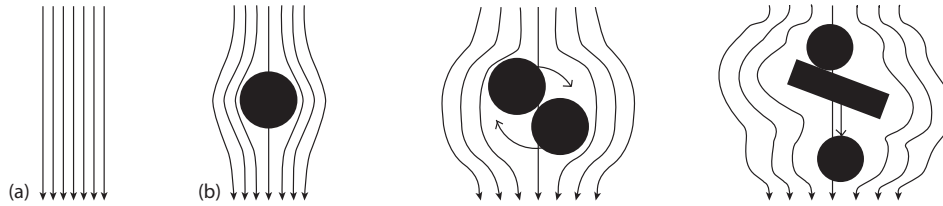


Figure A.4: (a) Flow-lines in a laminar flow of particle-free fluid far from a stationary boundary. (b) Influence of particles on flow-lines.

fraction,

$$\eta = \eta(\phi) \quad (\text{A.12})$$

However, given that most suspensions do not contain a uniform size, shape, and distribution of particles, equation A.12 should have the form:

$$\eta = \eta(\phi, \text{other details of the microstructure}) \quad (\text{A.13})$$

Where “other details of the microstructure” includes particle shape, size distribution, and the nature of particle-particle interactions.

Examples of particles suspended in a viscous fluid exist widely in nature (e.g. wet sediments and crystal-rich magmas) and in industry (e.g. cement and salsa). A long-standing problem in studies of particle suspensions has been to calculate the effective viscosity of the suspension. Due to variables such as particle concentration, shape, size, and interactions, a flowing suspension cannot accurately be described as a Newtonian fluid. Therefore, suspensions are commonly treated as non-Newtonian fluids. Observations of non-Newtonian behavior in particle suspensions—i.e. shear thinning/thickening, yielding behavior, etc.—come from early studies on suspension rheology [Bagnold, 1954; Jeffrey and Acrivos, 1976]. An ongoing problem has been to determine the link between bulk macroscopic properties of the suspension, which can be measured with a rheometer, and the particle-scale microstructure. Stickel and Powell [2005] describe a particle suspension’s viscosity as a function of several variables:

$$\eta = f(r, \rho_p, n, \eta_o, \rho_o, kT, \dot{\epsilon}, t), \quad (\text{A.14})$$

A.2. Suspension rheology

where the variables r , ρ_p , and n are the radius, density, and number concentration of the particles; η_o and ρ_o are the viscosity and density of the suspending fluid; kT is the thermal energy, $\dot{\epsilon}$ is the strain-rate, and t is time. The variables in Equation A.14 can be non-dimensionalized to give:

$$\eta_r = f(\phi, \rho_r, \text{Pe}, \text{Re}, t_r), \quad (\text{A.15})$$

where

$$\begin{aligned} \eta_r &= \frac{\eta}{\eta_o}, & \phi &= \frac{4\pi}{3}nr^3, \\ \rho_r &= \frac{\rho_p}{\rho_o}, & \text{Pe} &= \frac{6\pi\eta_o r^3 \dot{\epsilon}}{kT}, \\ \text{Re} &= \frac{\rho_o r^2 \dot{\epsilon}}{\eta_o}, & \text{and } t_r &= \frac{tkT}{\eta_o r^3}. \end{aligned}$$

Assuming the particles are neutrally buoyant and the flow is steady, the viscosity only depends on the particle fraction ϕ , the Peclet number Pe and the particle Reynolds number Re . The influence of Brownian motion is determined by the Peclet number [Mewis and Macosko, 1994] (i.e. Brownian motion occurs when $\text{Pe} \leq 1$), which describes the balance between hydrodynamic forces, which tend to align particles with the flow, and Brownian motion, which leads to randomization of particle orientation as a result of thermal fluctuations. Particles small enough to experience Brownian forces are constantly bombarded by molecules in the suspending fluid. These collisions cause the Brownian particle to undergo a random walk. If $\text{Pe} \geq 1$, particles may experience non-reversible interactions leading to hydrodynamic self-diffusion. This process can cause particle migration from regions of high strain-rate (i.e. high number of particle interactions) to low strain-rate (i.e. low number of particle interactions).

The suspensions discussed in this proposal have low particle Reynolds number (i.e. inertial forces are negligible) and high Peclet number (i.e. particles do not undergo Brownian motion). In suspensions of this type, particles interact via hydrodynamic (i.e. due to relative motion of particles and fluid and generated by particle-fluid motion) and interparticle (i.e. due to colli-

sions between particles) forces.

A.2.2 Particle shape and rheology

Spheres

See section A.3.3.

Rods

Since most natural suspensions rarely contain mono-dispersed spheres, it is useful to understand the rheology of non-spherical particles, e.g. rod-like particles, suspended in a Newtonian fluid. Hydrodynamic and particle interactions become more complex in these systems. The suspension's viscosity is a function of particle-fluid and particle-particle interactions, which depend on particle aspect ratio and concentration. The particle concentration is defined by the volume fraction of particles and the particle aspect ratio is $\frac{L}{d}$, where L is the particle's length and d is the particle's diameter. Bearing in mind this is a complicated stress coupling, there are three regimes for particle concentrations:

1. Dilute: when particles do not interact, $nL^3 \ll 1$, where n is the number of particles per unit volume.
2. Semi-dilute: when particles interact primarily through long-range hydrodynamic interactions, $nL^3 > 1$, but $nL^2d \ll 1$.
3. Concentrated: when additional non-hydrodynamic interactions become important, $nL^2d > 1$

Experiments by Milewski [1973] show that for rigid cylinders packed in random orientation the maximum volume fraction decreases with increasing aspect ratio.

The viscosity of a suspension can be related to the work required to maintain the motion of the suspended particles, which is influenced by the shape and orientation (for non-spherical particles) of the particles. Happel

A.2. Suspension rheology

[1957] defines the rate of work W required to shear a volume of fluid as:

$$\frac{dW}{dt} = \eta \dot{\epsilon}^2 V \quad (\text{A.16})$$

Where η is the apparent viscosity of the fluid, $\dot{\epsilon}$ is the strain rate, and V is the fluid's volume. If the fluid contains particles, the total rate of work required is the sum of the rate of work necessary to shear an identical volume of particle-free fluid plus the extra rate of work from the presence of the particle. The apparent viscosity of the suspension is given by:

$$\eta = \frac{\dot{W}_f}{\dot{\epsilon}^2 V} + \frac{\dot{W}_p}{\dot{\epsilon}^2 V} \quad (\text{A.17})$$

If the suspending fluid is Newtonian, the first term in equation A.17 is the Newtonian viscosity μ and the equation reduces to:

$$\eta_r = 1 + \frac{\dot{W}_p}{\mu \dot{\epsilon}^2 V_p} \phi \quad (\text{A.18})$$

Where ϕ is the particle volume fraction. Equation A.18 has the form of equation A.40 which is Einstein's equation for the viscosity of a dilute suspension of spheres. Here the B -term (which is 2.5 for spherical particles) is $\dot{W}/\mu \dot{\epsilon}^2 V_p$.

The work required to keep a particle in motion depends on shape and orientation (for non-spherical particles). Jeffery [1922] derives \dot{W}_p in his equation 61:

$$\frac{dW}{dt} = \frac{4}{3} \pi \mu \kappa^2 \left[\left(\frac{\alpha_o}{2b^2 \alpha'_o \beta''_o} + \frac{1}{2b^2 \alpha'_o} - \frac{2}{\beta'_o (a^2 b^2)} \right) \sin^4 \theta \sin^2 2\phi + \frac{1}{b^2 \alpha'_o} \cos^2 \theta + \frac{2}{\beta'_o (a^2 + b^2)} \sin^2 \theta \right] \quad (\text{A.19})$$

which can be used to determine a particle's instantaneous contribution to viscosity as a function of the particle's orientation in the flow (see Jeffery [1922] for definition of parameters α_o , β'_o , α'_o , β''_o , a , b). In Figure A.5, equation A.19 is solved to calculate the Einstein coefficient B ($\dot{W}/\mu \dot{\epsilon}^2 V_p$) that is used to represent the viscosity. The viscosity is smallest when the

A.2. Suspension rheology

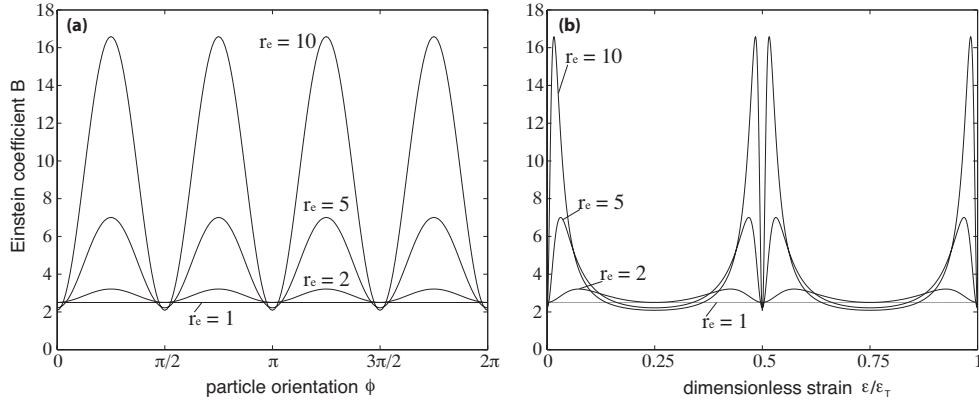


Figure A.5: A particle’s instantaneous contribution to the viscosity of a dilute suspension as a function of (a) particle orientation and (b) strain. Strain is made dimensionless by the amount of strain after one period of rotation.

particle is oriented at $\pi/2$ and π (perpendicular or parallel to the flow). At $\pi/2$ the particle is parallel to the flow and so does not cause a significant disturbance to the flowlines. At π the particle is perpendicular to the flow but is moving at the same speed as the fluid and so there is little distortion to the flowlines. The viscosity is largest at $\pi/4$ as the particle presents a large profile to the flow and moves at a slower speed than the flow. Figure A.5b shows the viscosity as a function of strain. For this case, B was computed by calculating a particle’s orientation as a function of strain. The amount of time a particle spends in a given orientation depends on the orientation, such that a plot of strain vs. viscosity shows the contribution of time as the particle rotates through one orbit. The largest contribution to viscosity comes just before and after the particle is perfectly aligned with the flow since it spends the most time close to this orientation and moves quickly through the other orientations (recall that flip over time scales with r^{-1}).

A.2.3 Particle behavior in a shear flow

The motion of an ellipsoid particle in a shear flow can be described by Jeffery orbits (Figure A.6b). Jeffery [1922] solved the equations of motion

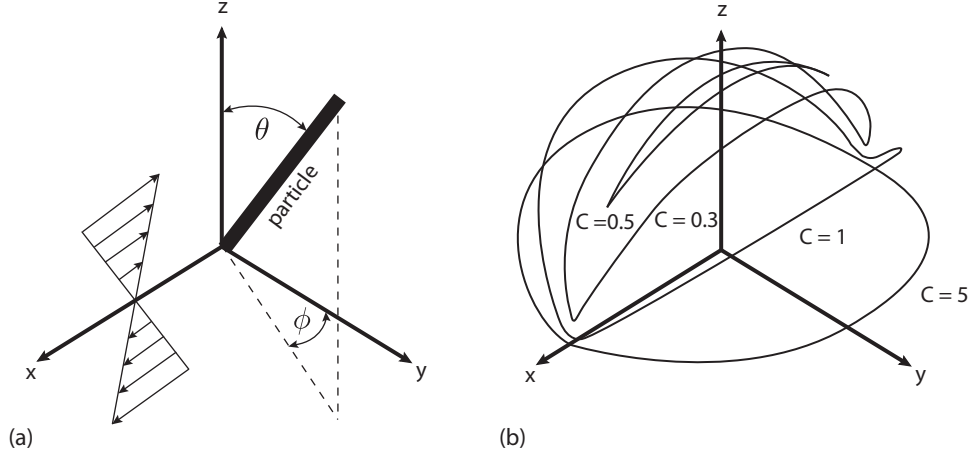


Figure A.6: (a) Orientation angles, ϕ and θ of a particle undergoing motion in a simple shear flow. (b) Jeffery orbits for different values of the orbit constant C for a simple shear flow in the xy plane, modified from Stover et al. [1992].

for non-interacting rigid ellipsoidal particles immersed in a Newtonian fluid.

He predicted that a single particle, in the absence of particle-particle interactions, undergoes periodic rotations in a spherical orbit. The particle rotates with a period given by:

$$T = \frac{2\pi}{\dot{\epsilon}} \left(r_e + \frac{1}{r_e} \right) \quad (\text{A.20})$$

Where $\dot{\epsilon}$ is the magnitude of the local strain rate and r_e is the aspect ratio of the particle. The differential equations which govern the motion of particles in simple shear [Jeffery, 1922] are:

$$\frac{d\phi}{dt} = \frac{\dot{\epsilon}}{r_e^2 + 1} (r_e^2 \cos^2 \phi + \sin^2 \phi) \quad (\text{A.21})$$

and

$$\frac{d\theta}{dt} = \dot{\epsilon} \left(\frac{r_e^2 - 1}{r_e^2 + 1} \right) \sin \theta \cos \theta \sin \phi \cos \phi \quad (\text{A.22})$$

A.2. Suspension rheology

The two angles that characterize the orientation of the particle are ϕ , measured from the y direction, and θ , measured from the z direction (see Fig. A.6a). Each closed trajectory (i.e. Jeffery orbit) is characterized by an orbit constant, C , which is given by:

$$C = \frac{\tan \theta (r_e^2 \cos^2 \phi + \sin^2 \phi)^{\frac{1}{2}}}{r_e} \quad (\text{A.23})$$

In a simplified case in which the particle only rotates in the $x - y$ plane, Jeffery's equation becomes:

$$\begin{aligned} \frac{d\phi}{dt} = & \left(\frac{r_e^2}{r_e^2 + 1} \right) \left[-\sin \phi \cos \phi \frac{\partial v_x}{\partial x} - \sin^2 \phi \frac{\partial v_x}{\partial y} + \cos^2 \phi \frac{\partial v_y}{\partial x} + \sin \phi \cos \phi \frac{\partial v_y}{\partial y} \right] \\ & - \left(\frac{1}{r_e^2 + 1} \right) \left[-\sin \phi \cos \phi \frac{\partial v_x}{\partial x} + \cos^2 \phi \frac{\partial v_x}{\partial y} - \sin^2 \phi \frac{\partial v_y}{\partial x} + \sin \phi \cos \phi \frac{\partial v_y}{\partial y} \right]. \end{aligned} \quad (\text{A.24})$$

Where ϕ describes the particle's orientation and the velocity gradient is, e.g., $\partial v_x / \partial x$. This equation does not account for particle-particle interactions. The particle's orientation only changes with the rotation of the suspending fluid.

The rotation of elongate particles in a shear flow can lead to alignment. Particles in a simple shear flow will rotate continuously, spending part of the time aligned with the flow and the rest of the time unaligned with the flow. The time spent at different orientations within the orbit depends on the particle's aspect ratio and the strain rate. Long slender particles spend most of their time lined up with the flow and the "flip-over" time (i.e. the time for rotation through π in the xy -plane) is of the order of r^{-1} . Figure A.7b shows the angular velocity of a particle with an aspect ratio ≥ 1 as it rotates through a closed orbit. The probability of a particle having a certain orientation is inversely proportional to the particle's angular velocity at that orientation. For particles with aspect ratios ≥ 1 there is a high probability that the particle will be oriented at $\pi/2$ or $3\pi/2$. At these orientations, the particle's angular velocity is the smallest (Fig. A.7b) such that the particle stays in (or close to) this orientation much longer than it does at 0 , π , or

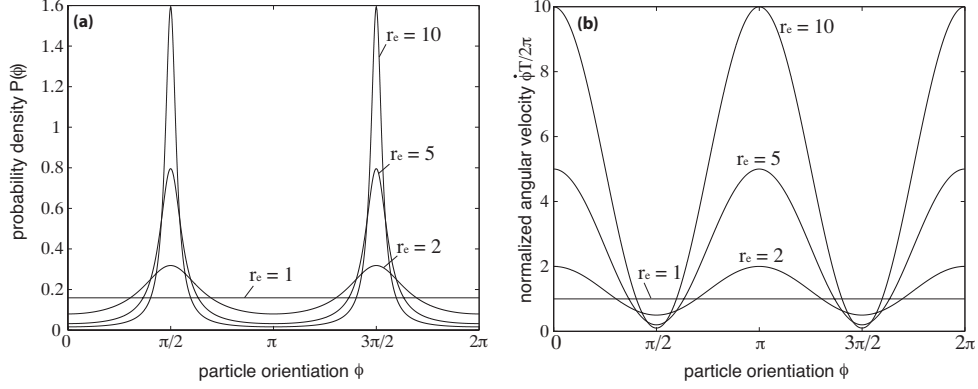


Figure A.7: (a) The probability density function in the ϕ -direction for particles with aspect ratios between 1 and 10. (b) Angular velocity of different aspect ratio particles in a simple shearing flow as a function of particle orientation. Equation A.21 describes the angular velocity which is normalized by the average angular velocity ($2\pi/T$).

2π . The probability density function for a particle's ϕ -orientation is

$$p(\phi) = \frac{1}{T\dot{\epsilon}} \left(\frac{r_e + 1}{r_e^2 \cos^2 \phi + \sin^2 \phi} \right) \quad (\text{A.25})$$

where T is a normalizing constant such that the integral over all orientation (0 to 2π) is equal to 1 for any aspect ratio (Figure A.7a).

Manga [1998] found a steady-state distribution of the orientation of slender rods in a simple shear flow by integrating equations A.21 and A.22 for one million randomly oriented, non-interacting ellipsoids with aspect ratio $r_e = 10$ (Fig. A.8). He characterizes the orientation distribution according to the standard deviation of the angles ϕ and θ . Similar to results obtained by Gay [1966], Manga [1998] reports that during pure shear, elongate particles will ultimately become almost perfectly aligned. These theoretical studies do not take into account particle-particle interactions.

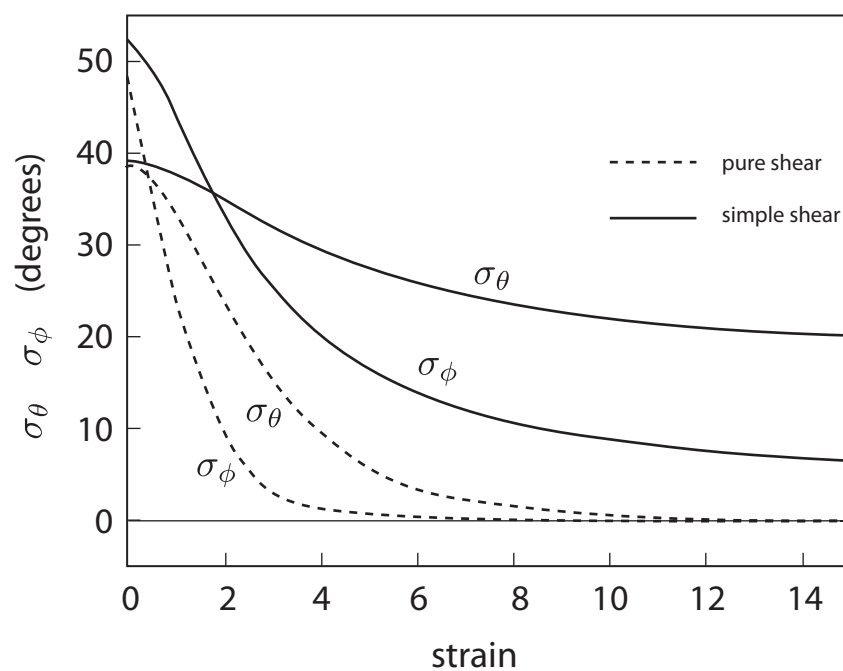


Figure A.8: Orientation distribution as a function of strain during pure and simple shear. σ_ϕ and σ_θ are the standard deviation of the angles ϕ and θ , modified from Manga [1998].

A.2.4 Hydrodynamic particle diffusion in semi-dilute and concentrated suspensions

Studies on semi-dilute and concentrated suspensions require detailed consideration of both particle interactions and the microstructure configuration. Both experimental [Folgar and Tucker, 1984; Leighton and Acrivos, 1987; Huang and Bonn, 2007] and numerical [Brady and Bossis, 1985; Sierou and Brady, 2002] investigations on concentrated suspensions of rigid spheres have made significant progress in quantifying and describing the behavior of these systems.

Rotary diffusion model: fibers in shear flow

The orientation distribution of fibers depends on the type of flow (e.g. pure or simple shear), particle concentration, geometry, and the rheology of the suspending fluid. Folgar and Tucker [1984] developed a theoretical model to predict the orientation distribution in concentrated suspensions of elongate particles undergoing pure and simple shear flow. They perform experiments of particles in simple shear flow and compare the steady-state orientation distributions between theory and experiment. Their model uses a statistical approach to predict a probability distribution function of particle orientation. The probability of a particle having an orientation between ϕ_1 and ϕ_2 is given by:

$$P[\phi_1 < \phi < \phi_2] = \int_{\phi_1}^{\phi_2} \psi_\phi(\phi') d\phi'. \quad (\text{A.26})$$

Here ψ_ϕ is independent of whether the particle is oriented at an angle ϕ or $\phi + \pi$. ψ_ϕ evolves in time according to

$$\frac{\partial \psi_\phi}{\partial t} = -\frac{\partial}{\partial \phi}(\psi_\phi \dot{\phi}) \quad (\text{A.27})$$

where $\dot{\phi}$ is the average angular velocity of a rotating particle. Folgar and Tucker [1984] combine Jeffrey's equation (see equation A.24) for the orientation of a particle in the $x - y$ plane (setting r_e equal to infinity) with an

interaction term in an expression for $\dot{\phi}$:

$$\dot{\phi} = \left[-\sin \phi \cos \phi \frac{\partial v_x}{\partial x} - \sin^2 \phi \frac{\partial v_x}{\partial y} + \cos^2 \phi \frac{\partial v_y}{\partial x} + \sin \phi \cos \phi \frac{\partial v_y}{\partial y} \right] - \frac{C_1 \dot{\epsilon} \frac{\partial \psi_\phi}{\partial \phi}}{\psi_\phi} \quad (\text{A.28})$$

where C_1 is a constant determined from experiments and accounts for particle interactions. It depends on particle aspect ratio and the volume fraction of particles. In a concentrated suspension, particles undergo a series of interactions which reorient them out of a closed Jeffery orbit. Once disrupted from their original orbit, the particles start a new orbit, assuming rotation according to Jeffery's equation. The interruption of orbits via interaction with other particles leads to a randomization of particle orientations. The final form of the theory by Folgar and Tucker [1984] is:

$$\frac{\partial \psi_\phi}{\partial t} = C_1 \dot{\epsilon} \frac{\partial^2 \psi_\phi}{\partial \phi^2} - \frac{\partial}{\partial \phi} \left[\psi_\phi \left(\sin \phi \cos \phi \frac{\partial v_x}{\partial x} - \sin^2 \phi \frac{\partial v_x}{\partial y} + \cos^2 \phi \frac{\partial v_y}{\partial x} + \sin \phi \cos \phi \frac{\partial v_y}{\partial y} \right) \right]. \quad (\text{A.29})$$

The interactions between fibers in a suspension undergoing simple shear are random and cause small changes in the fiber's orientation. According to Rahnama et al. [1995], these small changes in orientation can be considered diffusive. They find that as a fiber rotates according to Jeffery's orbits, it creates a disturbance to the flow field which in a semi-dilute to concentrated suspension can alter the periodic rotation of neighboring fibers (within \sim one fiber length of the fibers center). The orientational diffusivity results from the hydrodynamics of the flow and is not caused by thermal motion of the molecules in the fluid. The diffusivity ratio $D_{\theta\theta}/D_{\phi\phi}$ represents the ratio between diffusivity in the θ and ϕ directions (recall Fig. A.6). A high diffusivity ratio means that particles are oriented nearly parallel to the vorticity axis. Rahnama et al. [1995] found that the diffusivity ratio does not systematically depend on particle concentration and geometry. For a given particle aspect ratio, the diffusivity ratio decreases as concentration increases which suggests that particles align with the flow direction (i.e. perpendicular to the vorticity axis) at higher particle concentrations. The steady-state

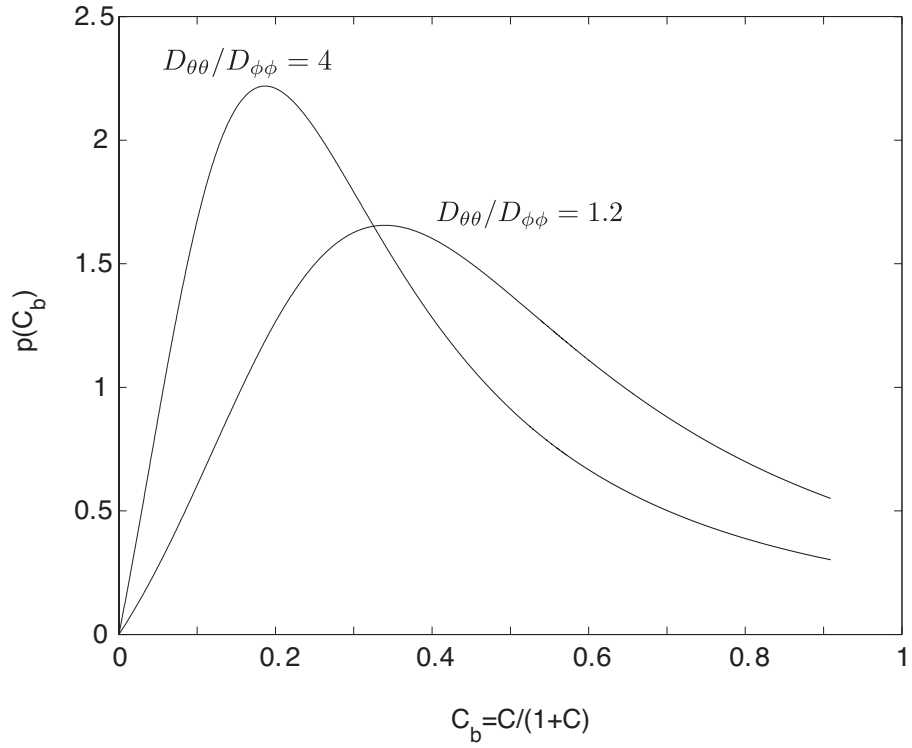


Figure A.9: Distribution of C_b ($C_b = C/(1 + C)$), where C is the orbit constant from equation A.23. Curves are from a model by Rahnama et al. [1995] modified from Manga [1998] for diffusivity ratios of 1.2 and 4.

orbit constant distribution is given by:

$$p(C_b) = \frac{4C_b \frac{D_{\theta\theta}}{D_{\phi\phi}}}{\left(4 \left[\frac{C_b}{1-C_b}\right]^2 \frac{D_{\theta\theta}}{D_{\phi\phi}} + 1\right)^{3/2} (1-C_b)^3} \quad (\text{A.30})$$

where $p(C_b)$ is the probability of a fiber having a certain C_b value ($(C_b = C/(1+C))$). Figure A.9 shows the probability distribution for diffusivity ratios of 4 and 1.2.

Diffusion model: Migrating spheres

Leighton and Acrivos [1987] investigate an observed decrease in a concentrated suspension's effective viscosity over time during experiments discussed in Gadala-Maria and Acrivos [1980]. They attribute the decrease in viscosity to particle migration out of the sheared gap in the Couette device. The migration, caused by irreversible particle-particle interactions, leads to a local decrease in particle concentration in regions of highest shear. During their experiments, they observe an initial viscosity-increase prior to the long-term viscosity decrease. They attribute the initial increase in viscosity to shear-induced particle migration from regions of high to low shear stress (gradients in shear stress). The viscosity increase reaches equilibrium after a total strain of $\sim 10^2$ while the viscosity decrease is not obvious until after a strain of $\sim 10^3$. They attribute the initial increase in viscosity to the observation that the initial suspension had a non-uniform concentration profile (which was set up by loading the sample into the Couette device) and when sheared, the particles diffuse to attain a uniform distribution—leading to an increase in viscosity. They model the diffusion process with the diffusion equation

$$\frac{\partial\phi}{\partial t} = D_{\perp} \frac{\partial^2\phi}{\partial z^2}; \quad 0 < z < h \quad (\text{A.31})$$

where $z = 0$ is the base of the gap and $z = h$ is the top of the gap. D_{\perp} is the diffusivity normal to the plane of shear and depends on concentration (although they assume the diffusion coefficient is constant during the migration process because the total concentration variation within the gap is

very small). The solution to equation A.31 is given by

$$\phi(z, t) = \phi^* + (\phi_o - \phi^*) \left[\frac{\hat{V}}{1 + \hat{V}} + \sum_{n=1}^{\infty} \frac{2 \exp(-\lambda_n^2 D_{\perp} t / h^2)}{(\lambda_n^2 + \hat{V}(1 + \hat{V}))} \left(\lambda_2 \sin \frac{\lambda_n z}{h} - \hat{V} \cos \frac{\lambda_n z}{h} \right) \right] \quad (\text{A.32})$$

The decrease in particle concentration in the gap given by equation A.32 leads to a decrease in observed suspension viscosity. They model this as the average viscosity in the gap:

$$\mu_{obs} = \frac{1}{h} \int_0^h \mu dz \quad (\text{A.33})$$

They use the viscosity data (increasing or decreasing) to estimate a diffusion coefficient D_{\perp} which is proportional to $\dot{\epsilon} a^2$ (a = particle radius and $\dot{\epsilon}$ = strain rate). They estimate D_{\perp} by matching the viscosity decrease predicted by their model to the observed decrease from the experiments. They attribute the migration of particles in concentrated suspensions to irreversible particle-particle interactions. As particles approach one another without any notable displacement from their original streamlines they can eventually come into physical contact, rotate due to vorticity in the shear flow, and finally split up. Because the particle is displaced from its streamline, the interaction is not reversible and leads to permanent displacements of the particles following each interaction. Additionally, particles can migrate across streamlines if there are viscosity gradients in the suspension. The viscosity gradients arise from concentration gradients. As two touching particles rotate in the presence of a viscosity gradient, the center of mass is no longer the center of rotation which causes the particles to be displaced from areas of high to low viscosity.

Phillips et al. [1992] develop a constitutive equation for concentrated suspensions that accounts for shear-induced particle migration. The SIM (shear induced migration) model which accounts for changes in the particle volume fraction of a sheared suspension. The particle conservation equation is given by

$$\frac{D\phi}{Dt} = -\nabla \cdot (N_c + N_{\mu}) \quad (\text{A.34})$$

where N_c and N_μ are particle fluxes resulting from particle interactions and viscosity, respectively. Particle interactions can cause a particle to move from its original streamline. A particle will tend to migrate away from regions of high collision frequency toward regions of low collision frequency. Said differently, the higher the strain-rate, the more opportunities particles have to interact (i.e. high collision frequency), which causes particles to migrate from high to low strain-rates. The number of particle collisions scales with $\dot{\epsilon}\phi$, where $\dot{\epsilon}$ is the local strain-rate. The particle flux due to interactions is

$$N_c = -K_c a^2 (\phi^2 \nabla \dot{\epsilon} + \phi \dot{\epsilon} \nabla \phi) \quad (\text{A.35})$$

where K_c is a constant determined by experimental data and a is the particle radius. The first half of the expression states that even in the absence of a concentration gradient, particles will migrate as the result gradients in strain-rate. The second half of equation A.35 states that a gradient in particle concentration will lead to a spatial distribution of particle interactions and hence the frequency of interactions. The gradient in particle concentration can also lead to spatial variations in viscosity, which causes particles to migrate from high to low viscosity. As two particles interact, one particle experiences a higher viscosity or resistance to motion relative to the other particle and so the center of their rotation is displaced in the direction of lower viscosity. The particle flux due to viscosity is given by

$$N_\mu = -K_\mu \dot{\epsilon} \phi^2 \left(\frac{a^2}{\mu}\right) \frac{d\mu}{d\phi} \nabla \phi \quad (\text{A.36})$$

where the particle flux due to viscosity does not depend on the viscosity of the suspending fluid.

Comparing global and local viscosity measurements

Huang and Bonn [2007] study the viscosity of concentrated suspensions. They show an agreement between global and local viscosity measurements by taking the particle migration (i.e. a particle density gradient) recognized by Leighton and Acrivos [1987] into account. They use MRI (Magnetic

Resonance Imaging) to measure the concentration gradient resulting from flow-induced particle migration. They find that the suspension dilates in regions of high shear (near the moving cylinder), compacts in regions of low shear (near the stationary cylinder), and that the concentration increases linearly with increases distance from the moving cylinder, which leads to viscosity variations across the sheared gap. In order to obtain accurate global viscosity measurements, Huang and Bonn [2007] use a small-gap, large-aspect-ratio Couette geometry in which particle migration is suppressed due to a balance between particle migration caused by the shear-rate gradient and migration due to the viscosity gradient. To compare the global and local measurements (local measurements are made in an wide-gap Couette geometry) they consider the effect of particle migration within the wide-gap experiments by measuring the viscosity as a function of volume fraction. They conclude that the flow of a concentrated suspension is governed by

$$\sigma = \mu(\phi)\dot{\epsilon} \tag{A.37}$$

Their measurements agree with the Krieger-Dougherty model discussed in Section A.3.3. Particle volume fraction increases linearly with distance away from the moving cylinder. This confirms the idea that viscosity varies within the sheared gap due to the migration of particles away from the moving cylinder.

At low speeds, the fluid is treated as a Bingham fluid rather than a Newtonian fluid. In their experiments, for velocities below some critical value V_c , they observe shear banding in which two well-defined bands form: a sheared band and a motionless band. They conclude that the viscosity profiles $\mu(r)$ are not independent of rotation speed (Figure A.10). For slow rotation speeds, (i.e. $V < V_c$) there exists a non-zero intercept (yield stress) in the stress-strain-rate plots at different speeds. The motionless region influences the viscosity of the sheared band—it tends to increase the viscosity. This was first noted by Huang et al. [2005] who discovered that below a certain strain-rate $\dot{\epsilon}$, stress remains constant and above $\dot{\epsilon}$, increases directly with strain-rate (Newtonian). They define the Leighton number as $Le =$

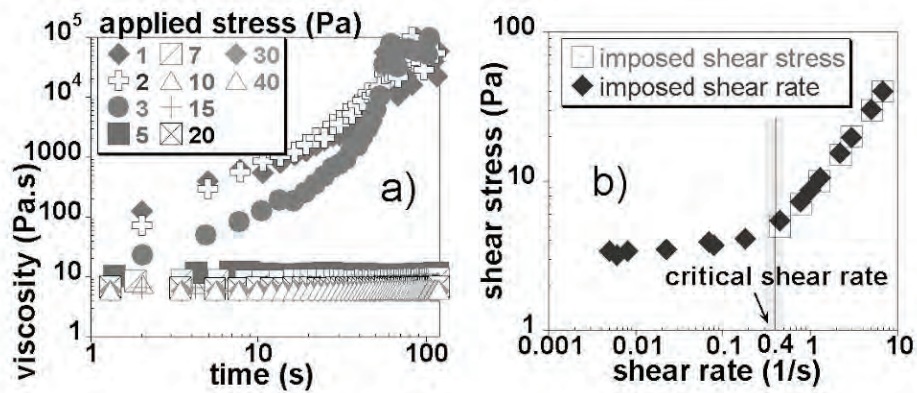


Figure A.10: Plot and caption from Huang et al. [2005]. (a) *Viscosity bifurcation: under imposed stress the viscosity either grows in time or decreases; therefore the steady-state viscosity jumps to infinity at a critical stress. This allows us to define both the critical stress and the critical shear rate. Before each experiment, the material is presheared during 30 s at 30s⁻¹ to obtain a reproducible initial state.* (b) *Flow curve (shear stress versus shear rate) for 20 mPa s silicone oil, both at an imposed macroscopic shear stress and shear rate. The shaded area is the statistical error bar.*

A.3. What controls a magma's effective viscosity

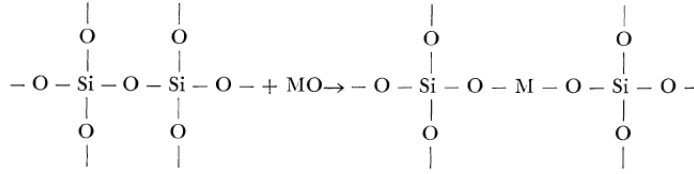


Figure A.11: Schematic diagram of Si-O bonds being replaced by M-O bonds. From Bottinga and Weill [1972].

$\mu\dot{\epsilon}/\sigma$ which is a ratio between lubrication and frictional forces and describes the transition from yielding behavior to viscous flow. Below a critical Le ($\sim 7 \times 10^{-4}$) the suspension behaves as a dry granular material.

A.3 What controls a magma's effective viscosity

A.3.1 Melt viscosity

Magma is a multiphase fluid. A rheological description of a magma includes the influence of a temperature-dependent melt viscosity, the presence of crystals and bubbles, and the deformation rate [Webb and Dingwell, 1990; Giordano et al., 2008].

Chemical composition and silicate melt structure

Silicate melt viscosity depends on bulk chemistry and can be explained in terms of a deforming silicate structure (e.g. Bottinga and Weill [1972]). The melt is made up of an extensive framework of silicate tetrahedra (SiO_4) linked to one another by Si-O bonds. In pure quartz SiO_2 , all four oxygen atoms in each tetrahedron are bridging making an extremely rigid framework; whereas, olivine is made of isolated tetrahedron which are connected by cations. Flow of a silicate melt requires movement of the strong Si-O bonds. The addition of metal oxides to silicate melt leads to a weaker structure (Figure A.11) and causes a decrease in viscosity (see Bottinga and Weill [1972]).

Rate of deformation

The response of magma to an applied differential stress depends strongly on the timescale over which the stress is applied. In particular, the relaxation time of a melt governs whether the melt deforms viscously or elastically. The relaxation rate $\dot{\epsilon}_r$ describes the structural relaxation of a silicate melt [Webb and Dingwell, 1990]. Deformation experiments on analogue and natural magmas at temperatures above the liquidus demonstrate that at low strain rates, $\dot{\epsilon} \ll \dot{\epsilon}_r$ (e.g. 10^{-5} s^{-1}) magma exhibits Newtonian behavior [Dingwell, 1995; Murase and McBirney, 1973; Spera et al., 1988; Shaw et al., 1968]; whereas, its behavior becomes non-Newtonian at high strain-rates, $\dot{\epsilon} \gg \dot{\epsilon}_r$, when the melt structure cannot respond fast enough to deformation and so behaves in an elastic (and sometimes brittle) manner [Simmons et al., 1982; Webb and Dingwell, 1990]. This phenomenon is known as the rheological glass transition. The glass transition temperature is a function of melt composition and water content (i.e. GTT strongly decreases with water content) [Deubener et al., 2003]. Caricchi et al. [2007] perform deformation experiments on particle-silicate melt suspensions which show that at low strain rates (10^{-6} to 10^{-5} s^{-1}) the suspensions behave as a Newtonian fluid. Increasing strain-rate causes shear-thinning effects which they attribute to a decrease in randomness of the particle distribution. This type of behavior follows power law relationship: $\tau = A\dot{\epsilon}^n$ (see Appendix A.1 for further discussion on constitutive equations) where τ is shear stress, $\dot{\epsilon}$ is strain rate, A is the flow consistency index and n is the flow behavior index. Values of $n < 1$ show shear-thinning behavior and $n > 1$ show shear-thickening behavior. At high enough strain rates ($\sim 10^{-4} \text{ s}^{-1}$), the particles reach a maximum degree of ordering and Binghamian behavior emerges.

Temperature and dissolved volatiles

Silicate melt viscosity depends strongly on temperature (Figure A.12). Shaw [1972] demonstrates that the temperature T dependence of silicic melts fol-

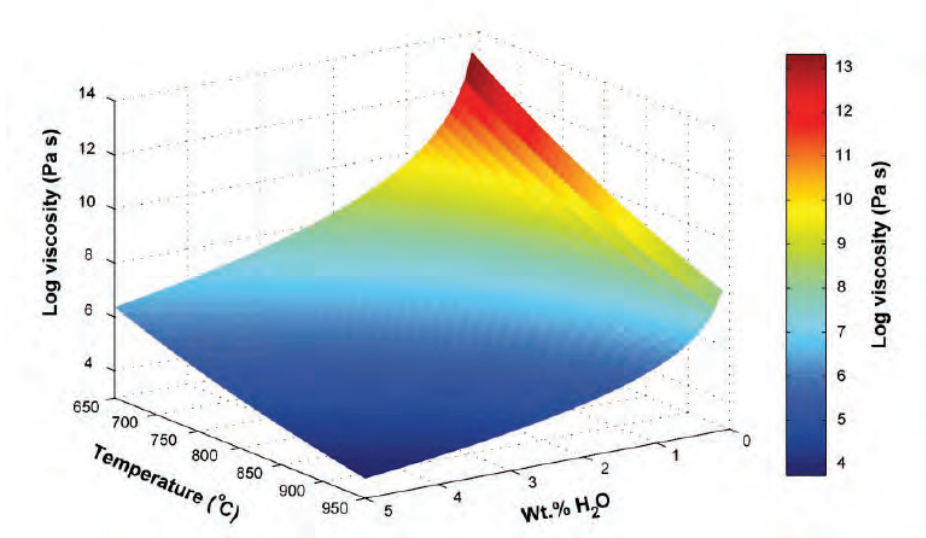


Figure A.12: From Gonnermann and Manga [2007] Silicate melt viscosity as a function of temperature and water content after empirical formulation of Hess et al. [2001].

lows an Arrhenius relationship:

$$\ln \eta = \ln A + \frac{E}{RT}, \quad (\text{A.38})$$

where the constants A and E are given by the y-intercept and the slope of the line in a plot of $\ln \eta$ vs. $1/T$. A represents the value of $\ln \eta$ at infinite temperature. E is the activation energy for viscous flow and R is the gas constant. Until recently, this was a common approximation used for most melt viscosity models.

Giordano et al. [2008] present a model to calculate melt viscosities for a wide range of compositions and show that the relationship between temperature and viscosity does not necessarily follow an Arrhenian relationship. They use the Vogel-Tammann-Fulcher (VFT) viscosity equation: $\ln \eta = A + (B/T - C)$ to account for the non-Arrhenian temperature-dependence of melt viscosity. A is assumed to be constant for all melts, which sug-

gests that at high temperatures silicate melts converge to the same viscosity value. The constants B and C are adjustable parameters which account for compositional effects. The parameters are defined as linear groups of oxide components. Dissolved volatiles (e.g. mostly H_2O and some CO_2) decrease melt viscosity [Giordano and Dingwell, 2003] (Figure A.12).

A.3.2 Bubbles

Depending on their size, bubbles can either increase or decrease a magma's viscosity [Taylor, 1932; Manga et al., 1998; Lejeune et al., 1999; Llewellyn and Manga, 2005]. This effect is described by the Capillary number

$$Ca = \frac{\eta_{melt}\dot{\epsilon}r}{\gamma}, \quad (\text{A.39})$$

where γ is the surface tension, η_{melt} is the melt viscosity, r is the bubble radius, and $\dot{\epsilon}$ is the shear strain rate. The Capillary number is a ratio of viscous shear stresses which cause bubble deformation and surface tension which resists bubble deformation. At low capillary number, bubbles do not deform and may increase the viscosity of the suspension. In the higher Ca limit, bubbles may stretch and deform creating free-slip boundaries along the melt-vapor interface, subsequently accommodating deformation resulting in a lower overall magma viscosity relative to the melt viscosity.

A.3.3 Crystals

There have been numerous models to describe the effect of crystals on magma's effective viscosity (see Petford [2009]). The earliest description of two-phase flow came from Einstein [1906] who considered a dilute (i.e. particles far enough apart to be treated independently of each other) suspension of spherical particles that could be described by an effective viscosity:

$$\eta = \eta_o(1 + 2.5\phi), \quad (\text{A.40})$$

where η_o is the viscosity of the suspending fluid and ϕ is the volume fraction of dispersed particles. As ϕ increases, fluid has to flow around the spheres,

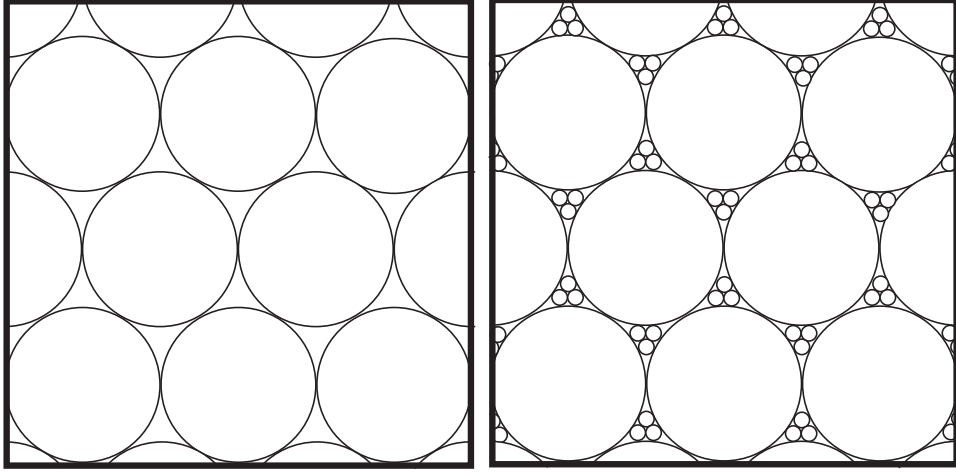


Figure A.13: Monodisperse and polydisperse rigid spheres.

which increases the effective viscosity of the suspension. Einstein's model is linear in ϕ and only applicable to dilute suspensions ($\phi < 0.05$ [Roscoe, 1952]). Krieger and Dougherty [1959] present a theoretical expression for the relative viscosity (i.e. the ratio of the effective viscosity of the suspension to the viscosity of the suspending fluid) of suspensions at non-dilute ($\phi > 0.05$) concentrations:

$$\eta = \left(1 - \frac{\phi}{\phi_m}\right)^{K\phi_m}, \quad (\text{A.41})$$

where $K = 2.5$ for monodisperse spheres and ϕ_m (maximum packing fraction) is the volume fraction of solids in closest-packing at which the relative viscosity approaches infinity,

$$\lim_{\phi \rightarrow \phi_m} \eta \rightarrow \infty. \quad (\text{A.42})$$

Said differently, when ϕ_m is reached the suspension is unable to flow. ϕ_m depends on particle shape and shape distribution and is always higher for polydisperse systems than for monodisperse systems (Fig. A.13). Lejeune and Richet [1995] report that when crystal concentrations reach $\sim 40\%$ there is a rheological transition to a suspension dominated by crystal-crystal interactions that acts like a Bingham fluid (see Figure A.14). In this regime the

A.4. Linking a magma's microstructure to a macroscopic description of its rheology

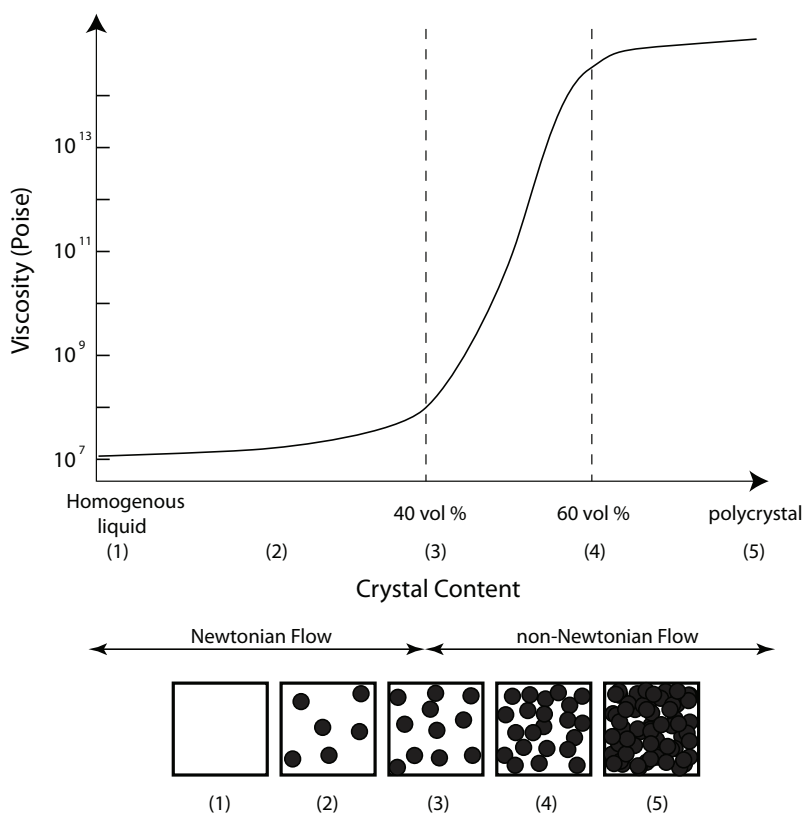


Figure A.14: From Lejeune and Richet [1995]. Rheological regimes as a function of crystal concentration.

touching framework of crystals gives rise to a yield strength which depends on the aspect ratio of the crystals [Saar et al., 2001].

A.4 Linking a magma's microstructure to a macroscopic description of its rheology

The microphysics governing the rheology of crystal-rich silicic magma remains an open question. An outstanding issue in the analysis of a granite's rheology and a key hurdle to understanding how large silicic eruptions occur rapidly is explaining how a microstructure behaves at the crystal-scale

A.4. *Linking a magma's microstructure to a macroscopic description of its rheology*

in relation to a macroscopic property such as the effective viscosity. The goal of this section is to build understanding of how an average rheology of a particle suspension is related to its microstructure. In particular, I address how certain classes of microtextures (e.g. schlieren around stoped blocks) observed in plutonic rocks can be related quantitatively to the coupled crystal-liquid dynamics that ultimately govern the rheological response of the magma. Field observations of kinematic indicators including crystal alignments and textural gradients around the margins of stoped blocks (see Fig. A.15) compared with scaling analysis drawn from thin viscous sheet theory [Wiebe et al., 2007] suggest that the host silicic magma had a viscoplastic rheology with a yield stress. The missing link in the analysis, however, is the relationship of this macroscopic rheology to the microphysics governing the deformation of the crystal-rich magma. To understand how a magma's microstructure might evolve to produce the textures we observe in the field, I perform quasi-two-dimensional analogue experiments to investigate the responses of mono- and poly-disperse mixtures of plastic particles (analogue crystals) and viscous liquid to an imposed simple shear using a rotating cylinder-Couette setup under laminar flow conditions. I aim to understand phenomena such as particle alignment and particle migration in terms of the three-way (solid-liquid, liquid-solid, solid-solid) particle-fluid coupling in the experiments. I use particle image velocimetry (PIV) and video analysis to characterize the microstructural response to imposed shear for a broad range of strain rates, particle concentrations and shape distributions. Stress-strain rate curves are measured and the corresponding rheologies are applied in numerical models to understand measured velocity profiles.

A vast amount of work has been done to characterize the rheology of particle suspensions (section A.2). Specifically, experimental work on natural and analogue suspensions demonstrates that the concentration of crystals suspended in a magma influences the magnitude of its viscosity and its rheological response to an imposed stress. An important component in the rheological description of a magma is the details of how the microstructure behaves in order to produce a macroscopic response.

A.4. *Linking a magma's microstructure to a macroscopic description of its rheology*

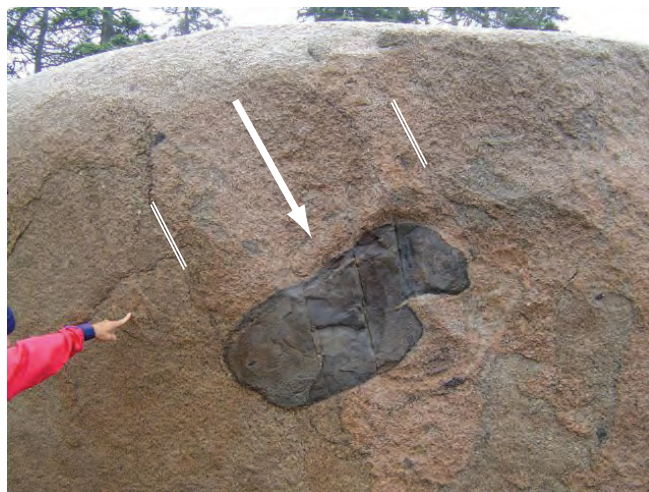
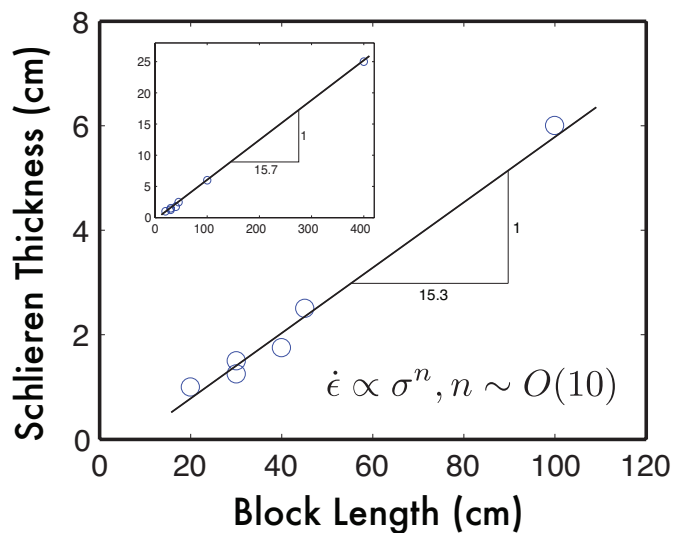


Figure A.15: (*bottom*) Photo of dense rhyolite that settled into a less dense silicic mush. Parallel white lines indicate aligned biotite crystals (i.e. schlieren) and textural gradients that indicate the accumulation of simple shear strains along the side boundaries of the falling block. The white arrow indicates the direction of paleo-vertical. (*top*) Plot of schlieren thickness vs. block length and a comparison with thin viscous sheet theory. The linear relationship constrains the rheology of the silicic mush to be stress-dependent and close to a perfect plastic.

A.4. *Linking a magma's microstructure to a macroscopic description of its rheology*

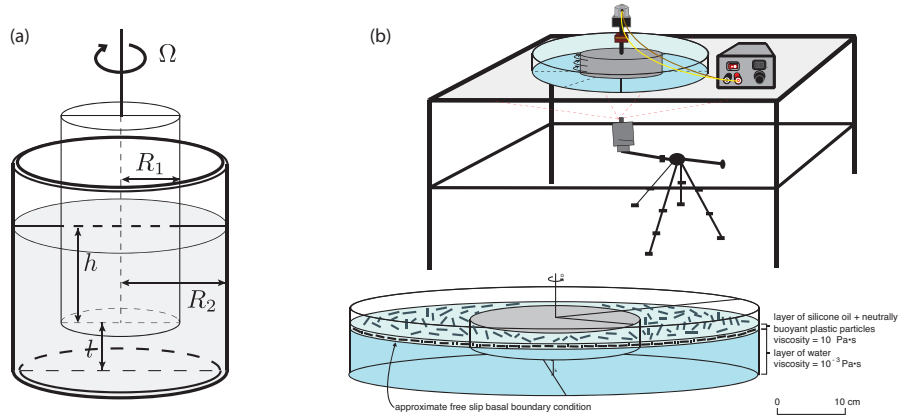


Figure A.16: (a) General design of concentric cylinder rheometer. (b) Experimental set-up. Simplified cartoon of tank, motor, torque sensor, power supply, and video recording set-up. Bottom cartoon of inner and outer cylinder dimensions with approximate fluid layer depths and particle size.

A.4.1 Experimental set-up

Rotational rheometers

Rotational rheometers have several features which make them appropriate for investigating the rheology of particle suspensions. Measurements can be made under constant shear for long periods of time allowing steady-state flow conditions to be achieved. Additionally, several measurements can be made on the same sample at various strain rates.

I use a concentric-cylinder rheometer (or Couette apparatus) (Fig. A.16a), which consists of an inner cylinder with radius R_1 and height h and an outer cylinder with radius R_2 . The inner cylinder rotates at a prescribed speed Ω set by an external motor. This mechanism produces simple shear flow in the fluid contained between the cylindrical gap. The basic concept behind all rheometers is identical: the material of interest is forced to flow in a simple, well-constrained geometry. Measurements of the force needed to drive the flow and the resulting deformation are recorded as functions of time and the measurements are then converted to stress and strain-rate. This conversion begins by recording the torque M on the inner cylinder. The torque M is

A.4. *Linking a magma’s microstructure to a macroscopic description of its rheology*

then converted to a shear stress τ by the relation:

$$\tau = aM \tag{A.43}$$

where a is a constant related to the geometry of the concentric-cylinder set-up. For a set-up similar to Fig. A.16a:

$$a = \frac{1}{2\pi h R_1^2} \tag{A.44}$$

I use a wide gap concentric-cylinder rheometer with an outer cylinder ($d = 60$ cm, $h = 8$ cm) that is transparent to allow transmission of light and easy viewing through the base the side-walls as I film all experiments from below. The inner cylinder ($d = 22$ cm, $h = 4$ cm) is suspended within the larger cylinder with a gap width = 19 cm allowing the Couette gap to be more than $10\times$ the particle length (~ 1 cm) [Powell, 1991]. I control the rotation of the inner cylinder using a brushless DC motor and a constant voltage programable DC power supply, which sets the rotation rate of the inner cylinder. There is a torque sensor mounted between the inner cylinder and the motor, which records the torque applied to the inner cylinder. The goal was to use this torque measurement to calculate stress.

Experimental materials

The working fluids for the experiments are silicone oil and water. A layer of Dow Corning 200® Fluid (silicone oil), 10,000 CST ($\rho = 967$ kg m⁻³, $\eta = 9.7$ Pa s) is stratified above water ($\rho = 997$ kg m⁻³, $\eta = 10^{-3}$ Pa s). The layer depth of the silicone oil is approximately 0.5 cm and the water layer is approximately 5 cm deep. The inviscid water layer below the viscous silicone oil creates a free-slip boundary condition along the bottom of the cylinder, reducing the geometry to two dimensions with a no-slip boundary condition at the moving boundary (i.e. the inner cylinder) and the stationary boundary (i.e. the outer cylinder). I use plastic particles as analogue crystals. Two different particle shapes—elongate prisms and equant spheres—represent, for example, two dominant minerals in silicic magmas (feldspar and quartz).

A.4. *Linking a magma’s microstructure to a macroscopic description of its rheology*

The particles are neutrally buoyant in the silicone oil.

I use a monolayer of particles suspended in a thin layer of oil to investigate the essential physics behind the microstructure in the plane of shear. This technique has been used by Belzons et al. [1981] who performed experiments in a Couette device with layer of oil with a depth of $2a$, where a is the sphere radius of the particles. The oil layer floats on top of a water layer similar to our setup. The effective viscosity measurements are uniformly lower than viscosity measurements of 3D suspensions [see Brady and Bossis, 1985]. The difference can be attributed to the fact that at high concentrations particles in the monolayer can follow the path of least resistance and emerge out of the plane of shear, which would lower the effective viscosity.

A.4.2 Methods for calibration

Calibration of the torque sensor begins with recording the torque on the cylinder in air and then in water at a range of voltages ($V = 0.1 - 5.0$). Measuring the torque on the cylinder in air detects any wobbles in the cylinder as it rotates that could affect the torque data. This signal is subtracted from all future measurements in water and oil. Any added torque from the presence of the water layer is subtracted from measurements with oil. The Newtonian case (silicone oil only) is used as the baseline for experiments with particles. The torque data is converted to a shear stress using equation A.43.

A.4.3 Experimental conditions

For the rheological measurements, the rotation rate is ramped up and down by adjusting the voltage through the power supply. For experiments in which I measure microstructure behavior, the rotation rate is fixed for a period of time before ramping up or down. There is a no-slip condition at side walls of cylinder and a free-slip condition along the base. We prescribe a particle volume concentration and shape distribution. Fig. A.17 shows a schematic parameter space for the proposed experiments. I ran a total of 32 experiments for each particle distribution (i.e. mono- or poly-disperse)—

A.4. Linking a magma's microstructure to a macroscopic description of its rheology

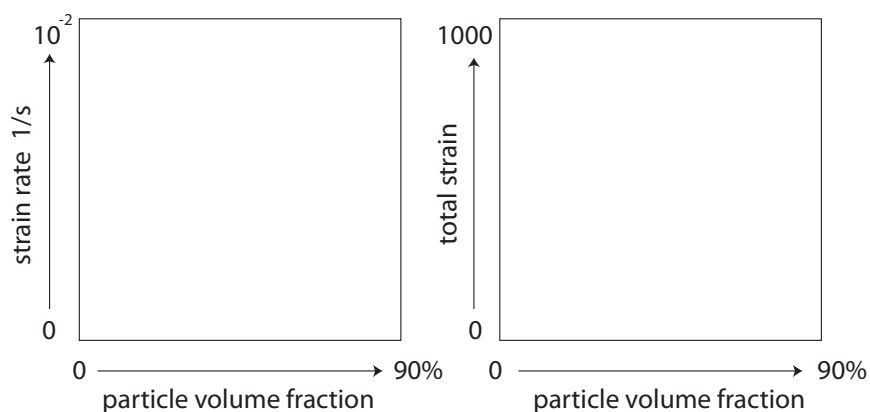


Figure A.17: Example regime diagrams for (*right*) fixed strain-rate, increasing total strain and (*left*) fixed total strain, with increasing strain-rate. The goal is to compare the radial velocity profile for each regime (see section A.4.4).

that includes four different particle concentrations at four strain-rates and four total strains $((4 \times 4) + (4 \times 4) = 32)$. I measure velocity profiles for each regime.

A.4.4 Techniques for characterizing kinematics of particle-fluid motions

The presence of crystals has a significant effect on a magma's viscosity, extent of shear thinning, and onset of yield strength [Jeffrey and Acrivos, 1976; Lejeune and Richet, 1995; Hoover et al., 2001; Saar et al., 2001; Caricchi et al., 2007]. Since magmas are multi-component suspensions with a variety of crystal shapes and sizes, incorporating the effect of crystal shape can make suspension models used to study magma movement more accurate. I have developed a few techniques to analyze the kinematics of particle-particle interaction, particle rotation and alignment. For each experiment, measurements of the microstructure behavior include: particle alignment (feldspars), particle paths and interactions, radial variation in particle concentration, average velocity profile extending out from inner cylinder.

A.4. *Linking a magma's microstructure to a macroscopic description of its rheology*

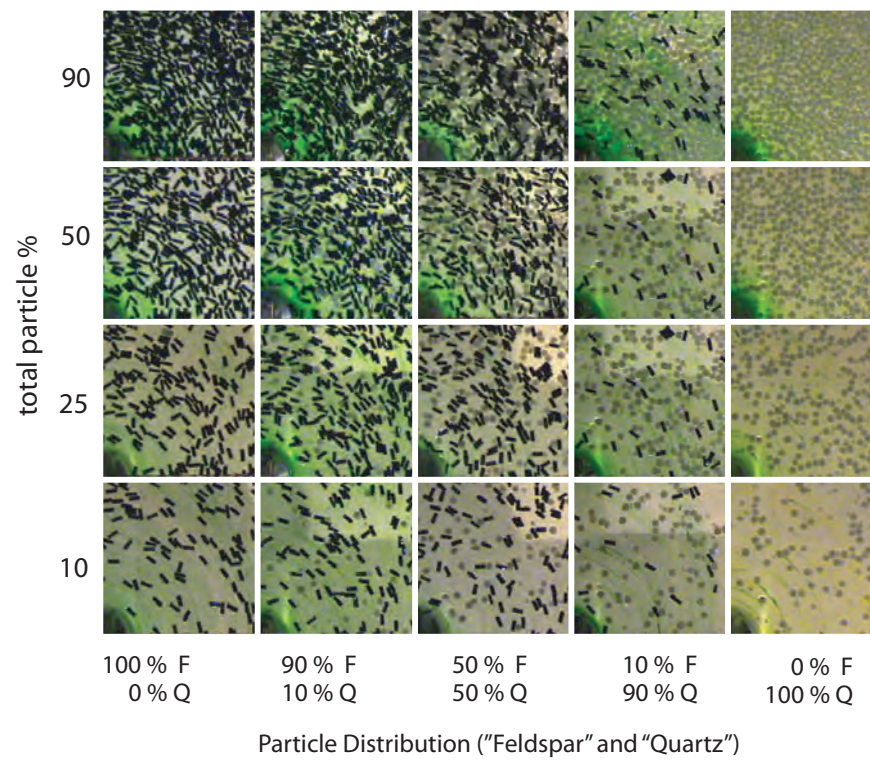


Figure A.18: Regime diagram showing the initial conditions of the experiments. Feldspars = black prisms. Quartz = white spheres.

A.4. Linking a magma's microstructure to a macroscopic description of its rheology

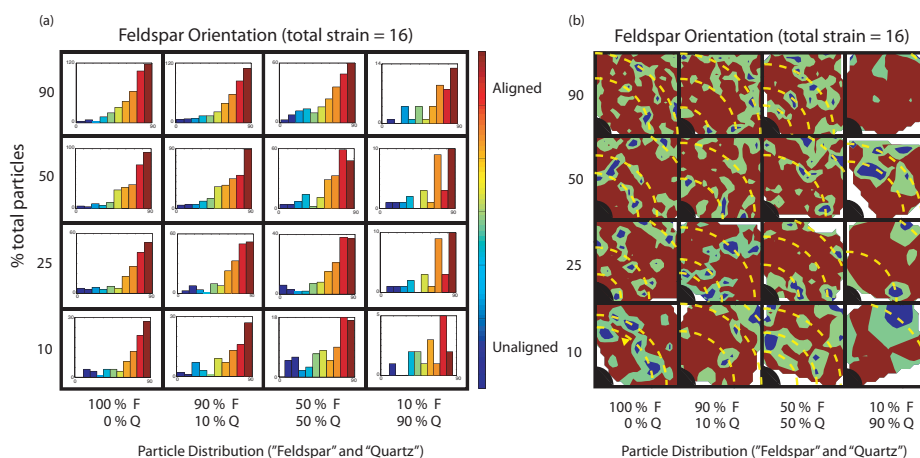


Figure A.19: (a) Histogram plots of feldspar orientation distribution. Orientations range from 0 (perfectly unaligned with flow—blue) to 90 (perfectly aligned with flow—red). Concentrations range from monodisperse feldspar particles to polydisperse mixtures of feldspar and quartz. The total particle concentration ranges from 10 to 90%. (b) Feldspar orientation as a function of position away from the inner cylinder (black quarter circle in the bottom right of each plot). Yellow dotted lines trace interpreted bands of unaligned feldspars.

Particle alignment mapping

I measure feldspar alignment by recording the angle of each particle at a given amount of total strain (number of cylinder revolutions). Fig. A.19a and A.19b show the orientation distributions for different particle mixtures and total concentrations as histograms and as a function of radius, respectively. I hand-trace the particles, from which an automated code measures the orientation of each particle. The goal was to establish a regime diagram for the evolution of particle alignment during a measurement of macroscopic rheology.

Particle tracking

I trace the particle paths using still-frames taken from video footage. By tracking one particle at a time, I qualitatively record particle interactions

A.4. *Linking a magma's microstructure to a macroscopic description of its rheology*

and rotation rate of individual particles. While this method is tedious and has yet to produce promising results, the goal was to expand the technique by following single particles through one entire orbit around the cylinder. The new set-up (Fig. A.16b utilizes the full-tank view (as apposed to 1/4 of the tank as in previous experiments not described in this thesis)). The goal is to understand how hydrodynamic particle interactions influence the particle orientation distribution.

Particle image velocimetry

I use PIV (particle image velocimetry) to calculate average velocity profiles. Measurements are made using the PIV toolbox in MATLAB®. The process begins by importing two still-frames taken from video footage of an experiment. The time (in seconds) between the frames is dt . The frames are divided into many small windows. A displacement vector is calculated for each window by means of cross-correlation technique. The displacement vector is converted to a velocity vector after dividing by dt . I radially sample the velocity matrix and then plot azimuthally-averaged velocity profiles (see Fig. A.20).

A.4.5 Measuring a macroscopic rheology: What did not work

The aim of the experiments for measuring macroscopic suspension rheology was to cover a broad range of conditions to characterize the effect of particles (shape distribution and concentration) on the apparent viscosity of a suspension. The main goal was to compare measured macroscopic rheologies to qualitative descriptions of the corresponding microstructures. Suspensions regimes are outlined in Fig. A.18.

For all experiments, the torque measurements on the cylinder could not be reproduced. The wobble between the motor and torque sensor was too large compared to the range in torque measurements. I employed various methods to reduce the wobble:

1. Recutting the gears that connect the motor to the rotating cylinder

A.4. Linking a magma's microstructure to a macroscopic description of its rheology

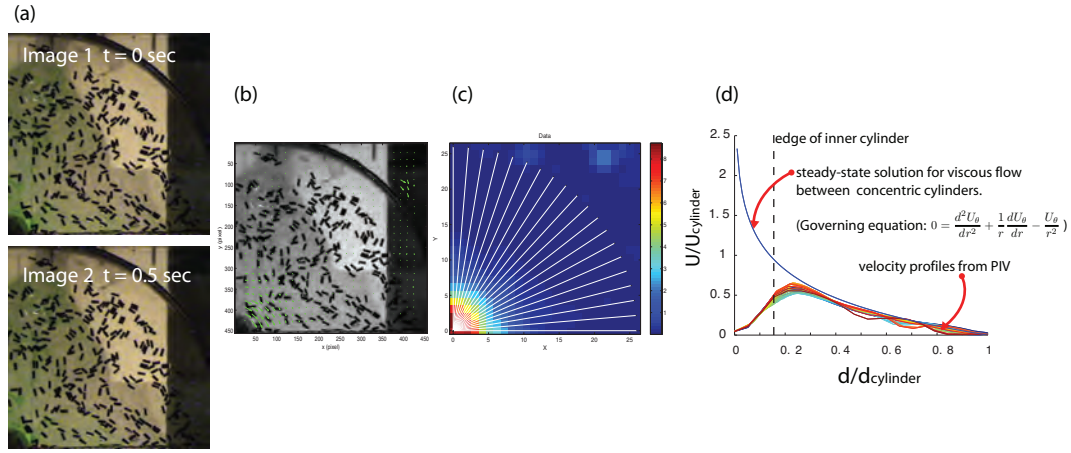


Figure A.20: Image analysis process. (a) Images used for PIV analysis, $dt = 0.5 \text{ sec}$. (b) Velocity vectors (green arrows) plotted over image 2. (c) Sampling the velocity matrix. (d) Plot of velocity profiles. Blue line is the steady-state solution for flow between concentric cylinders.

2. Removing the gears
3. Adding foam padding between any metal-to-metal contact points between the torque sensor cylinder and the motor
4. Loosening the connection (i.e. the tightness) between the supporting beam and the torque sensor

Even after various adjustments to the apparatus, I concluded that the error on the measurements was too large to confidently convert the torque measurements to a shear stress—which would then have been used to estimate the effective viscosity of the suspension at each rotation rate.

A.4.6 Future work

Solutions to the torque sensitivity

Given the delicate nature of this type of experiment, I concluded that my home-made rheometer could not produce accurate measurements for the macroscopic rheology of my particle suspensions. One possible solution that

A.4. *Linking a magma's microstructure to a macroscopic description of its rheology*

I did not explore, was to use an ambient fluid with a higher viscosity as a way to increase the torque on the inner cylinder. Alternatively, a thicker fluid layer depth (i.e. more fluid in contact with the rotating cylinder) might increase the torque value above the measured variation caused by instrument wobble. The problem in this case is that as the fluid layer increases beyond one particle thickness, the experiment is no longer two-dimensional.

New ideas for future experiments

Similar to the experiments described by Belzons et al. [1981], the difficulty in monitoring a quasi-two-dimensional particle suspension in which some of the particles have long aspect ratios is that in a monolayer with a free-slip boundary above and below, the particles will follow the path of least resistance during deformation and will move out of the plane of shear, which lowers the effective viscosity measurement. As a first order solution, using only equant shapes to match micro- and macro-viscosity measurements would eliminate the possibility for rotation out of a two-dimensional plane. One other interesting direction for future work is to use MEMS (Microelectromechanical systems) particles to measure the stress distribution among particles. The goal of this type of experiment would be to compare the stress distributed between particles as they rotate and collide to a macroscopic rheology measurement as a tool to understand how stress is accommodated at the microscopic scale—e.g. how strain associated with magma mobilization is accumulated and preserved at the crystal-scale in silicic magma chambers.